Instituto Superior de Engenharia
Politécnico de Coimbra

DEPARTMENT OF ELECTRICAL ENGINEERING

# Sensitivity analysis and design of dynamic wireless power transfer coil geometries for two-wheeled electric vehicles under misalignments

Dissertation to fulfill the Master's degree in Electrical Engineering

Specialization in Automation and Communications in Energy Systems

Author

**Mário Mendes Loureiro**

Supervisors

**Professor Rita Manuela da Fonseca Monteiro Pereira**

**Professor Adelino Jorge Coelho Pereira**

INSTITUTO POLITÉCNICO DE COIMBRA

INSTITUTO SUPERIOR DE ENGENHARIA DE COIMBRA

Coimbra, December 2025

# Abstract

This work investigates the geometric design and optimisation of a dynamic inductive power transfer coupler for two-wheeled electric vehicles, under misalignment and magnetic-field exposure constraints. A computational three-dimensional finite-element model of a shielded rectangular coupler is developed in Ansys Maxwell, an electromagnetic finite-element solver, to characterise coupling coefficients and magnetic flux density levels on control planes along the longitudinal travel range and under lateral and angular misalignments. Two simulation datasets are generated: one varying only geometric parameters at a nominal position for surrogate construction and global sensitivity analysis, and a second jointly sampling geometry, the travel range and misalignments for optimisation. Sparse Polynomial Chaos Expansions and Canonical Low-Rank Approximations surrogates are built to quantify Sobol' indices, revealing that a small subset of primary-side geometric variables dominates both coupling efficiency and magnetic field levels. Random Forest Regressors are then trained on the extended dataset and embedded in a Non-dominated Sorting Genetic Algorithm II to solve a multi-objective optimisation problem that maximises worst-case coupling, improves robustness to misalignment, and enforces magnetic-field leakage limits on all control planes. Optimal designs from the Pareto fronts were obtained, and a subset was selected for re-evaluation using the finite-element method. The results confirm that the proposed surrogate-assisted framework yields coupler geometries with enhanced dynamic coupling and reduced magnetic field leakage, while respecting the mechanical constraints for the electric motorcycle system.

**Keywords**: Dynamic inductive power transfer, Global sensitivity analysis, Magnetic field exposure, Multi-objective optimisation, Surrogate models.

Mário Loureiro

# Resumo

Este trabalho investiga o projeto geométrico e a otimização de um acoplador de transferência indutiva dinâmica de potência para veículos elétricos de duas rodas, sob restrições de desalinhamento e exposição a campos magnéticos. Um modelo computacional tridimensional de elementos finitos de um acoplador retangular com blindagem é concebido no Ansys Maxwell, um simulador eletromagnético de elementos finitos, para caracterizar os coeficientes de acoplamento e os níveis de densidade de fluxo magnético em planos de controlo ao longo do percurso longitudinal e sob desalinhamentos laterais e angulares. São gerados dois conjuntos de dados a partir da simulação: um variando apenas os parâmetros geométricos numa posição nominal para construção de modelos substitutos e análise de sensibilidade global, e um segundo amostrando conjuntamente a geometria, o percurso e os desalinhamentos para otimização. São construídos modelos substitutos *Sparse Polynomial Chaos Expansions* e *Canonical Low-Rank Approximations* para quantificar os índices de Sobol', revelando-se que um reduzido subconjunto de variáveis geométricas do lado primário domina tanto o desempenho do acoplamento quanto os níveis de campo magnético. Em seguida, são treinados os regressores *Random Forest* no conjunto de dados estendido e incorporados num *Non-dominated Sorting Genetic Algorithm II* para resolver um problema de otimização multi-objetivo que maximiza o acoplamento no pior caso, melhora a robustez ao desalinhamento e impõe limites de fuga de campo magnético em todos os planos de controlo. Foram obtidas geometrias otimizadas a partir das frentes de Pareto, e um subconjunto foi selecionado para reavaliação com recurso ao método dos elementos finitos. Os resultados confirmam que a abordagem proposta, assistida por modelo substituto, produz geometrias do acoplador com melhor acoplamento dinâmico e menor fuga de campo magnético, respeitando as restrições de integração mecânica no sistema do motociclo elétrico.

**Palavras-chave**: Análise de sensibilidade global, Exposição a campos magnéticos, Modelos substitutos, Otimização multi-objetivo, Transferência dinâmica indutiva de potência.

# Epigraph

*After the fear, the world comes.*
**Clarice Lispector**

# Dedication

*To my parents, who under the burning sun,*
*brought me this far into the shade.*

## Acknowledgments

Upon completion of my master degree dissertation, I am really grateful to those who have offered me invaluable support during the course. I would first like to express my deepest gratitude to my parents, siblings, and grandparents for always being by my side, supporting me in achieving my goals and dreams.

I would like to express my gratitude especially,

To my girlfriend, Beatriz, for her love and unconditional support.

To my supervisors, Professor Rita Pereira and Professor Adelino Pereira, for accompanying me throughout my dissertation and for all the advice they gave me on my journey through academia and life.

To my colleagues in the master's programme, Engineers Adriana Figueiredo and Tomás Adão, for all their support, perseverance, for all the moments of joy, and for always being there when everything got more challenging.

To Engineer Queiró, for his invaluable support and constant availability.

To Engineer Ana Pinheiro for kindly granting me access to the computational resources of ISEC and for her availability, assistance, and kindness.

To Professor Francisco Pereira and Professor Simão Paredes, for their help in using the computational resources of DEIS, which contributed to the successful completion of this work.

My sincere gratitude to you all!

# Contents

# Index of tables

# Index of figures

# List of abbreviations

| | |
|---|---|
| AGV | Automated Guided Vehicle |
| ALS | Alternating Least Squares |
| ANN | Artificial Neural Network |
| BP | Bipolar Pad |
| CIED | Cardiac Implantable Electronic Device |
| CPT | Capacitive Power Transfer |
| CSV | Comma-Separated Values |
| DC | Direct Current |
| DD | Double-D Pad |
| DDQ | Double-D Quadrature Pad |
| DIPT | Dynamic Inductive Power Transfer |
| DoE | Design Of Experiments |
| DWPT | Dynamic Wireless Power Transfer |
| EM | Electromagnetic |
| EMC | Electromagnetic Compatibility |
| EMF | Electromagnetic Field |
| EV | Electric Vehicle |
| FEA | Finite Element Analysis |
| FEM | Finite Element Method |
| GPR | Gaussian Process Regression |
| GSA | Global Sensitivity Analysis |
| HF | High Frequency |
| ICNIRP | International Commission On Non-Ionizing Radiation Protection |
| IEC | International Electrotechnical Commission |
| IEEE | Institute Of Electrical And Electronics Engineers |
| IMD | Implanted Medical Device |
| IPT | Inductive Power Transfer |
| ISO | International Organization For Standardization |
| J–A | Jiles–Atherton |
| LARS | Least-Angle Regression Algorithm |
| LCA | Life Cycle Assessment |

| | |
|---|---|
| LCC | Inductor–Capacitor–Capacitor |
| LCL | Inductor–Capacitor–Inductor |
| LOO | Leave-One-Out |
| LRA | Canonical Low-Rank Approximation |
| MAE | Mean Absolute Error |
| MC | Monte Carlo |
| MF | Magnetic Flux |
| MPT | Microwave Power Transfer |
| NSGA–II | Non-Dominated Sorting Genetic Algorithm II |
| OLEV | Online Electric Vehicle |
| OMP | Orthogonal Matching Pursuit |
| OPT | Optical Power Transfer |
| OSF | Optimal Space Filling |
| PCE | Polynomial Chaos Expansion |
| PCHIP | Piecewise Cubic Hermite Interpolating Polynomial |
| PDF | Probability Density Function |
| PEN | Polyethylene Naphthalate |
| PP | Parallel–Parallel |
| PS | Parallel–Series |
| PV | Photovoltaic |
| R2 | Coefficient Of Determination |
| RBF | Radial Basis Function |
| ReBCO | Rare-Earth Barium Copper Oxide |
| RF | Random Forest Regression |
| RMS | Root Mean Square |
| RMSE | Root Mean Square Error |
| RPT | Resonant Power Transfer |
| SAE | Society Of Automotive Engineers |
| SAR | Specific Absorption Rate |
| SP | Series–Parallel |
| SS | Series–Series |
| SVM | Support Vector Machine |
| SVR | Support Vector Regression |
| TFL | Twisted Length Factor |
| UQ | Uncertainty Quantification |
| UQ[py]Lab | Uncertainty Quantification (Python) Laboratory |
| UQLab | Uncertainty Quantification Laboratory |
| WEVC | Wireless Electric Vehicle Charging |
| WPT | Wireless Power Transfer |

# List of symbols

## Latin alphabet

| | |
|---|---|
| $a$ | Langevin shape parameter in $M_{an}$ |
| $a_i$ | Component of vector $a$ in $q$–norm |
| $\|a\|_q$ | Hyperbolic truncation norm |
| $\|\alpha\|$ | Total degree of multi index |
| $A$ | PCE regression matrix |
| $A_{11,2}(\mathbf{g})$ | Amplitude of $k_{11,2}$ over $\mathcal{D}$, $k_{11,2}^{\max} - k_{11,2}^{\min}$ |
| $A_{12,2}(\mathbf{g})$ | Amplitude of $k_{12,2}$ over $\mathcal{D}$, $k_{12,2}^{\max} - k_{12,2}^{\min}$ |
| $A_{ij}$ | Entry of regression matrix |
| $A_{left}$ | Area of the left control plane |
| $A_{right}$ | Area of the right control plane |
| $A_{top}$ | Area of the top control plane |
| $\mathcal{A}$ | PCE multi index truncation set |
| $\mathcal{A} \setminus \{\mathbf{0}\}$ | All PCE indices excluding constant term |
| $\mathcal{A}_{M,p,q}$ | Hyperbolic truncation index set |
| $\mathcal{A}_i$ | PCE index subset for variable group $i$ |
| $\mathcal{A}_{\{i\}}$ | PCE index subset with only variable $i$ |
| $\mathcal{A}_i^{\text{tot}}$ | PCE index subset for total effect of $i$ |
| $B$ | Magnetic flux density |
| $B_{ki}$ | Magnetic flux density sample $i$ at temperature $T_k$ |
| $B_{\text{lim}}$ | Maximum magnetic flux density limit |
| $B_p(\mathbf{g}, \mathbf{m})$ | Magnetic flux density on control plane $p$ for $(\mathbf{g}, \mathbf{m})$ |
| $\max \|B\|_p$ | Maximum magnetic flux density magnitude on plane p with $p \in \{top, left, right\}$ |
| $c$ | Reversibility coefficient in the Jiles–Atherton formulation |
| $c$ | Specific heat capacity |
| $c_0$ | PCE coefficient of constant basis term |
| $\hat{\mathbf{c}}$ | Estimated PCE coefficient vector |
| $\mathbf{c}$ | Vector of PCE coefficients |
| $C$ | Capacitance |
| $C$ | Regularisation parameter in SVR |
| $C(\mathbf{g})$ | Material index |
| $C_{\max}$ | Maximum admissible material index |
| $C_1$ | Transmitter compensation capacitance |

| | |
|---|---|
| $C_2$ | Receiver compensation capacitance |
| $\mathrm{Cov}(Z(\mathbf{x}), Z(\mathbf{x}'))$ | Covariance between process values |
| $dT$ | Incremental temperature |
| $dV$ | Incremental volume |
| $dW$ | Incremental energy converted to heat |
| $d_{sw}$ | Diameter of a single wire |
| $dm$ | Incremental mass |
| $dt$ | Incremental time |
| $D$ | Electric displacement field |
| $D$ | Total variance of response |
| $D_{i_1,\ldots,i_s}$ | Partial variance contribution |
| $\mathcal{D}$ | Dataset |
| $E$ | Electric field strength |
| $\|E\|$ | Electric field magnitude |
| $f$ | Frequency |
| $f(\mathbf{x})$ | Model function in Sobol decomposition |
| $f_0$ | Mean model response term |
| $f_1(\mathbf{x})$ | First trend basis function |
| $f_P(\mathbf{x})$ | Last trend basis function |
| $f_{\mathbf{X}}(\mathbf{x})$ | Joint probability density function of $\mathbf{X}$ |
| $f_{X_i}(x_i)$ | Marginal probability density function of $X_i$ |
| $f_i(x_i)$ | Main effect function of $X_i$ |
| $f_{ij}(x_i, x_j)$ | Second order interaction function of $X_i$ and $X_j$ |
| $f_j(\mathbf{x})$ | Trend basis function indexed by $j$ |
| $\mathbf{f}(\mathbf{x})$ | Trend basis function vector |
| $F_{ij}$ | Entry of trend design matrix |
| $\mathbf{F}$ | Trend design matrix |
| $\mathbf{g}$ | Geometric design vector |
| $\mathcal{G}$ | Admissible design set |
| $H$ | Hat matrix |
| $H$ | Magnetic field strength |
| $H_{eff}$ | Effective magnetic field |
| $H_{ki}$ | Magnetic field strength sample $i$ at temperature $T_k$ |
| $I_1$ | Primary current |
| $I_2$ | Secondary current |
| $k$ | Kernel function |
| $k$ | Hysteresis-loss related coefficient in the Jiles–Atherton formulation |
| $k(\mathbf{x}, \mathbf{x}', \boldsymbol{\theta})$ | Covariance kernel |
| $k_{11,2}$ | Coupling coefficient between primary coil 1 and secondary coil |
| $k_{11,2}^{\max}(\mathbf{g})$ | Maximum of $k_{11,2}(\mathbf{g}, \mathbf{m})$ over $\mathbf{m} \in \mathcal{D}$ |

| | |
|---|---|
| $k_{11,2}^{\min}(\mathbf{g})$ | Minimum of $k_{11,2}(\mathbf{g},\mathbf{m})$ over $\mathbf{m} \in \mathcal{D}$ |
| $k_{12,2}$ | Coupling coefficient between primary coil 2 and secondary coil |
| $k_{12,2}^{\max}(\mathbf{g})$ | Maximum of $k_{12,2}(\mathbf{g},\mathbf{m})$ over $\mathbf{m} \in \mathcal{D}$ |
| $k_{12,2}^{\min}(\mathbf{g})$ | Minimum of $k_{12,2}(\mathbf{g},\mathbf{m})$ over $\mathbf{m} \in \mathcal{D}$ |
| $k_{PF}$ | Packing factor |
| $K$ | Kernel function in SVR |
| $\mathcal{K}_v$ | Modified Bessel function of second kind |
| $l_{e,k}$ | Primary coil exterior length ($k \in \{1,2\}$) |
| $l_{f,k}$ | Ferrite longitudinal dimension ($k \in \{1,2\}$) |
| $l_{i,k}$ | Primary coil interior length ($k \in \{1,2\}$) |
| $l_{s,k}$ | Shield longitudinal dimension ($k \in \{1,2\}$) |
| $L$ | Inductance |
| $L_1$ | Primary self inductance |
| $L_2$ | Secondary self inductance |
| $m$ | Mass |
| $m(\mathbf{x})$ | GPR trend function |
| $\mathbf{m} = (x, y, \alpha)$ | Operating-condition vector (position and misalignment) |
| $M$ | Magnetisation in the Jiles–Atherton model |
| $M$ | Number of input variables |
| $M(\mathbf{x})$ | Deterministic model response at $\mathbf{x}$ |
| $MAE$ | Mean Absolute Error |
| $M_{12}$ | Mutual inductance between primary and secondary coils |
| $M_{an}$ | Anhysteretic magnetisation |
| $M_{irr}$ | Irreversible magnetisation component |
| $M_{rev}$ | Reversible magnetisation component |
| $M_s$ | Saturation magnetisation |
| $\mathcal{M}$ | High fidelity deterministic model |
| $\mathcal{M}^*$ | Generic surrogate model |
| $\mathcal{M}_{GPR}$ | Gaussian process regression surrogate |
| $\mathcal{M}_{M,p}$ | Total degree index set |
| $\mathcal{M}_{PCE}$ | Polynomial chaos expansion surrogate |
| $\mathcal{M}_{\mathrm{PCE}\setminus i}$ | PCE surrogate built without sample $i$ |
| $\mathcal{M}_{SVR}$ | Support vector regression surrogate |
| $n_g$ | Number of geometric design variables |
| $n_{sw}$ | Number of single wires in the litz wire |
| $n_{val}$ | Number of validation samples |
| $\mathbb{N}$ | Natural numbers |

| | |
|---|---|
| $N$ | Number of training samples |
| $N_1$ | Number of primary windings |
| $N_2$ | Number of secondary windings |
| $OD_{LW}$ | Litz-wire outer diameter |
| $p$ | Length of lay (pitch) |
| $p$ | Maximal total polynomial degree |
| $p_i$ | Maximum polynomial degree in dimension $i$ |
| $P$ | Number of trend basis functions |
| $P_{in}$ | Input power |
| $P_{in,i}$ | Input power at stage $i$ |
| $P_{out}$ | Output power |
| $P_{out,i}$ | Output power at stage $i$ |
| $q$ | Hyperbolic truncation parameter |
| $Q$ | Quality factor |
| $Q_1$ | Primary coil quality factor |
| $Q_2$ | Secondary coil quality factor |
| $r$ | Maximum interaction order |
| $r(T)$ | Residual function used in parameter identification |
| $r_i(\mathbf{x})$ | Correlation with $i$th training point |
| $\mathbf{r}(\mathbf{x})$ | Correlation vector with training points |
| $\mathbb{R}$ | Real numbers |
| $R$ | Canonical rank in LRA |
| $R(\mathbf{x}, \mathbf{x}', \boldsymbol{\theta})$ | Correlation function |
| $RMSE$ | Root Mean Square Error |
| $R^2$ | Coefficient of determination |
| $\mathbb{R}^M$ | $M$ dimensional real space |
| $R_1$ | Primary resistance |
| $R_2$ | Secondary resistance |
| $R_L$ | Load resistance |
| $R_{ij}$ | Entry of correlation matrix |
| $\mathbf{R}$ | Correlation matrix |
| $s_{cf,k}$ | Primary spacing between coil and ferrite ($k \in \{1,2\}$) |
| $s_{sf,k}$ | Primary spacing between shield and ferrite ($k \in \{1,2\}$) |
| $SAR$ | Specific absorption rate |
| $S_{T_i}$ | Total Sobol index of $X_i$ |
| $S_{T_i}^{\mathrm{PCE}}$ | Total Sobol index from PCE |
| $S_i$ | First order Sobol index of $X_i$ |
| $S_{\sim i}$ | Sobol index of all variables except $X_i$ |
| $S_i^{\mathrm{PCE}}$ | First order Sobol index from PCE |

| | |
|---|---|
| $S_i^T$ | Total Sobol index notation |
| $t$ | Time |
| $t_{OC}$ | Outer coating thickness |
| $t_{f,k}$ | Primary ferrite thickness ($k \in \{1,2\}$) |
| $t_{s,k}$ | Primary shield thickness ($k \in \{1,2\}$) |
| $T$ | Temperature |
| $T(P,N)$ | Leave–one–out multiplicative correction factor |
| $TLF$ | Twisted length factor |
| $T_k$ | Temperature associated with the $k$-th $B$–$H$ dataset |
| $\mathbf{u}(\mathbf{x})$ | Auxiliary vector in GPR variance |
| $U$ | Total energy |
| $\Delta U$ | Change in total energy between consecutive adaptive passes |
| $U^{(p)}$ | Total energy at adaptive pass $p$ |
| $U_{error}$ | Error energy used in the Energy Error (%) definition |
| $U_{total}$ | Total energy used in the Energy Error (%) definition |
| $v$ | Index subset defining active variables |
| $v^{(i)}(X_i)$ | Univariate factor function in dimension $i$ |
| $v_r^{(i)}(X_i)$ | Univariate factor for rank $r$ and dimension $i$ |
| $V$ | Voltage |
| $V$ | Volume |
| $V_1$ | Source side voltage |
| $V_2$ | Load side voltage |
| $w(\mathbf{X})$ | Rank one function in LRA |
| $w^{(i)}$ | Quadrature weight indexed by $i$ |
| $w_{e,k}$ | Primary coil exterior width ($k \in \{1,2\}$) |
| $w_{f,k}$ | Primary ferrite exterior width ($k \in \{1,2\}$) |
| $w_{i,k}$ | Primary coil interior width ($k \in \{1,2\}$) |
| $w_{s,k}$ | Primary shield exterior width ($k \in \{1,2\}$) |
| $\mathbf{w}$ | Weight vector in feature space |
| $W$ | Energy converted to heat |
| $W$ | Power |
| $x$ | Longitudinal movement |
| $x_i$ | Realisation of $X_i$ |
| $x_j^{\max}$ | Upper bound of input variable $X_j$ |
| $x_j^{\min}$ | Lower bound of input variable $X_j$ |

| | |
|---|---|
| $\mathbf{x}$ | Realisation of $\mathbf{X}$ |
| $\mathbf{x}^{(i)}$ | Training input sample indexed by $i$ |
| $\mathbf{x}_{val}^{(i)}$ | Validation input sample indexed by $i$ |
| $X_1$ | First input variable |
| $X_2$ | Secondary reactance |
| $X_L$ | Inductive reactance |
| $X_L$ | Load reactance |
| $X_M$ | Last input variable |
| $X_i$ | Input variable indexed by $i$ |
| $\mathbf{X}$ | Random input vector |
| $y$ | Lateral misalignment |
| $y^{(i)}$ | Model evaluation at $\mathbf{x}^{(i)}$ |
| $y_{val}^{(i)}$ | Validation response sample indexed by $i$ |
| $\mathbf{y}$ | Vector of model evaluations |
| $Y$ | Model response random variable |
| $Y^{(i)}$ | Random response at training point $i$ |
| $Y^*$ | Surrogate response random variable |
| $\mathbf{Y}$ | Vector of random responses at training points |
| $z_{left}$ | $z$-coordinate used for the left control plane evaluation |
| $z_{right}$ | $z$-coordinate used for the right control plane evaluation |
| $z_{top}$ | $z$-coordinate of the top control plane |
| $Z(\mathbf{x})$ | Zero mean Gaussian process term |
| $Z_L$ | Load impedance |

## Greek alphabet

| | |
|---|---|
| $\alpha$ | Angular misalignment |
| $\alpha$ | Mean-field coupling parameter in Jiles–Atherton formulation |
| $\alpha_i$ | SVR dual coefficient for sample $i$ |
| $\alpha_i^*$ | SVR dual coefficient companion for sample $i$ |
| $\boldsymbol{\alpha}$ | PCE multi index |
| $\widehat{\beta}$ | Generalised least squares trend estimator |
| $\beta$ | Trend regression coefficient vector |
| $\beta_0$ | Constant trend coefficient |
| $\beta_i$ | Trend coefficient indexed by $i$ |
| $\boldsymbol{\beta}$ | PCE multi index |
| $\boldsymbol{\beta}$ | Trend coefficient vector in matrix form |
| $\gamma_{k,r}^{(i)}$ | LRA univariate polynomial coefficient |
| $\Gamma(v)$ | Euler gamma function |
| $\delta_{jk}$ | Kronecker delta |
| $\delta_M$ | Logical function used to suppress non-physical solutions |
| $\delta$ | Branch direction factor in the Jiles–Atherton formulation |
| $\delta$ | Skin depth |
| $\delta_{jk}$ | Kronecker delta |
| $\epsilon_{\mathcal{A}}$ | PCE truncation error |
| $\epsilon_{emp}$ | Normalised empirical error |
| $\epsilon_{gen}$ | Relative generalisation error |
| $\epsilon_{LOO}^*$ | Corrected leave–one–out error |
| $\epsilon_{LOO}$ | Leave one–out–error |
| $\epsilon_{val}$ | Relative validation error |
| $\varepsilon_r$ | Relative permittivity |
| $\eta$ | Power transfer efficiency |
| $\eta_{amplifier}$ | Power amplifier efficiency |
| $\eta_{coupling}$ | Coupling efficiency |
| $\eta_{ee}$ | End–to–end efficiency |
| $\eta_i$ | Stage efficiency |
| $\eta_{inverter}$ | Inverter efficiency |
| $\eta_{max}$ | Maximum efficiency in S–S compensation topology |
| $\eta_{rectifier}$ | Rectifier efficiency |
| $\eta_{regulator}$ | Regulator efficiency |
| $\theta$ | Kernel scale hyperparameter |

| | |
|---|---|
| $\boldsymbol{\theta}$ | Kernel hyperparameter vector in GPR |
| $\kappa_{12}$ | Coupling coefficient between coils 1 and 2 |
| $\lambda$ | Sparsity regularisation weight |
| $\mu_0$ | Permeability of free space |
| $\mu_r$ | Relative permeability |
| $\mu_{val}$ | Validation sample mean |
| $\mu_Y$ | Sample mean of training responses |
| $\hat{\mu}_{val}$ | Estimated validation mean |
| $\hat{\mu}_Y$ | Estimated mean response over training set |
| $\hat{\mu}_{val}$ | Estimated validation mean |
| $\xi_j$ | $j$-th scalar component of the design vector $\mathbf{g}$ |
| $\xi_j^{\max}$ | Upper bound of design variable $\xi_j$ |
| $\xi_j^{\min}$ | Lower bound of design variable $\xi_j$ |
| $\xi_j$ | Scalar component of the geometric design vector |
| $\rho$ | Density |
| $\sigma$ | Electrical conductivity |
| $\sigma^2$ | Process variance factor in predictor |
| $\sigma^2_{GPR}(\mathbf{x})$ | Predicted variance at $\mathbf{x}$ |
| $\sigma^2_Z$ | Gaussian process variance |
| $\varphi_k^{(i)}(X_i)$ | Univariate orthonormal polynomial in LRA |
| $\psi_k^{(j)}(x)$ | Univariate orthonormal polynomial basis |
| $\Psi_{\boldsymbol{\alpha}}(\mathbf{X})$ | Multivariate PCE basis polynomial |
| $\Psi_{\boldsymbol{\beta}}(\mathbf{X})$ | Multivariate PCE basis polynomial for index $\boldsymbol{\beta}$ |
| $\omega$ | Angular frequency |

# 1 Introduction and background

## 1.1 The role of wireless power transfer in the electrification of urban mobility

Electric vehicles (EVs) for micromobility, such as electric scooters, bicycles, and mopeds, are becoming increasingly widespread in urban environments as cities seek to decarbonise short-distance trips and reduce local air pollution. However, the large-scale adoption of these vehicles hinges not only on vehicle design but also on the availability of convenient, reliable, and space efficient charging solutions that can be integrated into dense urban fabrics without compromising pedestrian space or streetscape quality.

In this context, wireless power transfer (WPT) has emerged as a particularly attractive alternative to conventional plug-in charging. By transferring energy across an air gap by means of inductive or resonant inductive coupling, WPT eliminates exposed conductive connectors, reduces mechanical wear, and enables chargers to be embedded in parking bays, pavements, or the roadway itself. These features are especially appealing for micromobility applications, where vehicles are frequently parked in public space and user convenience is a critical factor for adoption.

WPT systems for EVs can be deployed in several modes, ranging from stationary charging pads for parked vehicles to dynamic configurations in which power is transferred while the vehicle is moving. The latter, commonly termed dynamic wireless power transfer (DWPT), seeks to mitigate range anxiety, reduce the size and cost of onboard batteries, and distribute energy supply along the route rather than concentrating it at a limited number of plug-in charging stations. In low-speed urban corridors or dedicated lanes, DWPT can in principle provide quasi-continuous energy replenishment to light electric vehicles, public transport fleets, and micromobility systems, thereby supporting a higher penetration of electric modes in city centres.

The direction of further research in this area is expected to support the development of sustainable cities and the seamless integration of local zero-emission transportation infrastructure [1, 2]. At the same time, the proliferation of WPT and DWPT solutions has brought issues of interoperability, electromagnetic compatibility (EMC), electromagnetic field (EMF) exposure, safety, and efficiency to the foreground. These concerns have motivated an intensification of national and international standardisation efforts. A notable example is the SAE J2954 standard for light-duty vehicles, which defines power classes, alignment procedures and acceptable criteria for interoperability, EMF emissions and EMC, with the aim of enabling the safe and widespread deployment of interoperable wireless charging systems [3]. In parallel, the SAE J2954/3 guideline, which specifically targets DWPT for light-duty vehicles, is being developed as an extension to SAE J2954, providing application-orientated specifications for DIPT systems, but is still a work in progress at the time of this study [4].

Despite substantial progress at the system and standardisation levels, the widespread deployment of DWPT, and more specifically, dynamic inductive power transfer (DIPT) systems, still requires further research to overcome several technical challenges. Key among these are the design of coil geometries that maintain high power-transfer efficiency under lateral, longitudinal, and angular misalignments, the control of EMF leakage in nearby air regions subject to stringent exposure limits, and the achievement of robust performance along realistic vehicle trajectories and operating conditions. These challenges are particularly acute for two-wheeled micromobility vehicles, whose slender geometry and motion patterns naturally lead to larger relative misalignments and more constrained packaging space than conventional passenger cars.

In this dissertation, these challenges are addressed at the coupler design level. The focus is placed on the development of a constrained design and analysis framework for DIPT coil systems dedicated to micromobility, combining finite element analysis, surrogate-based global sensitivity analysis, and multi-objective optimisation. The goal is to explore how coil geometries can be shaped to enhance power-transfer performance while respecting EMF exposure constraints on defined control planes along representative misalignment trajectories. In this context, the next section sets out the specific objectives and scope of the work.

## 1.2 Objectives

Inductive power transfer (IPT) systems are currently heading into a more advanced stage of development, with many studies being conducted on simulation and design using finite element analysis (FEA). However, the DIPT variant, which allows EVs to be powered, is still under development, and studies are needed on its efficiency, misalignment tolerance, and EMF leakage control.

The aim of the dissertation is to design and validate a constrained optimisation pipeline for DIPT coil systems for two-wheeled EVs that maximises power transfer efficiency while ensuring EMF compliance on defined controlled planes across longitudinal motion under lateral or angular misalignment.

This contribution will focus on the following objectives:

- Establish a critical state-of-the-art on DIPT systems, covering operating principles, coil geometries and conductors, power conversion topologies, compensation networks, shielding strategies, and applicable safety regulations and limits for EMF exposure and exposure;

- Develop a physics-based electromagnetic model of a representative DIPT system on a FEA solver to characterise performance along a longitudinal motion of the secondary coil over the primary coils, including lateral and angular misalignments;
- Construct a structured simulation dataset that relates relevant geometric variables, movement parameters, and misalignment scenarios of functional outputs, as well as spatial magnetic-field distributions on defined control planes;
- Formulate scalable or response-surface models, enabling rapid exploration of the design space and identification of geometry configurations that maximise transfer efficiency;
- Develop scalable surrogate or response-surface models to enable rapid exploration of the design space and to provide computationally efficient objective and constraint evaluations within an NSGA–II-based multi-objective optimisation framework;
- Formulate and solve an MF-constrained multi-objective coil-geometry optimisation problem using NSGA–II, ensuring compliance with electromagnetic exposure limits on the control planes along the entire vehicle trajectory;
- Assess robustness of candidate designs to expected variations, evaluating efficiency and field compliance under perturbed conditions;
- Standardise the handling and reporting of results to ensure that all analyses are repeatable and open to audit, including consistent data exports, clearly defined computed metrics, automatic checks against magnetic-flux-density limits on the control planes, and reproducible figure generation;
- Provide practical recommendations for DIPT coil geometry and operating conditions that balance efficiency, compliance with EMF limits, and dimensional constraints, thereby providing actionable guidance for subsequent work;
- Develop a Python framework to support and streamline the project workflow, using data generated by a finite-element electromagnetic solver.

## 1.3 Structure of the dissertation

The dissertation is organised into seven chapters, which follow the logical progression from contextual background and theoretical foundations, through numerical modelling and surrogate-based sensitivity analysis, to multi-objective optimisation and design recommendations. Figure 1.1 represents a graphical perspective on the structure of the work.

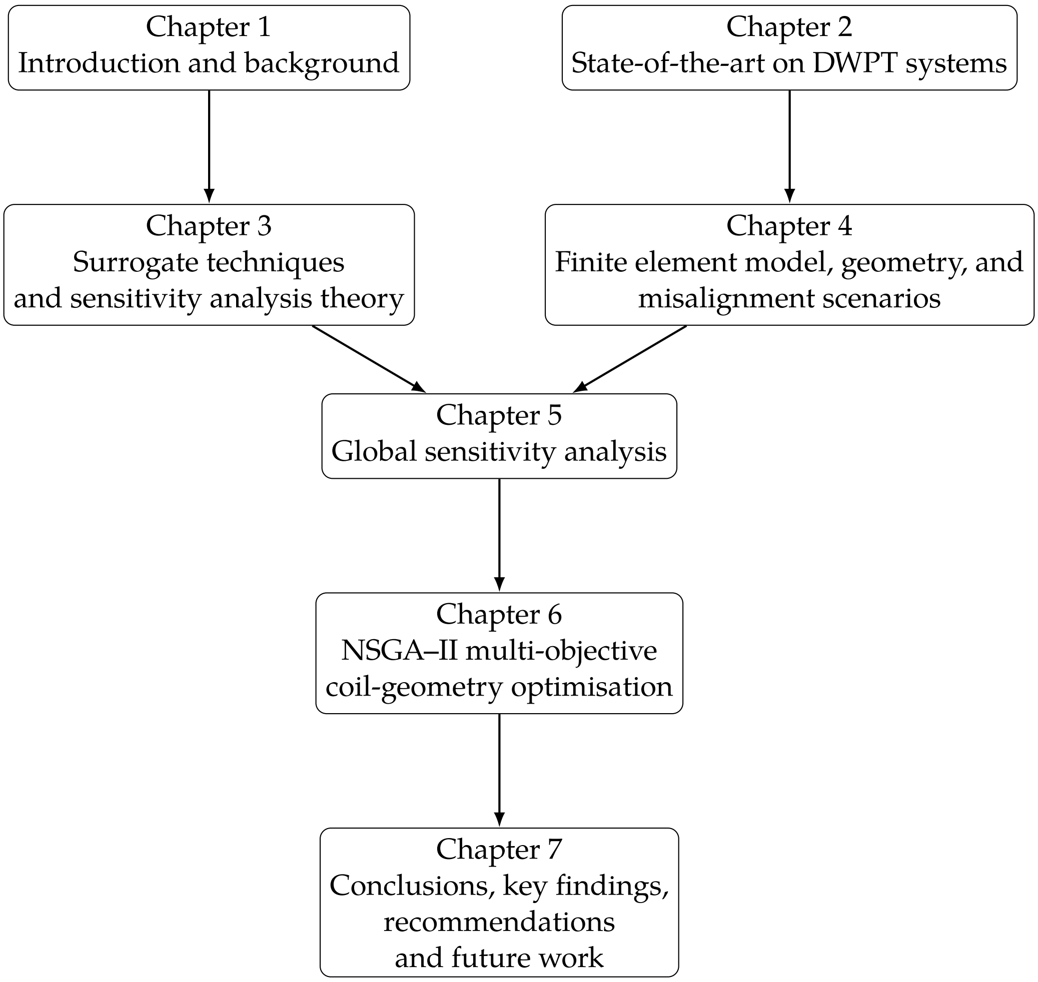


Figure 1.1: Overview of the dissertation structure.

Chapter 1 introduces the motivation and scope of the work. It discusses the role of WPT in the electrification of urban mobility, outlines the research gap addressed in this dissertation, and states the specific objectives related to coil-geometry design, EMF exposure compliance, and robustness to misalignments.

Chapter 2 reviews the state-of-the-art on DIPT systems. It summarises the main wireless power transfer technologies for EVs, the architecture of DIPT couplers and power supply systems, and the compensation networks typically employed. Particular attention is given to efficiency metrics, EMF exposure guidelines, and shielding strategies, as well as to relevant prototypes and experimental projects that inform the design choices adopted in this work.

Chapter 3 introduces the surrogate techniques and global sensitivity analysis tools that are considered and compared for the subsequent study. Several regression-based surrogate models are reviewed, including Gaussian process regression, canonical low-rank approximations, support vector regression, polynomial chaos expansions, and tree-based ensemble methods. The chapter also presents the formulation of variance-based global sensitivity measures, with an emphasis on Sobol' indices and their interpretation for engineering design.

Chapter 4 describes the finite element model developed for the representative DIPT system. The chapter details the coil geometries and optimisation parameters, material and electromagnetic properties, excitation and compensation circuits, and the definition of EMF control planes. In addition, it discusses mesh generation, solver settings, and convergence assessment. The design of experiments adopted to generate the simulation datasets is presented, together with an overview of the simulation campaign and computational resources.

Chapter 5 is devoted to the construction and validation of surrogate models based on polynomial chaos expansions and to the global sensitivity analysis of the coupler geometry. It defines the input and output quantities of interest, the probabilistic characterisation of the design variables, and the sparse PCE construction strategy. The resulting surrogates are then used to estimate Sobol' indices for coupling coefficients and magnetic flux-density metrics on the control planes. The chapter concludes with a discussion of the implications of the sensitivity results, including the identification of the most influential geometric parameters, the trade-offs between efficiency and EMF exposure, and the selection of decision variables for optimisation.

Chapter 6 formulates and solves the EMF-constrained multi-objective coil-geometry optimisation problem. The objectives, constraints and decision variables are stated, and the NSGA–II evolutionary algorithm is introduced as the optimisation engine. The chapter presents the resulting Pareto fronts, performs a trade–off analysis between coupling efficiency and EMF compliance, and uses response surfaces to interpret the behaviour of the initial and optimised designs under misalignments. A detailed comparison between the initial design and the selected optimised configuration is provided.

Finally, Chapter 7 summarises the main findings of the study and reflects on their significance for the design of dynamic inductive power transfer systems for micromobility. It synthesises the contributions related to finite element modelling and EMF constraints, surrogate modelling and global sensitivity analysis, and NSGA–II geometry optimisation. The chapter also discusses the limitations of the present work and outlines recommendations for future research and for the practical design of DIPT systems.

# 2 State-of-the-art on dynamic inductive power transfer systems

## 2.1 Principles of wireless power transfer technologies for electric vehicles

The WPT technology can be classified on the basis of transfer distance and frequency of operation. There are two main groups of technologies: radiative, for considerable distances, and coupling, for short distances (Figure 2.1). Coupling technologies refer to a short transmission distance, transmission being carried out by a magnetic field, IPT or by an electric field, capacitive power transfer (CPT). These types of technologies can be further categorised as non-resonant and resonant [5, 6]. For radiative technologies, there are two main categories that differ in operating frequency: microwave power transfer (MPT) and optical power transfer (OPT) [7].

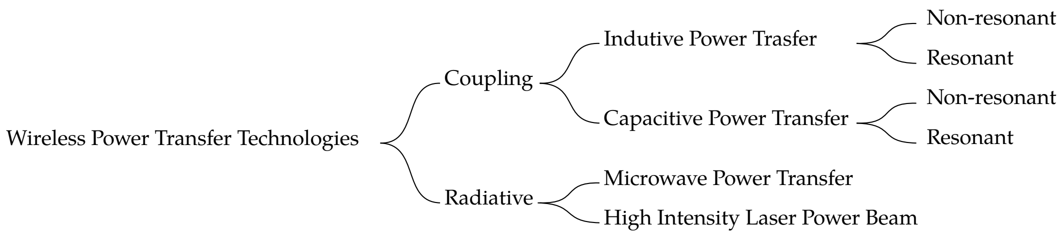


Figure 2.1: Wireless power transfer technologies classification [8].

### 2.1.1 Inductive power transfer

IPT operates on the basis of the generation of an electromagnetic field by a primary coil which induces an electric current in a secondary coil [7, 9]. The primary coil is powered by an inverter operating in the 79 to 90 MHz frequency band, with a standard frequency of 85 MHz defined by SAE J2954 and IEC 61980-3 standards, and by a compensation network, which powers the electric vehicle [3, 5, 10]. The inverter is fed from a DC bus, which, in turn, is fed by rectification of the single-phase or three-phase grid supply. The electromagnetic field (EMF), from which the high-frequency (HF) supply is derived, induces an alternating current in the secondary coil, which is located in the EV and is connected to an AC – DC converter and compensation network. It should be noted that the position and movement of the coils directly affect mutual coupling, affecting the efficiency of the power transfer. Figure 2.2 illustrates a simplified block diagram of an IPT system.

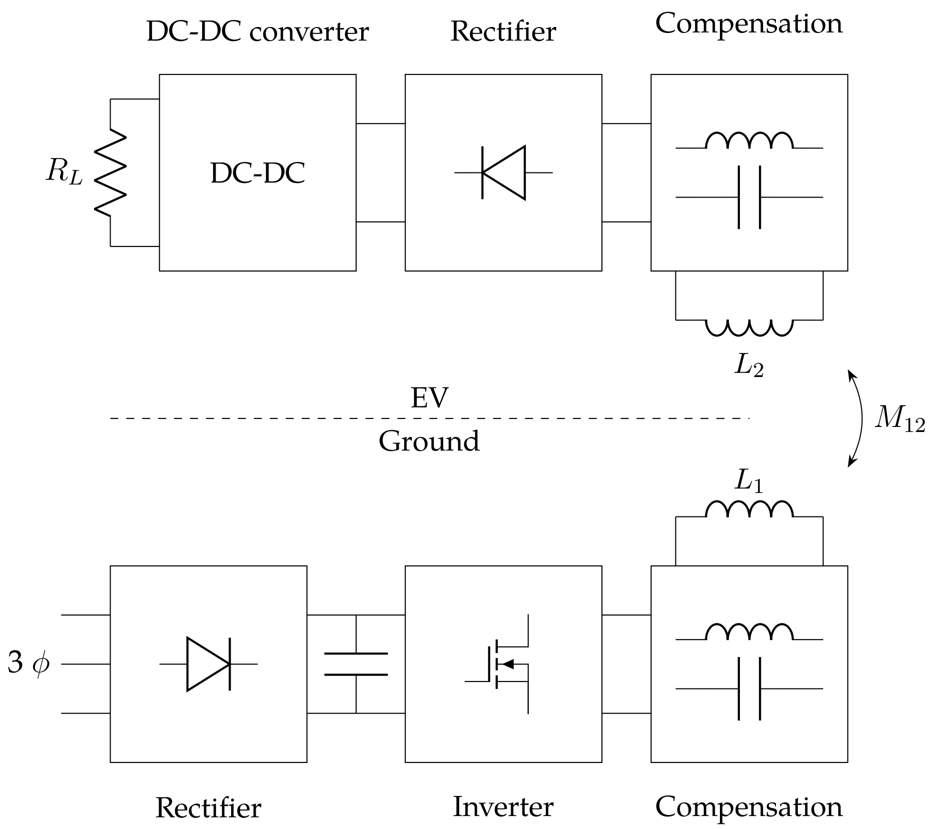


Figure 2.2: High-level block diagram of an IPT system [6].

Resonant inductive power transfer (IPT) differs from non-resonant IPT in that it operates at the same frequency in both the transmitter and receiver, which is an improvement in efficiency and also intolerant of metallic objects [8].

Three categories of IPT systems can be distinguished: stationary, dynamic, and quasi-dynamic. Stationary charging systems, commonly encountered, mostly serve as charging facilities in private garages and public parking bays, subject to the payment of a usage and consumption charge. The IPT system is used to charge a battery on board the EV. When the battery is charged, the vehicle can be driven until the battery reaches a level that requires it to be recharged. Dynamic charging is a process that applies to vehicles in circulation, in which the transmission coils are embedded in the road in a linear configuration that powers the secondary coil in the vehicle. This type of system charges an EV battery normally on fast roads or highways. Quasi-dynamic systems are used to charge EVs when they are opportunely stopped at an intersection, a traffic light, or a bus stop. They are also based on systems with embedded coils positioned where vehicles stop momentarily [5, 11].

### 2.1.2 Capacitive power transfer

CPT is a type of system based on an electric field coupling created between two pairs of plates that act as two capacitors. The plate pairs are subjected to an alternating HF voltage, and a displacement current is generated between them due to the created electric field. The generated current depends on the electric field, the dielectric constant and the area where the current is generated.

This type of system comprises an HF inverter, a compensation network in the transmitter and receiver, and an inverter in the receiver that feeds the EV battery (Figure 2.3). Compensation networks contribute to decreasing system impedance and increasing efficiency.

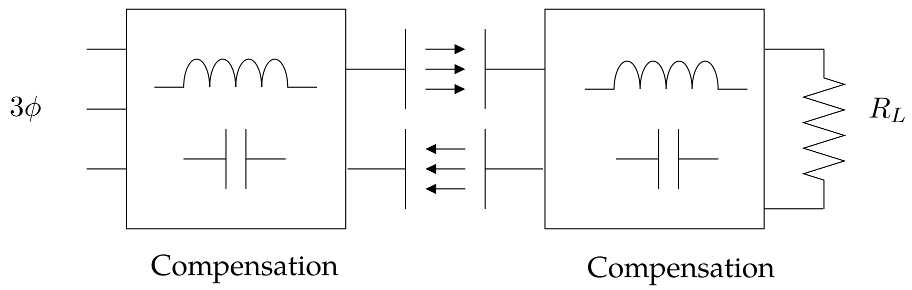


Figure 2.3: High-level block diagram of an CPT system [8].

The cost of this system is lower than the cost of an IPT system, and its efficiency is also lower. It is highly tolerant of misalignment, especially for aluminium pads [7, 9, 12].

There are some disadvantages to this type of technology compared to the others, namely the limited transmission distance between the plates and electrical current leaks that can cause injuries to EV users. For heavy-duty EVs, it may not be a viable system due to the low power per transmissible plate area. This is due to the low capacity because it is a simple coupling with two plates. Some studies suggest increasing the operating frequency as a solution, but the efficiency naturally decreases. There are also issues related to the appearance of metallic obstacles in the coupling area that lead to a reduction in transferred power [9].

### 2.1.3 Microwave power transfer

MPT operates in the microwave or radio frequency band, with the magnetron powered by high-voltage direct current. The signal is transmitted by an antenna and received by a rectenna consisting of an antenna and a rectification stage. The direct current is then converted and feeds a load. Figure 2.4 illustrates a high-level diagram of this system.

It enables the transfer of power on the order of kilowatts over a few kilometres and is applicable to DWPT systems while maintaining compatibility with other communications systems. Nevertheless, it is less efficient than IPT systems and, due to the essentially one-dimensional nature of the power transfer, it does not permit power injection

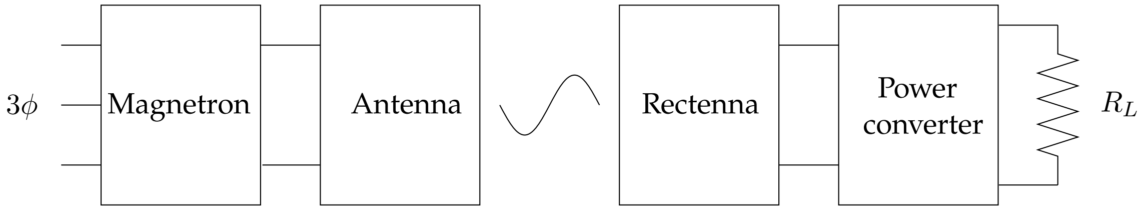


Figure 2.4: High-level block diagram of an MPT system [8].

from the emitter via regenerative braking. Moreover, this type of energy transfer can be harmful to the health of humans and animals upon exposure [7].

### 2.1.4 Optical power transfer

OPT systems are based on the emission of a laser beam, with the receiver consisting of a photovoltaic panel. Power transfer occurs on the order of THz, and it enables the transfer of power on the order of kilowatts over a few kilometres and is applicable to DWPT systems, reduced in size compared to MPT systems. The system consists of a laser diode that is directed at the photovoltaic (PV) panel. The light received on the PV panel is converted into an electric current to power a load. Figure 2.5 represents a high-level diagram of an OPT system [8, 13].

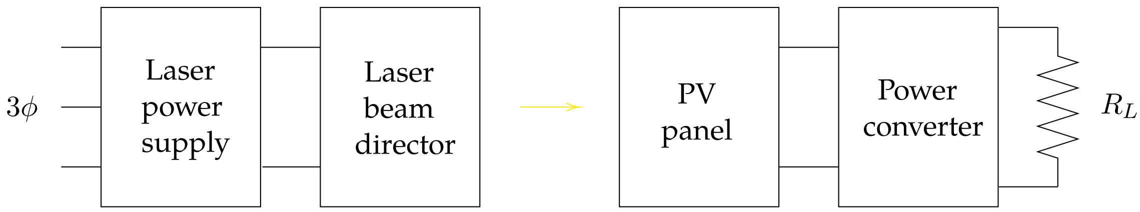


Figure 2.5: High-level block diagram of an OPT system [8].

This type of system require alignment between the laser beam and the PV panel, is intolerant of obstacles, and its efficiency is limited by the PV panel, whose efficiency depends on temperature [7, 8].

### 2.1.5 Comparative analysis and application to dynamic systems

IPT systems present high safety and efficiency along with the possibility of bidirectional transmission, presenting little tolerance to metallic objects, especially resonant IPT systems. Resonant IPT systems face issues with regard to thermal dissipation and magnetic interference. CPT power transfer systems feature lightweight couplers, tolerance to metallic obstacles, and the possibility of bidirectional transmission. MPT is applicable over longer distances and for high-power applications, but has a relatively high cost and does not allow bidirectional transmission.

The aim of this study is to analyse dynamic systems to which inductive technologies are applied. This type of technology offers simplified implementation, galvanic isolation, and high efficiency, along with the possibility of bidirectional energy transfer, which is essential for regenerative braking procedures. Table 2.1 presents a comparison between the categories of technologies applicable to WPT. IPT technology presents a number of engineering challenges: the high cost of coupler manufacturing materials due to the reduction of skin-effect losses; the creation of eddy current losses in adjacent metallic materials, and the fluctuation of the transferred power due to misalignment between the transmitting and receiving coils [8].

Table 2.1: Comparison of coupling and radiative wireless power transfer technologies [7, 8, 14].

| Technology | Coupling | | Radiative | |
|---|---|---|---|---|
| | Inductive | Capacitive | Microwave | Optical |
| Efficiency | 90-95% | 80-90% | 40-50% | 1-15% |
| Power range | 100 kW | 7 kW | 250 W | 500W |
| Frequency | kHz-MHz | kHz-MHz | MHz-GHz | THz |
| Air gap | 30 cm | 30 cm | >1km | >1 km |
| Bidirectional | Yes | Yes | No | No |
| Relative cost | Medium | Low | High | High |

## 2.2 Architecture of dynamic inductive power transfer couplers

The centrepiece of a DIPT system consists of a set of coupled coils commonly referred to as pads. For ground transport infrastructures, the primary coil is road–embedded and the secondary coil is incorporated into the vehicle. The coils have auxiliary equipment that is fundamental to their operation: magnetic material to conduct the magnetic flux and EMF shielding. The coils are made up of low-resistance conductors and allow high inductance, contributing to an increase in the quality factor and efficiency of the system (Subsection 2.4.1) [5].

### 2.2.1 Inductor materials

Coils are composed of conductive materials, ranging from litz wires, magnetoplated wires, magnetocoated wires, tubular conductors, rare-earth barium copper oxide wires (ReBCO), and copper-clad aluminium wires.

Litz wires consist of a multi-stranded wire in which the various copper conductors have their own insulation (Figure 2.6a). The outside of the wire is also insulated (Figure 2.6c). This type of wire is suitable for conducting high-frequency alternating current, and due to its insulated multi-strand design, reduces the skin effect. The skin effect is the increase in current density near the surface of the conductor, causing eddy current losses. Separating the wire into smaller insulated wires reduces the total surface area, resulting in a reduction in losses [15, 16]. The SAE J2954 standard specifically refers to the use of 5 mm diameter litz wire, without specifying the material [3]. This type of conductor is considerably expensive, as it requires the insulation of several conductors and the need to twist the conductors together, which also increases production costs [15].

Magnetoplated wires are multistrand wires in which each conductor consists of a conductive copper core and a thin layer of material with magnetic properties. The layer is composed, from the inside out, of nickel, iron and a layer of insulation (Figure 2.6b). Iron acts as a magnetic conductor, while nickel is present to improve welding performance. The presence of iron increases the inductance of the coil and, therefore, the coupling factor and the efficiency of the system. This type of wire improves magnetic coupling and promotes a reduction in magnetic losses. However, they have a more complex and expensive manufacturing process involving electroplating [7, 17].

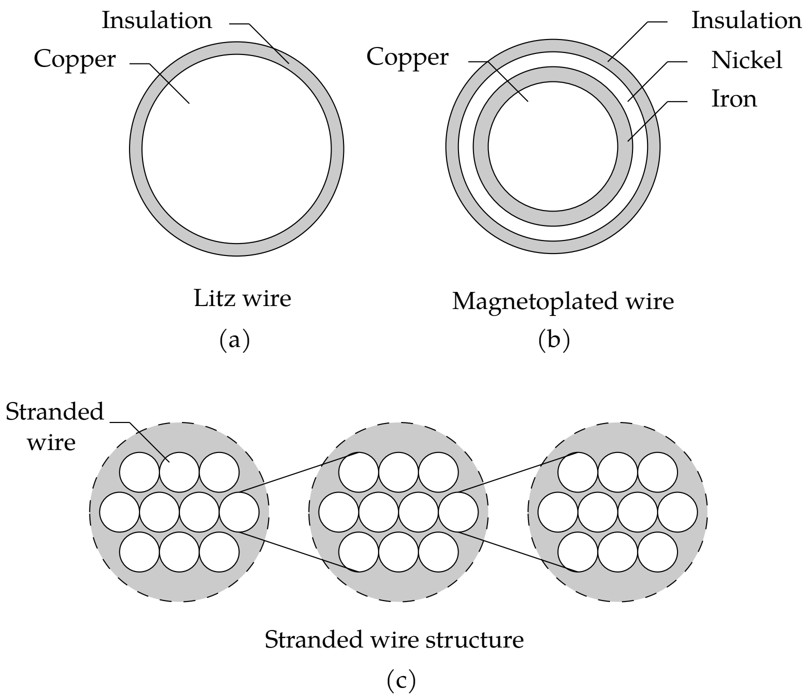


Figure 2.6: Section view of the strucure of a: a) Litz wire; b) Magnetoplated wire; c) Stranded wire structure with parent and child litz wires [7].

Magnetocoated wires differ from magnetoplated wires because of their manufacturing process, using chemical deposition or spray-coating methods. Similarly to the previous type of wire, this improves the magnetic characteristics of the conductor, and the durability of the coating may be lower than that of the magnetoplated wire [7, 17].

Tubular conductors, usually manufactured from copper, have a lower skin effect and a lower conductive area than conductors with the same cross-sectional area. This type of conductor is manufactured by extrusion, with improvements in weight reduction and the possibility of internal cooling (Figure 2.7a). These types of wire are less common for this type of application [18].

ReBCO wires are formed by superconductors resulting from a combination of copper oxide, barium, and rare earths that present a ribbon-shaped shape. The manufacturing process entails epitaxial deposition on a nickel-chromium-molybdenum alloy substrate, usually Hastelloy, which is a registered alloy of Haynes International. The copper, silver and ReBCO layers are deposited sequentially (Figure 2.7b). This type of wire has a quality factor up to 7.2 times higher than copper wire coils, resulting in improved efficiency at temperatures of around 70 K. They require complex cooling systems to maintain the superconductivity characteristics necessary for operation. They are very mechanically fragile compared to the other types of wires mentioned and have a considerable cost. [7, 19, 20].

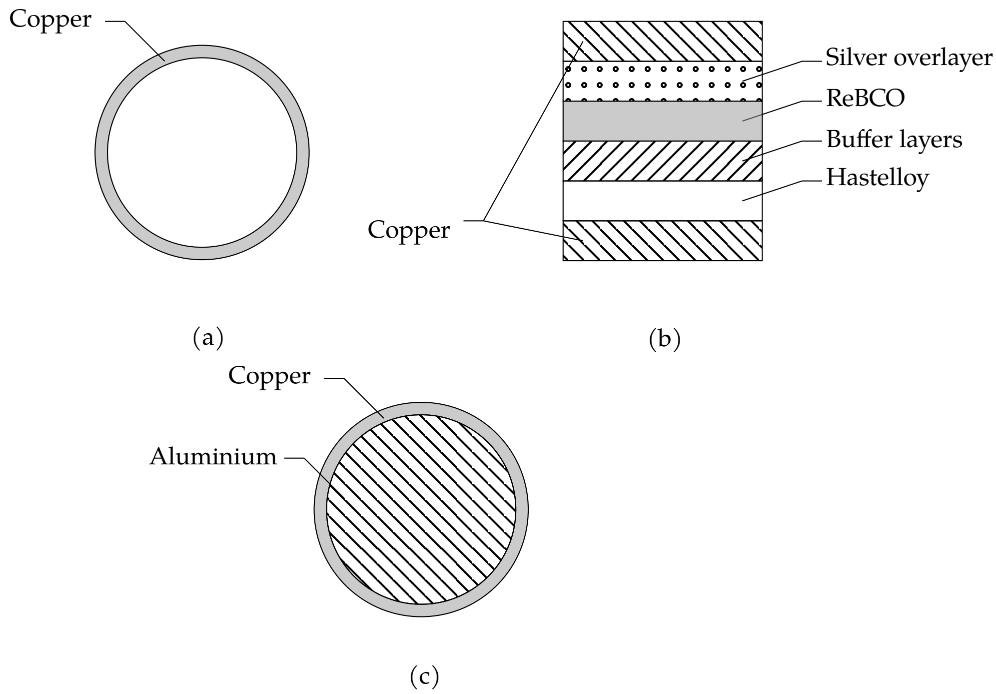


Figure 2.7: Section view of the structure of a: a) Tubular conductor; b) ReBCO conventional wire; c) Copper-clad aluminium wire [19].

Copper-clad aluminium wires are a type of dual metal conductor constructed of an aluminium core and a copper-clad cast cladding (Figure 2.7 c). Manufactured by lamination and extrusion, they are lightweight, suitable for use at high frequencies, and have a lower cost than copper wires [21, 22].

### 2.2.2 Classification of magnetic couplers

Magnetic coupling is a fundamental element in IPT systems and typically consists of a primary coil, a secondary coil, and a shield. The coils are used to transmit power, while the shield helps to improve the distribution of the flux. There are two main types of coil that are applicable to DIPT systems: power track systems and planar coupling-based systems or pad systems [7].

### 2.2.3 Power track systems

Power track systems make use of a track coil along the fixed path of an electric vehicle, which could be an automated guided vehicle (AGV), a railway machine, or an online electric vehicle (OLEV) [23, 24]. This type of transmitter allows more than one vehicle to be powered simultaneously. A single HF inverter and a compensation network power the track coil, ensuring constant mutual inductance in relation to the receiving coil [7].

Features a straightforward coil design with minimal construction complexity [7]. However, this type of coil provides insufficient tolerance for misalignment and is mostly applicable to vehicles travelling on a closed circuit. It has high maintenance costs and high energy losses in power transmission along with significant EMF emissions along the track, when the EV is not covering it [25].

The track coil can be classified according to the design of the magnetic core, which is usually made of ferrite. Initially, types "I", "S", "U" and "W" were proposed for power transmission on tracks [7, 26, 27]. Figure 2.8 represents the four main types of geometry for power tracks.

These types of geometries can be compared according to their EMF leakage, maximum air gap, track width, efficiency, power transfer level, and tolerance to lateral misalignment (Table 2.2).

Table 2.2: Comparison of DIPT power track systems magnetic cores [5, 7, 26, 27].

| Parameters | I-type | S-type | U-type | W-type |
|---|---|---|---|---|
| EMF leakage | Medium | Low | High | Low |
| Air gap size | Considerable | Considerable | Medium | Small |
| Track width | Small | Small | Considerable | Medium |
| Efficiency | High | Low | Low | High |
| Power Transfer Level | High | High | Low | Low |
| Tolerance to lateral misalignment | High | High | High | Low |

The different types of power track systems are designed for specific applications. In general, they have a high cost, mechanical fragility, considerable weight, high maintenance and sensitivity to misalignment, which directly affects the power transferred. They are not a viable alternative to urban transport, where movement is more dynamic and subject to misalignment [8]. In order to overcome these limitations and obtain greater flexibility of movement while maintaining the efficiency of the system, novel types of coils with pad geometry have been developed [7].

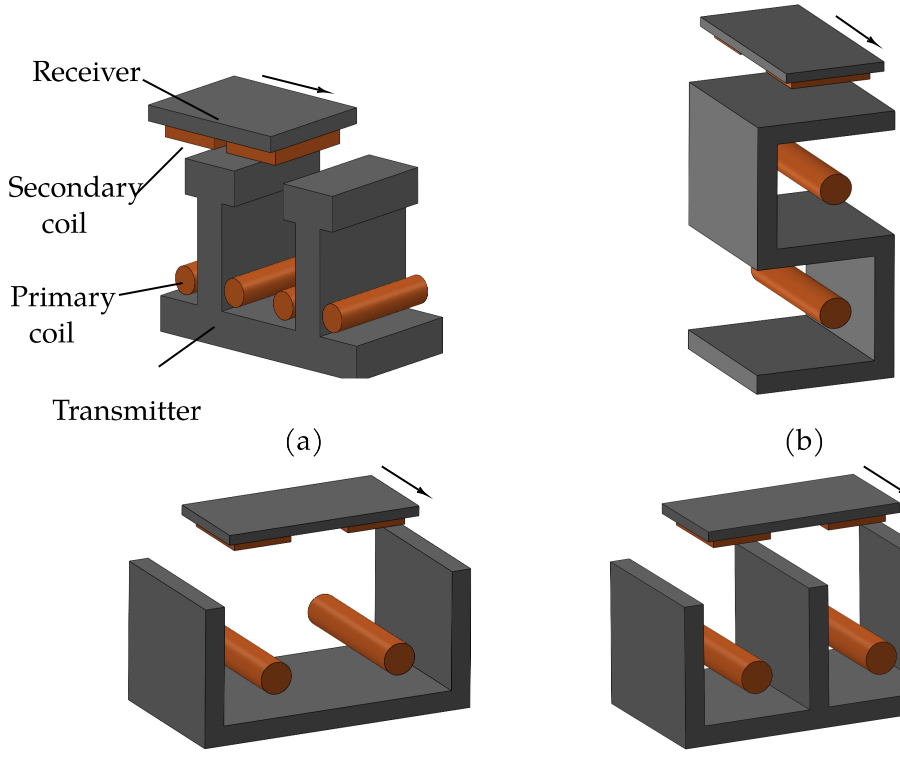


(a) (b)

(c) (d)

Figure 2.8: Power track: a) I-type; b) S-type; c) U-type; d) W-type [7].

### 2.2.4 Magnetic pad couplers

Magnetic pad couplers can be classified according to the magnetic flux generated as non-polarised and polarised pads (Figure 2.9).

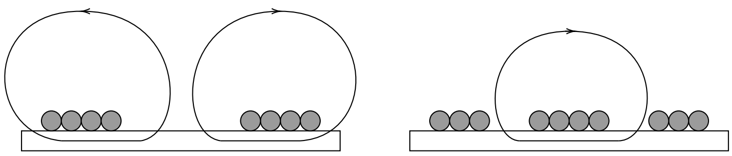

(a) (b)

Figure 2.9: Section view of a coil pad coupler structure: a) Non-polarised; b) Polarised [28].

Non-polarised pads are defined as a single coil with orthogonal magnetic flux to the plane of the pads resulting from the central magnetic pole and the opposite magnetic pole around the outside of the coil (Figure 2.9a). Some examples are circular, square, and rectangular pads. Polarised pads generate orthogonal and parallel magnetic flux to the plane of the pads (Figure 2.9b). This type of pad has opposite magnetic poles on the same orthogonal line resulting from double-D or double-D quadrature geometry, for example [28].

The magnetic field created in a non-polarised coil is orthogonal to the plane of the pads, and the magnetic field created in a polarised coil is parallel to them. Thus, coupling will occur between a non-polarised and a polarised coil if both are centred [28].

Circular, square, and rectangular pads were among the earliest types of pads to be studied, and many variants of these designs have been found with optimised ferrite geometries to direct magnetic flux and increase efficiency while reducing EMF leakage. Circular pads are the most common and least complex to construct, allowing considerable power transfer (Figure 2.10a). They have limited tolerance for misalignment, which is reflected in a reduction in the power transferred, so their application to dynamic systems is more limited. High EMF leakage, requiring improved shielding. This type of coil is normally used as a transmitter for stationary systems. Square pads are suitable for DIPT, being interoperable with circular pads and moderately tolerant of misalignment. Regarding EMF leakage, shielding is necessary and has been shown to be effective (Figure 2.10b) [7, 29].

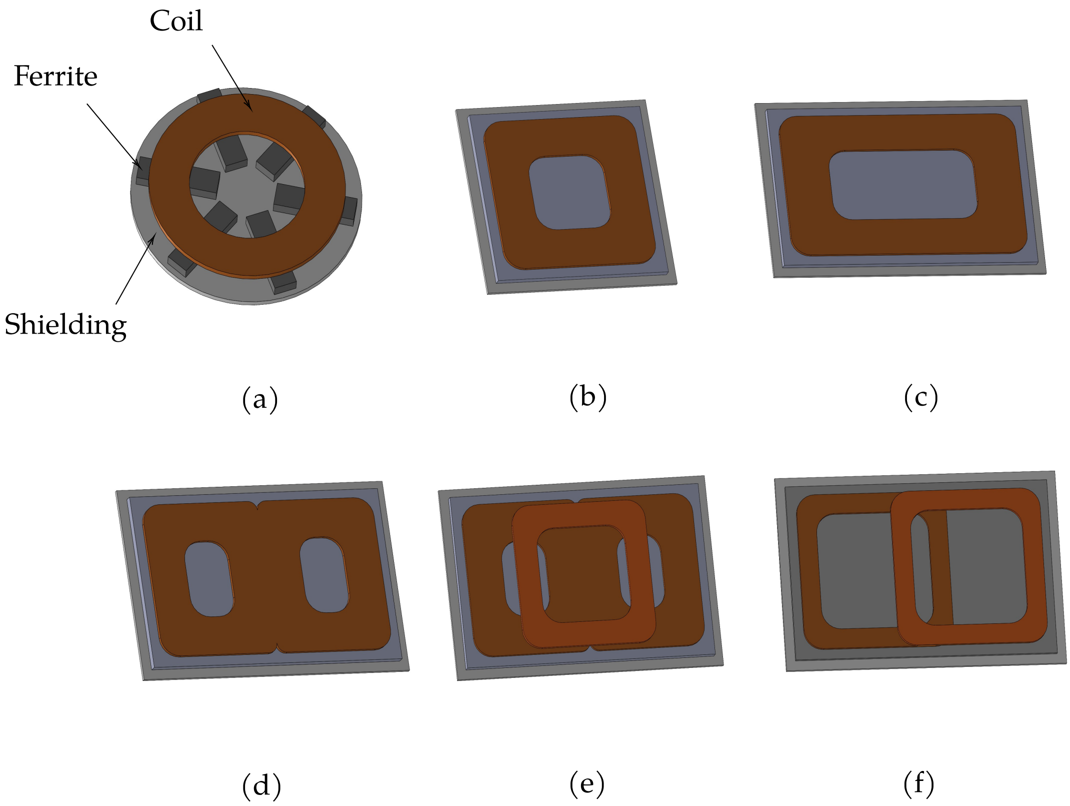


Figure 2.10: Magnetic pads: a) Circular; b) Square; c) Rectangular; d) Double-D; e) Double-D quadrature; f) Bipolar [9].

Rectangular pads have moderate tolerance to misalignment and the shielding has some influence on the transmitted power. Significant EMF leakage, requiring optimised shielding. It is applicable to short transmission distances, can be used both as a transmitter and receiver, and is suitable for DIPT [7, 30].

Double-D (DD) pads consist of two oposite adjacent coils, allowing energy transmission over an improved distance and moderate misalignment tolerance. It is usually only applicable as a transmitter coil and is not interoperable with non-polarised pads. This design features extremely low EMF leakage. However, DD pads have a coupling null point which limits power transfer and their tolerance to horizontal misalignment. To overcome this limitation, the Double-D quadrature (DDQ) pad was developed, which consists of placing a coil decoupled from the previous two, improving tolerance to horizontal misalignment [29].

Bipolar pads (BP) represent a simplified version of the DDQ, consisting of two overlapping rectangular coils. It offers similar improvements to the DDQ, but requires less complex fabrication and reduces the amount of material required. The mutual decoupling between the coils forming BP improves the distribution of the magnetic flux and tolerance to misalignment [8].

## 2.3 Structure of power supply systems

DIPT systems deliver energy to electric vehicles while they are in motion, enabling a substantial reduction in the required capacity of the on-board battery and thereby lowering vehicle cost, size and weight. In such systems, grid frequency power is processed by a chain of converters comprising a rectifier, power–factor–correction stage, and HF inverter on the transmitter side, together with a rectifier and DC–DC converter on the vehicle, so that the road-embedded track is energised by a controlled HF AC current [5, 31].

From the viewpoint of the ground infrastructure, two main classes of DIPT power supply architecture can be identified, depending on how the transmitter coils are arranged and energised [5, 31]. In the long–track configuration Figure 2.11a, a single extended transmitting conductor, typically tens of metres in length, is fed from a central resonant network and HF inverter, allowing several vehicles to be charged simultaneously as they traverse the instrumented lane, but at the expense of higher reactive power and more pronounced spatial variation of the transferred power [5, 31].

Alternatively, segmented coil architectures partition the roadway into multiple shorter transmitter pads whose dimensions are comparable to those of the vehicle-side receiver pad; at any instant only the segment(s) beneath the vehicle are energised, which improves utilisation of the installed infrastructure and mitigates leakage-field emissions [5]. When segmented coils are used, two main supply arrangements are commonly discussed, as illustrated in Figure 2.11b and Figure 2.11c.

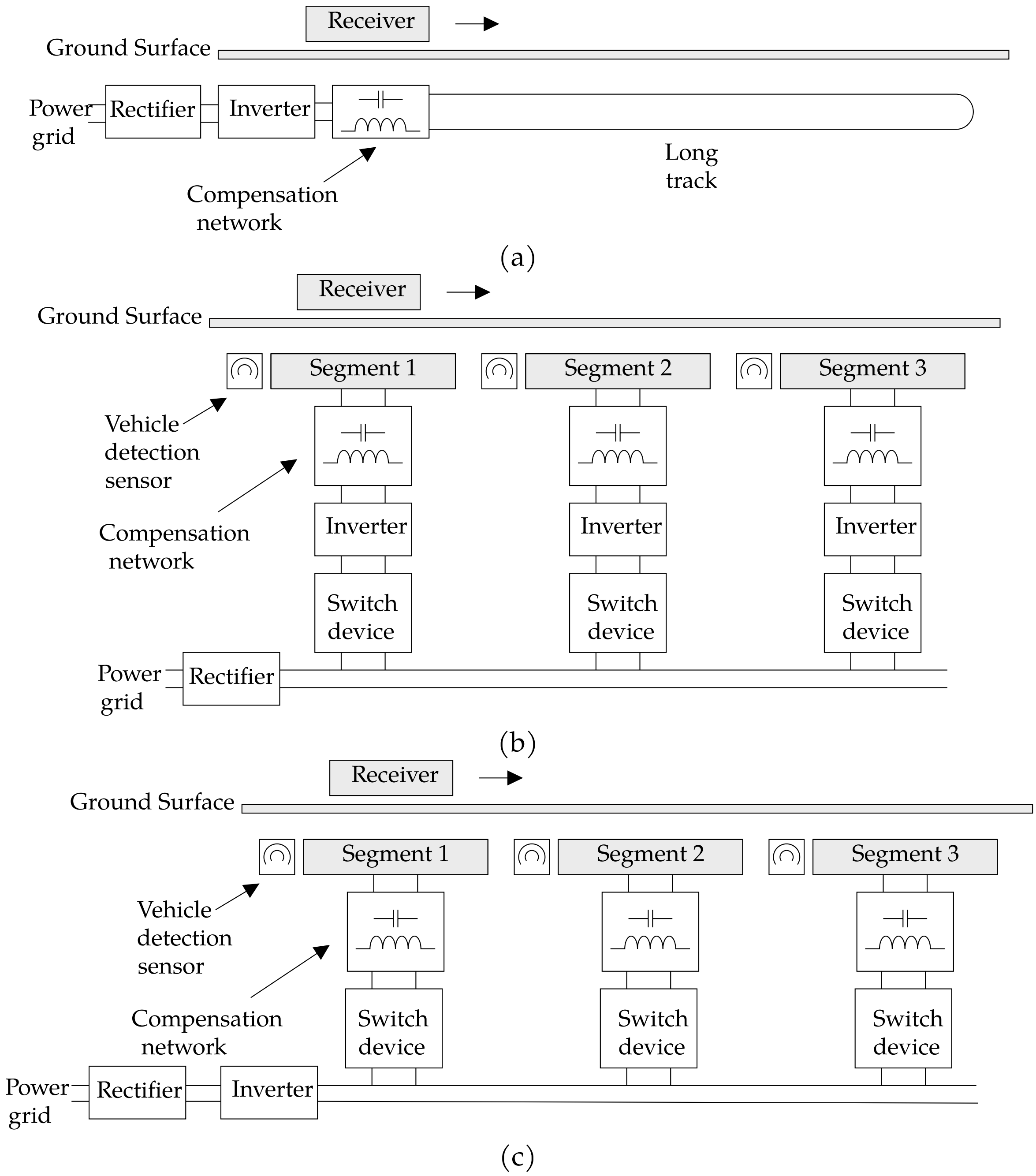


Figure 2.11: Different power supply configurations for DWPT systems: a) Long track; b) Common DC–bus; c) Common HF AC–bus [5, 31].

In the common DC–bus arrangement, a front–end rectifier establishes a DC backbone from which individual HF inverters or switching converters feed each segment, enabling independent activation and precise power control at the cost of multiple power-electronic stages and high–voltage DC cabling along the track [5].

In the common HF AC–bus arrangement, a single HF inverter supplies a bus that is routed along the track, while local switches and compensation networks connect the selected segment(s) to the bus. This reduces the extent of DC cabling and can simplify protection, but imposes tighter constraints on the design of the HF bus and on the impedance of the segments to maintain efficiency and EMC performance [5, 31].

The choice between long–track and segment architectures and between common DC–bus and common HF AC–bus supplies represents a system level trade–off between infrastructure cost, converter complexity, controllability of power flow, and the ability to satisfy electromagnetic-field exposure limits along the roadway [5, 31].

## 2.4 System efficiency

DIPT systems can be decomposed in a sequence of energy-processing stages from the electrical source to the load (end-to-end). This sequence is composed of the inverter and respective clock, power amplifier, coupled coils, rectification and regulation stage. Figure 2.12 provides this cascade and the associated stage efficiencies.

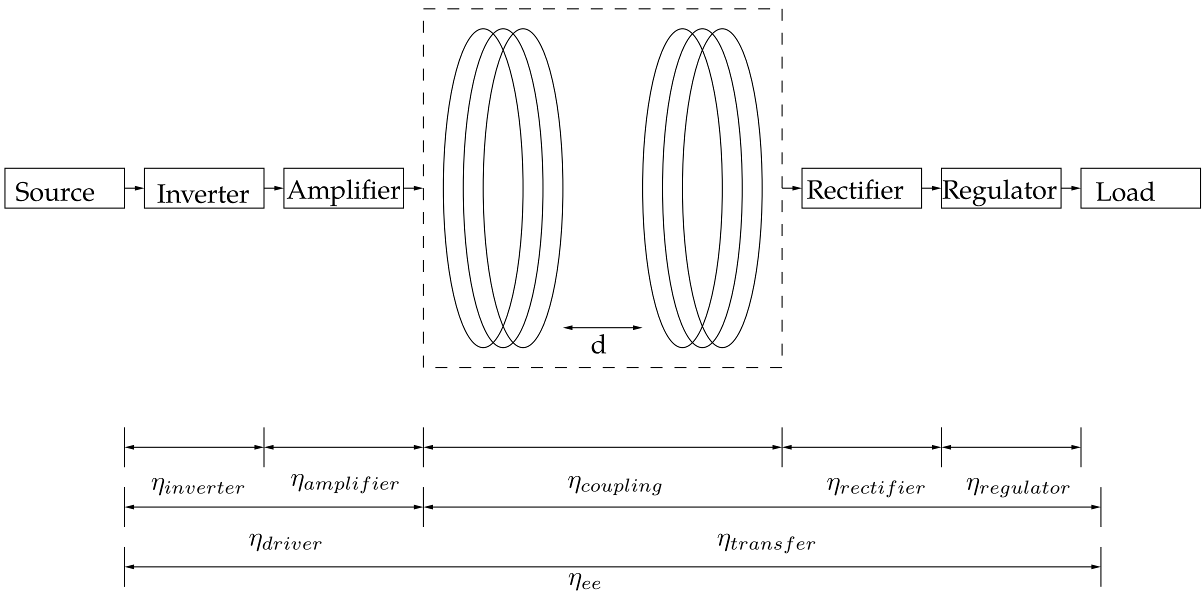


Figure 2.12: Different power supply configurations for DWPT systems: a) Long track; b) Common DC-bus; c) Common HF AC-bus [32, 33]

The end-to-end efficiency may be expressed as the product of stage efficiencies (Equation 2.1).

$$\eta_{ee} = \eta_{inverter}\,\eta_{amplifier}\,\eta_{coupling}\,\eta_{rectifier}\,\eta_{regulator} \tag{2.1}$$

Each efficiency $\eta_i = P_{out,i}/P_{in,i}$ is defined at the electrical interfaces indicated in the diagram. Inverter and amplifier efficiencies can be grouped as a driver efficiency. In the same way, coupling, rectifier, and regulator efficiencies can be grouped as a transfer efficiency. However, the mathematical identity remains unchanged.

This dissertation focusses exclusively on coupling efficiency as the fraction of high-frequency AC power injected into the primary coil as it is delivered to the secondary coil. The electromagnetic coupling embodies the principal design levers relevant to geometry, spacing and misalignment tolerances, shielding materials, and induced-loss mechanisms, which are central to the DIPT project for micromobility. For this study, frequency, compensation topologies and load conditions are fixed for comparability purposes and to allow a sensibility analysis and comparative study. Section 2.4.1 develops the formal definition of $\eta_{coupling}$.

### 2.4.1 Coupling efficiency

An IPT system can be modelled by a circuit in which the primary coil $L_1$, powered by an alternating voltage source, induces a current in the secondary coil $L_2$. The resistance of the primary and secondary coils is given by $R_1$ and $R_2$, respectively. Figure 2.13a represents the model of the IPT system [32].

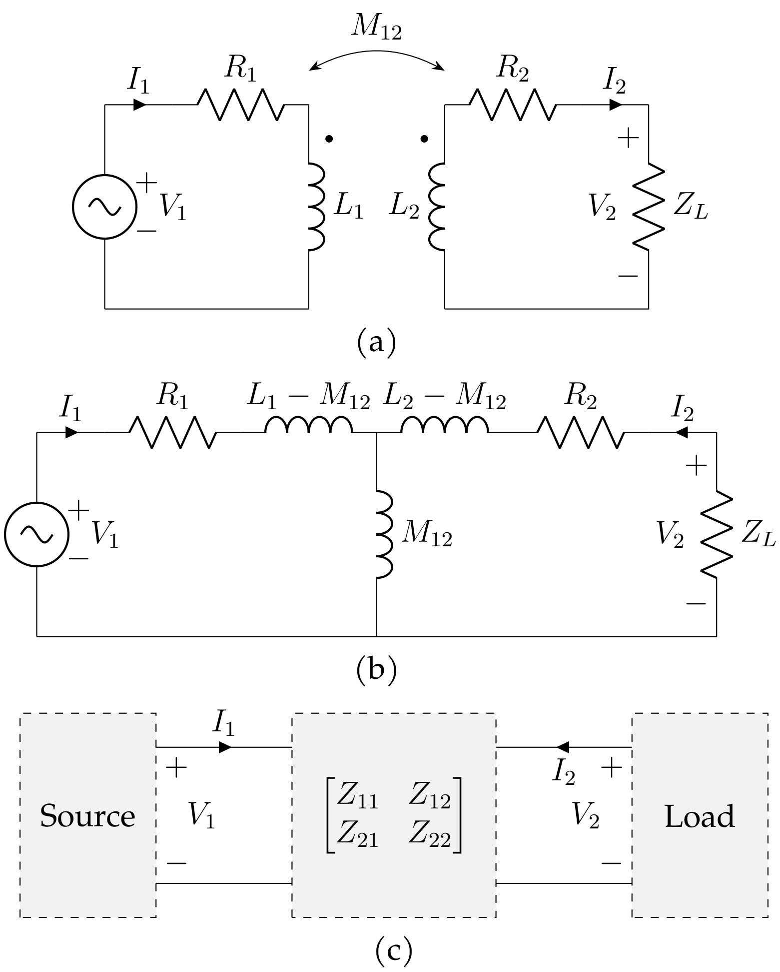


Figure 2.13: IPT system: a) Circuit model; b) Equivalent T-model; c) Simplified two-port model [32].

Considering that $M_{12}$ represents mutual inductance, the source and load voltages can be written as a function of the system impedances, according to the T-model and the simplified two-port network model in Figures 2.13b and 2.13c, respectively. Equation

2.2 represents the voltages in the system.

$$\begin{bmatrix} V_1 \\ V_2 \end{bmatrix} = \begin{bmatrix} R_1 + j\omega L_1 & j\omega M_{12} \\ j\omega M_{12} & R_2 + j\omega L_2 \end{bmatrix} \begin{bmatrix} I_1 \\ I_2 \end{bmatrix} = \begin{bmatrix} Z_{11} & Z_{12} \\ Z_{21} & Z_{22} \end{bmatrix} \begin{bmatrix} I_1 \\ I_2 \end{bmatrix} \tag{2.2}$$

The coupling between the primary and secondary coils is characterised by the coupling coefficient $\kappa_{12}$ given by the equation 2.3 [32].

$$\kappa_{12} = \frac{M_{12}}{\sqrt{L_1 L_2}} \tag{2.3}$$

In addition, the transmission efficiency is directly influenced by the ratio between the transmitted energy and the energy dissipated in the coil, given by the quality factor. The quality factor is a dimensionless value that depends on the inductive reactance and the resistance of the coil. Transmission efficiency is improved for a higher quality factor. Equation 2.4 represents the quality factor [34, 35].

$$Q = \frac{X_L}{R_L} = \frac{\omega L}{R_L} \tag{2.4}$$

The efficiency of a coupling in an IPT system is given by Equation 2.5 [32].

$$\eta = \frac{P_{out}}{P_{in}} = \left| \frac{Z_{12}}{Z_L + Z_{22}} \right|^2 \frac{R_L}{R_1 + \frac{\omega^2 M_{12}^2 (R_2 + R_L)}{(R_2+R_L)^2 + (X_2+X_L)^2}} \tag{2.5}$$

Therefore, the maximum efficiency for an IPT system with series-series compensation (SS) is given by Equation 2.6.

$$\eta_{max} = \frac{\kappa_{12}^2 Q_1 Q_2}{\left(1 + \sqrt{1 + \kappa_{12}^2 Q_1 Q_2}\right)^2} \tag{2.6}$$

Equations 2.3 and 2.6 summarise the classical two–coil analysis of an SS–compensated IPT link, in which the transfer efficiency is governed by the coupling coefficient $\kappa_{12}$, the coil quality factors and the load electrical characteristics [32]. However, in the present study these expressions are used only to set the theoretical background, because performance evaluation focusses on the magnetic coupling between the coils rather than on the closed–form efficiency formulas. The coupler under study forms part of a dynamic system with two primary coils and a single secondary coil, so the power transfer along the track results from a sequence of primary–to–secondary couplings, for which the simple two–coil efficiency expression in Equation 2.6 is no longer directly applicable.

In the DIPT model considered in this work, two identical primary coils are placed symmetrically with respect to the secondary coil. For each misalignment condition, the finite element model provides the coupling coefficients $k_{11,2}$ and $k_{12,2}$ between the secondary winding and each of the two primary windings. Similarly to other DIPT designs with modular and identical transmitting coils, the coupling coefficient of each primary with the receiver exhibits a repetitive pattern along the charging lane, often referred to as a mutual-inductance cycle. In the present configuration, the simulated curves for $k_{11,2}$ and $k_{12,2}$ are numerically similar, as expected from symmetry. Consequently, geometry level analysis is carried out by plotting and comparing the two coupling coefficients separately, without introducing an additional aggregated coefficient. This choice emphasises the physical interpretation of each primary–secondary coupling and is sufficient for assessing how coil geometry and misalignment affect the magnetic coupling in the symmetric two-primary module.

Although the two primary coils are geometrically identical and placed symmetrically with respect to the secondary coil, both coupling coefficients $k_{11,2}$ and $k_{12,2}$ were extracted from the finite element model for each misalignment condition. From a theoretical point of view, the two curves are expected to coincide; however, computing both coefficients provides a useful numerical consistency check of the 3D model, ensuring that the mesh, boundary conditions and coil connections preserve the intended symmetry. Since the two quantities are obtained from the same field solution, the additional computational cost is negligible compared with the cost of solving the electromagnetic problem itself.

## 2.5 Compensation networks

Compensation networks are applicable IPT and DIPT systems, with the aim of minimising magnetic flux leakage and reactive power in order to increase efficiency, transferred power, and system stability. The parasitic capacitance is not sufficient to maintain resonance between the two coils. Compensation networks are therefore fundamental to power transfer and are incorporated into the transmitter and receiver circuits.

### 2.5.1 Basic compensation networks

The basic compensation networks, which are implemented by adding a capacitor in series or parallel to the transmitter and receiver circuits. There are four basic compensation topologies to refer to depending on the position of the capacitor in the transmitter and receiver circuit: series-series (SS), series-parallel (SP), parallel-series (PS), and parallel-parallel (PP) [8]. Figure 2.14 represents the four basic compensation networks, where $M_{12}$ represents mutual inductance, $R_1$, $L_1$ and $R_2$, $L_2$ represent the resistance and inductance of the primary and secondary coils, respectively. $C_1$ and $C_2$ represent the compensation capacitors of the transmitter and receiver circuits, respectively.

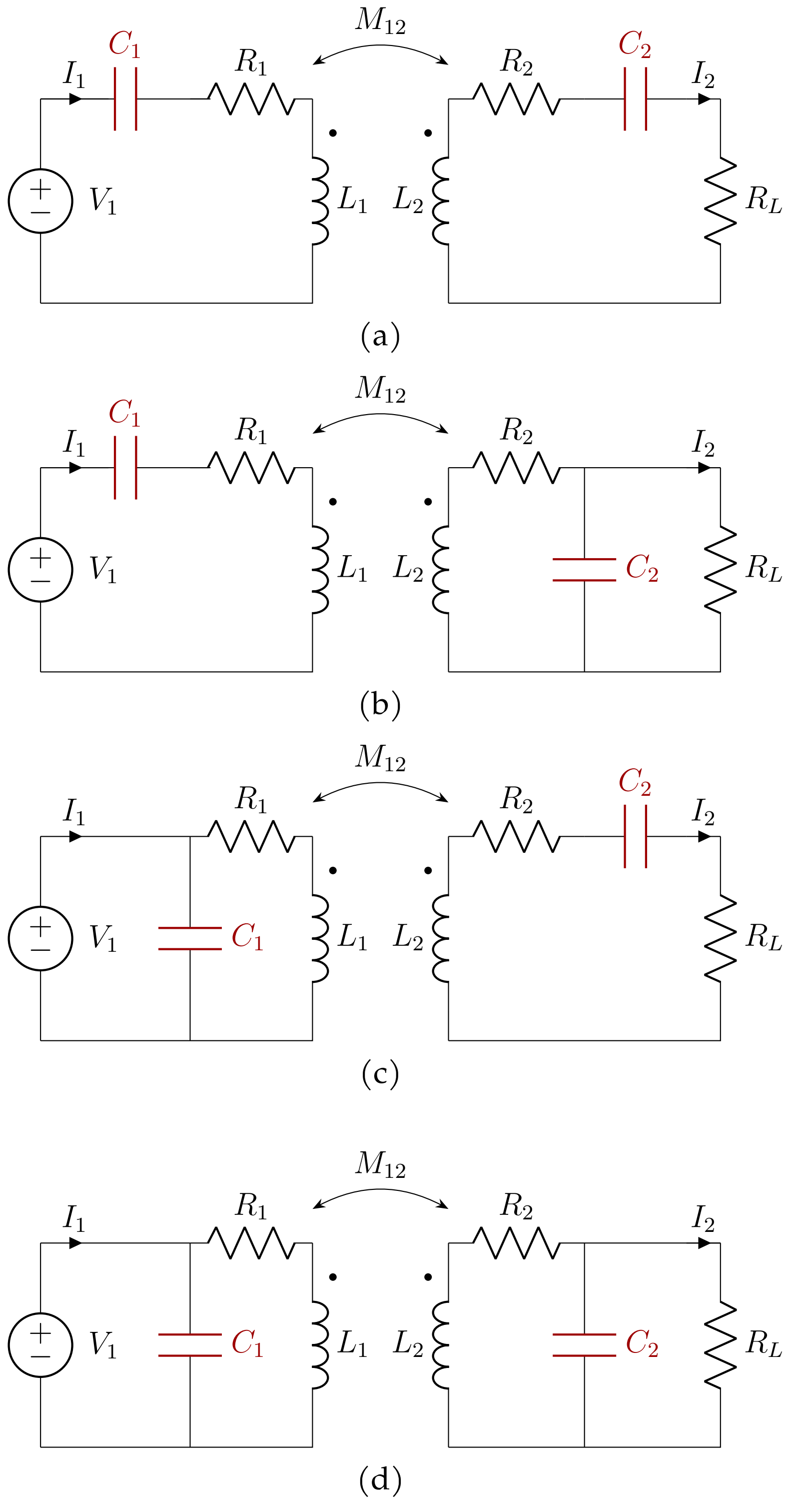


Figure 2.14: Basic compensation networks: a) SS; b) SP; c) PS; d) PP [7].

Table 2.3 presents the relationship between the compensation capacitances and the design variables of the transmitter and receiver. In the SS topology, the compensation capacitance of the transmitter and receiver depends directly on the desired resonance frequency and the inductance of the primary coil, and is independent of the coupling coefficient and the load. Thus, the capacitance is moderately dependent on misalignment. In the SP topology, the capacitance of the transmitter depends on the resonance frequency, the inductances of the primary and secondary coils, and the mutual inductance. It is a moderately sensitive strategy to misalignment. The PS topology depends on the resonance frequency, the inductance of the primary coil, the mutual inductance, and the load resistance. Since it depends directly on the receiver system, it is very sensitive to misalignment. The PP topology depends on the variables mentioned for the PS topology and also on the inductance of the secondary coil, and is also very sensitive to misalignment.

Table 2.3: Parameters for determining the capacity of capacitors for basic compensation networks [7, 8].

| Topology | Primary capacitance | Secondary capacitance |
|---|---|---|
| SS | $C_1 = \dfrac{1}{\omega^2 L_1}$ | $C_2 = \dfrac{1}{\omega^2 L_2}$ |
| SP | $C_1 = \dfrac{L_2}{\omega(L_1 L_2 - M_{12}^2)}$ | $C_2 = \dfrac{1}{\omega^2 L_2}$ |
| PS | $C_1 = \dfrac{L_1 + \omega^2 R_L}{\omega^2(\omega^2 M_{12}^4 + L_1^2 + \omega^2 L_1 R_L)}$ | $C_2 = \dfrac{1}{\omega^2 L_2}$ |
| PP | $C_1 = \dfrac{L_2^3(L_1 L_2 - M_{12}^2)}{(L_1 L_2 - M_{12}^2)^2 \omega^2 L_2^2 + M_{12}^4 R_L^2}$ | $C_2 = \dfrac{1}{\omega^2 L_2}$ |

Basic compensation topologies depend on variables that are not stable, which explains the reason why these systems underperform in the conditions for which they were designed.

## 2.6 Safety and electromagnetic field exposure

WPT and DWPT systems have associated EMF leakages as a result of the inherent energy transfer method [36]. The impact of these emissions should be minimised through construction solutions or shielding and should always be accurately quantified according to the applicable guidelines. EMF emissions have significant biological impacts, especially on human health. This type of emission is categorised as non-ionising radiation, forming part of the spectrum that does not have enough energy to produce ionisation in matter. Exposure to EMF emissions can be categorised as direct, when the fields interact with the body, or indirect, when the body interacts with conductive materials that have a different electrical potential relative to the body. The International Commission on Non-Ionizing Radiation Protection (ICNIRP) 2010 guidelines state that, for frequencies above 100 kHz, there is an increase in the temperature of biological tissues exposed to EMF emissions [37]. It also mentions a feeling of "warmth" when there is exposure to 10 kHz EMF emission, along with effects in the nervous system [37, 38]. Exposure to non-ionising radiation has effects on fertility, brain function, human behaviour, and the functioning of the cardiovascular system [39].

There are numerous international standards, guidelines, and recommendations that recommend limits on exposure to non-ionising radiation and subsequent absorption by the human and animal body. The absorption of non-ionising radiation by biological tissues can be accounted for by the Specific Absorption Rate (SAR), which is defined as the time derivative of the incremental energy consumption by heat $dW$, absorbed or dissipated by an incremental mass $dm$. The mass of biological tissue can be given as a function of its density $\rho$, contained in a given volume $dV$ (Equation 2.7). SAR represents the energy absorbed per unit mass, the unit of which can be expressed as $W/kg$ [38].

$$SAR = \frac{d}{dt} \cdot \left(\frac{dW}{dm}\right) = \frac{d}{dt} \cdot \left(\frac{dW}{\rho \cdot dV}\right) \tag{2.7}$$

Biological tissues have substantial dielectric losses and unitary magnetic permeability and do not significantly interfere with magnetic fields. By deriving Equation 2.7, it is possible to obtain a simplified expression for SAR (Equation 2.8).

$$SAR = \frac{\sigma \cdot |E|^2}{\rho} \tag{2.8}$$

The conductivity and density of biological tissues are represented by $\sigma$ and $\rho$, respectively. $E$ represents the root mean square (rms) electric field in the interior of the biological tissue [38].

The increase in temperature in biological tissues is directly correlated with SAR and is given by Equation 2.9, where $c$ is the specific heat capacity of the tissue, $T$ is the temperature and $t$ is the time.

$$SAR = c\frac{dT}{dt} \tag{2.9}$$

To address technical challenges related to EMF emissions from WPT systems, some regulatory entities have established values to limit the effects on human health. ICNIRP 2010 guidelines set limits, in a range from 1 Hz to 100 MHz, for time-varying magnetic and electric fields. They refer to general public exposure limits and occupational exposure limits. General public exposure limits refer to the exposure of individuals of varying ages and health status who are unaware of their exposure to EMF. This type of condition requires the adoption of stricter limits compared to the occupational exposure of workers. Occupational exposure limits refer to adults working in a regular workplace, working under known and controlled exposure conditions. Generally, the regulatory limits for this type of exposure are higher than those for the general public.

Considering that IPT systems operate in the 3 kHz to 10 MHz band, the ICNIRP 2010 guidelines establish maximum limits for the root mean square electric field inside the biological tissues of the head and body, for general public and occupational exposure. Table 2.4 represents these maximum limits (root mean square), where $f$ represents the field frequency [37].

Table 2.4: Basic restrictions for human exposure of all tissues of head and body to time-varying electric and magnetic fields established in the ICNIRP 2010 guidelines [37].

| Exposure characteristic | Internal electric field $E$ $(V/m)$ |
|---|---|
| General public exposure | $1.35 \times 10^{-4} \cdot f$ |
| Occupational exposure | $2.7 \times 10^{-4} \cdot f$ |

Considering that the WPT operating frequency range covered by the ICNIRP 2010 guidelines is between 3 kHz and 10 MHz, there are exposure limits defined according to the electrical and magnetic properties of the EMF field. Limits for these properties are established for the general public and types of occupational exposure. Table 2.5 represents the electric field strength, magnetic field strength, and magnetic flux density limits established by the ICNIRP 2010 guidelines, which must be respected when designing WPT systems [37].

Table 2.5: General public exposure limits established in the ICNIRP 2010 guidelines for frequencies between 3 kHz to 10 MHz [37].

| Reference levels | General public limits |
|---|---|
| Electric field strength $E$ $(V/m)$ | 83 |
| Magnetic field strength $H$ $(A/m)$ | 21 |
| Magnetic flux density $B$ $(\mu T)$ | 27 |

IEEE C95.1-2019 standard establishes exposure limits for the general public, setting regulatory root mean square levels for the strength of the electric field, the strength of the magnetic field and the density of the magnetic flux for specific areas of the human body (Table 2.6) [40].

Table 2.6: General public exposure limits established in the IEEE C95.1-2005 standard for frequencies between 3.35 kHz to 5 MHz and between 3 kHz to 100 kHz [40].

| Frequency range | 3.35 kHz to 5 MHz | | 3 kHz to 100 kHz |
|---|---|---|---|
| Body parts | Head and torso | Limbs | Whole body |
| Electric field strength $E$ $(V/m)$ | | | 614 |
| Magnetic field strength $H$ $(A/m)$ | 163 | 900 | |
| Magnetic flux density $B$ $(\mu T)$ | 205 | 1130 | |

The indicated values are higher than ICNIRP's. Furthermore, this IEEE regulation is not binding on the European Union, but is valid for the United States of America and other countries that follow IEEE standards. It should be emphasised that Directive 2013/35/EU transcribes the limits indicated in the ICNIRP 2010 guidelines, making it binding to the European Union [41]. Directive 2013/35/EU was transposed into Portuguese law by Law 64/2017 of 7 August [42].

However, the guidelines and directives covered until now focus on general public and occupational limits and are not directly related to the occupation of EVs, pedestrians, or cyclists in the surroundings or interference with implanted medical devices. They must, however, be observed during the design and production process of EVs with WPT. The SAE J2954, IEC 61980 and ISO 19363 standards stand out in this regard, as they present guidelines focused on the automotive sector, regulating emissions and exposure to EMF for stationary WPT systems.

Despite the fact that the SAE J2954 standard is not binding in the European Union, it is recognised internationally as a technical reference and follows the ICNIRP 2010 guidelines and the IEEE C95.1-2019 standard. The SAE J2954 standard establishes an industry-wide specification that establishes criteria for interoperability, electromagnetic compatibility, EMF exposure and emissions, minimum performance, safety and testing for WPT systems. The standard outlines regulations on EMF emission and exposure for EVs with input power up to 11.1kVA. It also establishes regulatory limits for EMF exposure for implanted medical devices (IMD) and other cardiac implantable electronic devices (CIED) [3].

Three regions are defined in relation to EV, according to the SAE J2954 standard, where different regulatory limits are applied for exposure to EMF (Figure 2.15).

Region 1 is the entire are underneath the vehicle, including the wireless power assemblies and the surroundings, not extending beyond the structure of the lower body. Region 2 is the peripheral region of the vehicle, with the border with region 1 extending vertically down the side of the vehicle to the ground surface. Region 3 is the interior of the vehicle.

Region 1 requires increased safety measures to prevent human exposure to values higher than those mentioned in Table 2.7. Prevention of exposure requires active or passive measures to restrict access to the energy transfer zone of the WPT system. Alternatively, the system should be equipped to detect and deactivate in the presence of humans to prevent exposure, taking into account the speed of approach specific to each class of the system. Compliance with the regulatory limits outlined in Table 2.7 during normal operations is essential in the absence of previous security measures. Regions 2 and 3 must comply directly with the regulatory limits defined in Table 2.7.

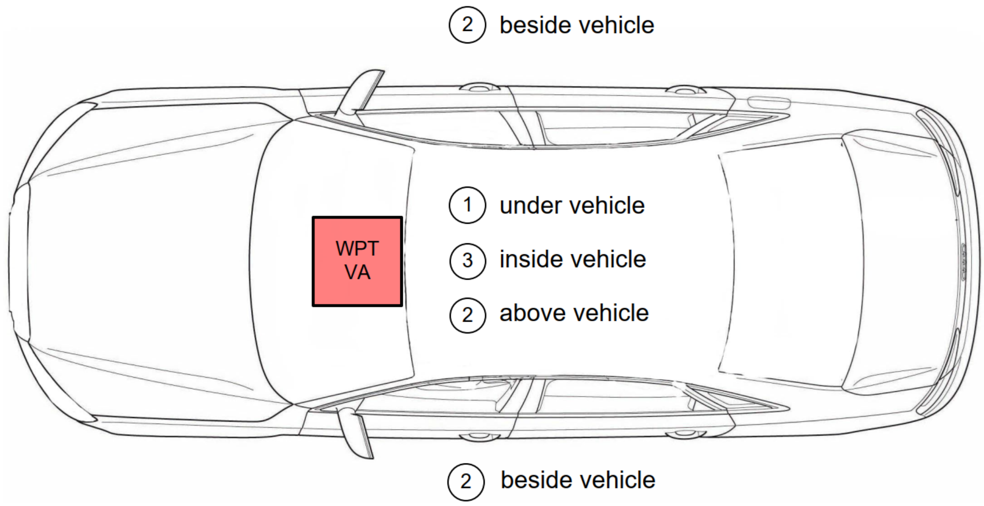


(a)

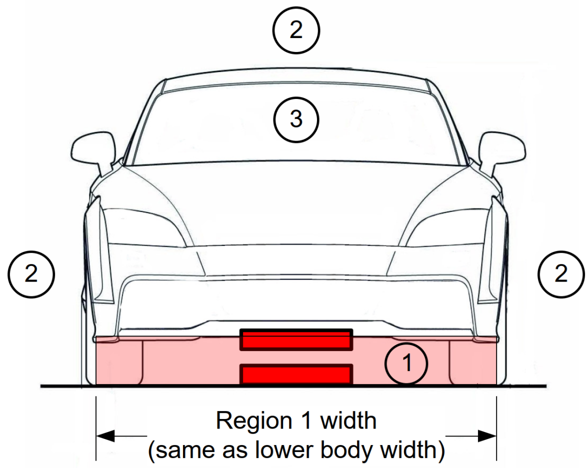


(b)

Figure 2.15: Regulatory EMF regions established by SAE J2954 standard: a) Top view; b) Front view [3].

Table 2.7: EMF exposure limits established in the SAE J2945 standard for frequencies between 79 kHz to 90 kHz [3].

| Region | Reference levels | Magnetic flux density $B$ ($\mu T$) |
|---|---|---|
| 1 | IEEE C95.1-2019 | Head and torso: 205<br>Limbs: 1130 |
| 2,3 | ICNIRP 2010 | 27 |

SAE J2954 standard also establishes regulatory limits for regions 2 and 3 in the case of people with CIEDs placed on their torso, in compliance with the ISO 14117 (Table 2.8) [43]. Additional limits for other IMDs are still being considered by the committee responsible for SAE J2954 [3].

The values in Tables 2.7 and 2.8 apply to sinusoidal modulated WPT fields. When non-sinusoidal, assessments should be conducted considering peak limits equal to the root mean square multiplied by $\sqrt{2}$.

Table 2.8: CIED EMF exposure limits established in the SAE J2945 standard for frequencies between 79 kHz to 90 kHz [3].

| Regions | Magnetic flux density $B$ ($\mu T$) |
|---|---|
| 2,3 | 15 |

IEC 61980-1 states, in section 11.8, that WPT systems and analogues should not expose humans to dangerous EMF above the limits established in international guidelines, usually ICNIRP and IEEE [44]. In addition, ISO 5474-4 states in section 10.4.3 that regions 2 and 3, which are equivalent to those referred to in SAE J2954, must not exceed the regulatory limits defined in the ICNIRP 2010 guidelines [45].

The standards observed apply to stationary systems, and the regulations for dynamic systems are lacking. There are some initiatives and standards to extend existing regulations for stationary systems to dynamic systems. One of these is the SAE J2954/3 standard, which establishes specifications for airworthiness criteria for light-duty EVs and heavy-duty EVs. However, in its current scope, the standard does not address electric two-wheelers, such as scooters or motorbikes, highlighting a gap in existing regulations for DWPT in the micromobility sector. This standard is still classified as WIP – Work In Progress, and there is no date set for its application. However, it will establish standards for interoperability, electromagnetic compatibility, EMF, minimum performance, safety, and testing for dynamic wireless power transfer. It will not yet address the possibility of bidirectional power transfer, which will be reserved for a future standard [4].

The IEEE/IEC 63184 standard establishes assessment methods of human exposure to EMF from stationary and dynamic WPT systems. It also presents the intention to regulate EMF exposure related to CPT systems operation in future editions [46].

To ensure the safety of EV drivers and pedestrians, DIPT systems must comply with international guidelines on human exposure to electromagnetic fields, such as those defined by ICNIRP. However, compliance with these limits can be challenging, particularly under misalignment conditions or at higher power levels. As a result, shielding strategies play a crucial role in reducing unintended EMF emissions and ensuring compliance with regulatory thresholds. Section 2.7 the design and implementation of magnetic shielding techniques designed to decrease stray fields in DWPT applications.

## 2.7 Shielding

Shielding strategies are designed to control EMF leakage. Limited EMF leakage affects adjacent equipment and interferes with human health, fauna, and flora. EMF leakage must be controlled by the IPT system in order not to exceed the maximum limits allowed by international standards such as SAE J2954 or IEC 61980 [3, 47]. Shielding is usually placed adjacent to the coils to help improve efficiency and coupling [8, 48]. Shielding types can be classified as active, passive and reactive, with the passive category being sub-classified as magnetic, conductive or magneto-conductive (Figure 2.16).

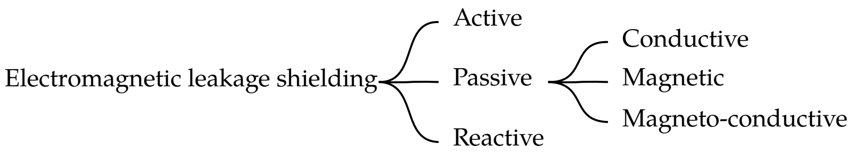


Figure 2.16: Classification of electromagnetic leakage shielding strategies [7].

Active shielding consists of adding extra windings to the coils in order to generate an inverse magnetic field to the power transfer magnetic field, thereby mitigating EMF leakage [49, 50]. Naturally, there is the design problem of placing the windings to reduce EMF leakage without interfering with the magnetic field and, consequently, the efficiency of the system. The extra energy consumed to power the shielding coils also contributes to a reduction in efficiency, along with an increase in the cost and size of the system [7, 8].

Conductive passive shielding uses the effect of magnetic induction on conductive materials, where eddy currents are created. The currents created in turn induce a magnetic field opposite to the field that generated them, counteracting it. EMF leakage is reduced, with efficiency losses of around 1% to 2% due to joule losses related to eddy currents [7]. There are examples of EVs that employ the chassis and body itself to reduce EMF leakage while still affecting the efficiency of the system [49, 51]. The SAE J2954 standard recommends an aluminium shield with dimensions of 800 mm $\times$ 800 mm $\times$ 0.7 mm [3].

Magnetic shielding uses materials that have high magnetic permeability and are non-conductive, helping to diffuse the electromagnetic flux to enhance power transmission. This solution has been shown to increase system efficiency while reducing EMF leakage. A practical example is the use of adjacent ferrite, which contributes to the above effects, but has the downside of increasing the cost of the IPT system. Some variations of ferrite application range from radial bars to rings around the coil [7, 8, 50, 52].

Most passive shielding applications use solutions that combine conductive and magnetic subtypes. As a rule, conductive shielding is used in conjunction with a ferrite body in order to improve efficiency while reducing EMF leakage [7].

Reactive shielding operates in a similar way to active shielding, by adding coil windings to reduce EMF leakage. However, the extra windings are not powered by the system, but are isolated from the primary and secondary coils and in a closed circuit with capacitors in parallel. The current flowing through the shielding coil originates from the magnetic field induced by the primary and secondary coils, resulting in a magnetic field that reverses the original one, thereby reducing EMF leakage. There are no controls over the reverse magnetic field, which is possible with active shielding [8, 36, 53].

Passive shielding is effective in reducing EMF leakage to levels below those mentioned in international standards for powers below 100 kW. For higher powers, active and reactive solutions are more efficient [7].

# 3 Surrogate techniques and sensitivity analysis

The design of complex electromagnetic systems requires significant computational resources, which increase the costs incurred during the design phase. As stochastic modelling considering uncertainty in physical phenomena is increasingly being applied to engineering projects, it requires dealing with large amounts of information that demands significant computational resources. Monte Carlo simulation is one of the most commonly used methods, allowing statistical quantities to be estimated by repeatedly sampling inputs and re-evaluating the model a large number of times. For studies requiring high fidelity, the number of re-evaluations can easily reach thousands or millions of runs, resulting in extremely high computational costs [54].

Surrogate modelling is an alternative that aims to generate a mathematical model that functionally approximates a high fidelity computational model. As each evaluation of a finite element solver is costly, a carefully validated model can reduce orders of magnitude of computational resources while retaining the input-output structure needed for prediction, optimisation, and sensitivity analysis. However, surrogates for design engineering should be substantially cheaper than the parent model and sufficiently accurate for decision-making purposes [55].

The model is created based on the response of the computational model to specific inputs and is trained to approximately predict the response of the computational system, reducing calculation time and computational costs. Surrogate models facilitate rapid and practical analysis, allowing the acquisition of a series of detailed analyses as well as sensitivity analysis and uncertainty quantification.

## 3.1 Surrogate techniques and notation

In the previous section, a qualitative overview of surrogates was introduced. In the present section, the discussion is formalised by introducing the mathematical notation that will be applied through this work.

Consider a random input vector with independent components $\mathbf{X} = (X_1, ..., X_M)^\top \in \mathbb{R}^M$, endowed with a joint probability density function (PDF) $f_{\mathbf{X}}(\mathbf{x})$. In this work, unless otherwise stated, the components $X_i$ are assumed to be mutually independent (Equation 3.1).

$$f_{\mathbf{X}}(\mathbf{x}) = \prod_{i=1}^{M} f_{X_i}(x_i) \tag{3.1}$$

A surrogate model is a computationally inexpensive approximation of the high-fidelity model $\mathcal{M}$, trained from a design of experiments,

$$\mathcal{D} = \{\mathbf{x}^{(i)}\}_{i=1}^{N} \subset \mathbb{R}^M, \quad \mathbf{y} = (y^{(1)}, ..., y^{(N)})^\top \tag{3.2}$$

where $y^{(i)} = \mathcal{M}\left(\mathbf{x}^{(i)}\right)$. The high-fidelity model response is defined as the random variable $Y = \mathcal{M}(\mathbf{X})$. Based on the training data $(\mathcal{D}, \mathbf{y})$, a surrogate mapping $\mathcal{M}^*$ is constructed such that $Y^* = \mathcal{M}^*(\mathbf{X}) \approx \mathcal{M}(\mathbf{X})$ [56, 57].

The following sections introduce the main surrogate families considered in this work: Gaussian process regression, artificial neural networks, support vector regression, radial basis function models, and polynomial chaos expansions.

## 3.2 Gaussian Process Regression

Gaussian process regression (GPR) modelling, or Kriging, is a stochastic modelling algorithm for computer experiments and uncertainty quantification. It was originally developed in geostatistics as a spatial interpolation technique and was later introduced into the context of deterministic computer codes [58, 59, 60]. In the state-of-the-art literature, GPR is regarded as a flexible, probabilistic interpolator that can emulate a broad class of smooth responses on the basis of relatively small experimental designs. The theoretical foundations on this surrogate are further explained.

### 3.2.1 Mathematical formulation

Let $\mathcal{M} : \mathbb{R}^M \to \mathbb{R}$ denote the high-fidelity deterministic model, as $Y = \mathcal{M}(\mathbf{X})$ where $\mathbf{X}$ is a random input vector distributed to the joint PDF $f_{\mathbf{X}}(\mathbf{x})$. The deterministic mapping $\mathbf{x} \mapsto \mathcal{M}(\mathbf{x})$ is a realisation of a Gaussian random field, as referred by Equation 3.3, where $m(\mathbf{x})$ is a deterministic trend function and $Z(\mathbf{x})$ is a zero-mean Gaussian process with covariance [61].

$$\mathcal{M}(\mathbf{x}) = m(\mathbf{x}) + Z(\mathbf{x}) \tag{3.3}$$

The covariance of $Z(\mathbf{x})$ can be defined as $\mathrm{Cov}(Z(\mathbf{x}), Z(\mathbf{x}')) = k(\mathbf{x}, \mathbf{x}', \boldsymbol{\theta})$, where $k$ is a positive-definite kernel, parametrised by hyperparameters $\theta$. The covariance structure is encoded by a kernel (or correlation function) $R = R(\mathbf{x}, \mathbf{x}', \boldsymbol{\theta})$ and a process variance $\sigma_Z^2$ (Equation 3.4).

$$k(\mathbf{x}, \mathbf{x}', \boldsymbol{\theta}) = \sigma_Z^2 \, R(\mathbf{x}, \mathbf{x}', \boldsymbol{\theta}) \tag{3.4}$$

The kernel is a crucial part of the GPR predictor as it directly influences the approximation of the model. There are several family types of kernels applicable to GPR as represented on Table 3.1. For the Matérn kernel, $\theta$ represents a correlation function scale parameter, $v$ is the shape parameter and $\Gamma$ is the Euler's Gamma function and $\mathcal{K}_v$ is the modified Bessel function of the second kind [56].

Table 3.1: Gaussian process regression kernels [56].

| Family type | Kernel |
|---|---|
| Linear | $R(\mathbf{x},\mathbf{x}',\boldsymbol{\theta}) = \max\left(0,\ 1-\dfrac{\lvert\mathbf{x}-\mathbf{x}'\rvert}{\theta}\right)$ |
| Exponential | $R(\mathbf{x},\mathbf{x}',\boldsymbol{\theta}) = \exp\left[-\dfrac{\mathbf{x}-\mathbf{x}'}{\theta}\right]$ |
| Squared exponential | $R(\mathbf{x},\mathbf{x}',\boldsymbol{\theta}) = \exp\left[-\dfrac{1}{2}\left(\dfrac{\mathbf{x}-\mathbf{x}'}{\theta}\right)^2\right]$ |
| Matérn | $R(\mathbf{x},\mathbf{x}',\boldsymbol{\theta}) = \dfrac{1}{2^{v-1}\Gamma(v)}\left(2\sqrt{v}\dfrac{\mathbf{x}-\mathbf{x}'}{\theta}\right)\mathcal{K}_v\left(2\sqrt{v}\dfrac{\mathbf{x}-\mathbf{x}'}{\theta}\right)$ |

The trend is usually written as a linear combination of $P$ functions, as stated by Equation 3.5, where $\mathbf{f}(\mathbf{x}) = (f_1(\mathbf{x}), ..., f_P(\mathbf{x}))^\top$ is a vector of functions that can be constant, linear or polynomials and $\beta$ is a vector of regression coefficients.

$$m(\mathbf{x}) = \beta^\top \mathbf{f}(\mathbf{x}) = \sum_{j=1}^{P} \beta_i f_j(\mathbf{x}) \tag{3.5}$$

Different alternatives of $\mathbf{f}$ correspond to simple, ordinary or universal (Table 3.2). In simple GPR the trend is assumed known, in ordinary GPR it is an unknown constant, and in universal GPR it is a general linear combination of basis functions [56, 62].

Table 3.2: Common Gaussian process regression trend specifications [62].

| Trend type | Basis functions |
|---|---|
| Simple | $\beta^\top \mathbf{f}(\mathbf{x}) = \sum_{j=1}^{P} f_{ij}(\mathbf{x})$ |
| Ordinary | $\beta^\top \mathbf{f}(\mathbf{x}) = \beta_0$ |
| Universal | $\beta^\top \mathbf{f}(\mathbf{x}) = \beta_i f_j(\mathbf{x})$ |

Considering a design of experiments $\mathcal{D} = \{\mathbf{x}^{(i)}\}_{i=1}^{N}$ and the corresponding model evaluations $\mathbf{y} = \left(y^{(1)}, ..., y^{(N)}\right)^\top$ with $y^{(i)} = \mathcal{M}\left(\mathbf{x}^{(i)}\right)$. The GPR surrogate $\mathcal{M}_{GPR}$ is the further mean of the Gaussian process conditioned on the observed data. The joint distribution of the vector of observations $\mathbf{Y} = \left(Y^{(1)}, ..., Y^{(N)}\right)$ and the prediction at a new point $Y^*(\mathbf{x})$ is multivariate normal (Equation 3.6).

$$\begin{bmatrix} Y^*(\mathbf{x}) \\ \mathbf{Y} \end{bmatrix} \sim \mathcal{N}_{N+1}\left(\begin{bmatrix} \mathbf{f}^\top(\mathbf{x})\,\boldsymbol{\beta} \\ \mathbf{F}\,\boldsymbol{\beta} \end{bmatrix}, \sigma_Z^2 \begin{bmatrix} 1 & \mathbf{r}^\top(\mathbf{x}) \\ \mathbf{r}(\mathbf{x}) & \mathbf{R} \end{bmatrix}\right). \tag{3.6}$$

In Equation 3.6, $\mathbf{F}$ is the $N \times P$ design matrix of the trend given as $F_{ij} = f_j\left(\mathbf{x}^{(i)}\right),\ \ i = 1,...,N,\ \ j = 1,...,P$ and $\mathbf{R}$ is the $N \times N$ correlation matrix with entries as $R_{ij} = R\left(\mathbf{x}^{(i)}, \mathbf{x}^{(j)}, \boldsymbol{\theta}\right)$ and $\mathbf{r}(\mathbf{x})$ is the vector of correlations between $\mathbf{x}$ and the instances given as $r_i(\mathbf{x}) = R\left(\mathbf{x}, \mathbf{x}^{(i)}, \boldsymbol{\theta}\right)$

By conditioning this joining Gaussian vector on the observed responses, the GPR surrogate is given by Equation 3.7, where $\widehat{\beta}$ is the generalised least-squares estimator written as $\widehat{\beta} = (\mathbf{F}^\top\mathbf{R}^{-1}\mathbf{F})^{-1}\mathbf{F}^\top\mathbf{R}^{-1}\mathbf{y}$ [56].

$$\mathcal{M}_{GPR} = \mathbf{f}^\top(\mathbf{x})\widehat{\beta} + \mathbf{r}^\top(\mathbf{x})R^{-1}\left(\mathbf{y} - \mathbf{F}\widehat{\beta}\right) \tag{3.7}$$

The predicted variance of the model is given by Equation 3.8, where $\mathbf{u}(\mathbf{x}) = \mathbf{F}^\top\mathbf{R}^{-1}\mathbf{r}(\mathbf{x}) - \mathbf{f}(\mathbf{x})$.

$$\sigma^2_{GPR}(\mathbf{x}) = \sigma^2\left[1 - \mathbf{r}^\top(\mathbf{x})\mathbf{R}^{-1}\mathbf{r}(\mathbf{x}) + \mathbf{u}^\top\left(\mathbf{F}^\top\mathbf{R}^{-1}\mathbf{F}\right)^{-1}\mathbf{u}(\mathbf{x})\right] \tag{3.8}$$

The main advantages and disadvantages of using this algorithm for this study are presented in the following subsections.

### 3.2.2 Advantages

For deterministic computer models, GPR surrogates achieve very high accuracy with relatively small experimental designs. As covariance encodes prior assumptions on smoothness and correlation of the response, the noise-free finite-model solutions allow the interpolation over the training data and reproduces all responses at the instances. These aspects are beneficial when the cost of simulations is high, especially for AC Magnetic simulations [61, 63].

This algorithm is data-efficient compared to other regression methods as it can represent non-linear but smooth response surfaces with relatively few hyperparameters. When combined with DoE's generated by Latin hypercube or low-discrepancy sequences, accurate surrogates can be obtained even in moderately high dimensions. This is in line with the present DIPT case study, where each Maxwell simulation may require substantial computational time [61].

The covariance kernel can be tailored to reflect prior knowledge of the underlying physics. An example is the anisotropy between subsets of design variables and correlation for geometrical parameters. Some kernels provide a mechanism for screening less influential inputs by learning a distinct characteristic length-scales. This mechanism may support qualitative sensibility analysis and dimension reduction before more formal methods based on variance can be applied [61].

### 3.2.3 Limitations

A fundamental drawback is that exact GPR inference scales in a cubic ratio in relation to the number of training samples, due to the need to factorise de covariance matrix, with memory costs scaling to the square of the number of training samples. This becomes a limitation beyond a few thousand instances [61].

The quality of a surrogate critically depends on an appropriate choice of a kernel family and hyperparameters. Some options can lead to over-smoothing or oscillations, while suboptimal parameters might negatively influence the interpolation property. Hyperparameters are commonly estimated by maximising the marginal likelihood, which involves non-convex optimisation problems that can have multiple local optimal solutions [55, 61].

The efficiency of the GPR surrogate decreases as the number of input variables increases or when the response surfaces exhibit sharp local features, discontinuities, or considerable variations in the scale. In such cases, large training sets and more sophisticated kernel constructions may be necessary, increasing the complexity of the model. For the case of extreme misalignment, these issues can limit the quality of a single global model [55].

Another important limitation, which is present on most surrogate techniques, is the low reliability extrapolation capacity. The predictions are most reliable within the convex hull of the training design. However, outside this region, the predictions revert to the previous mean with increasing uncertainty and may not respect physical constraints [60, 61].

### 3.2.4 Applicability to the present study

In the context of this study, GPR offers several attractive features as a candidate surrogate algorithm. First, the underlying finite-element model is deterministic am smooth with respect to the geometrical and positioning parameters in the considered design domain. This is precisely the regime where GPR surrogates excel. The further application enables accurate interpolation of quantities of interest, such as mutual inductance, coupling coefficient, and transmitter power, as functions of coil geometry over a relative position. Second, the probabilistic nature of GPR is advantageous for sensitivity analysis. Once trained, the surrogate can be sampled at negligible costs to perform large Monte Carlo studies that would be infeasible with the original Maxwell solver. Moreover, existing work on global sensitivity analysis with GPR surrogate demonstrates that variance-based Solbol's indices can be computed either from the representation itself or via Monte Carlo simulation of the surrogate [64, 65, 66].

Nevertheless, an important limitation of GPR in the present methodological framework is that, unlike polynomial chaos expansion (PCE), it does not provide by construction an explicit orthogonal decomposition of the model response in terms of input variables. In PCE, the polynomial basis is orthonormal with respect to the input measure, and the variance contributions associated with each polynomial subset can be calculated from the expansion coefficients, leading to simple closed-form expressions of Sobol sensitivity indices [67]. In contrast, for GPR, the Sobol indices must be obtained by integrating the predictive mean and covariance over the input space. This is because calculations involve additional Monte Carlo sampling or specialised analytic formulas. As one of the objectives of this work is to obtain a transparent, analytically tractable variance decomposition of the coupling coefficient and magnetic flux density distribution for a relatively high-dimensional input space, PCE offers a more direct route than GPR to compute Sobol's indices.[56].

## 3.3 Canonical low-rank approximations

Canonical low-rank approximations (LRA) constitute a class of surrogates that use tensor-product structures in order to mitigate the curse of dimensionality. The main objective is to approximate the response of a deterministic computational model by a sum of a small number of rank functions. Each rank function is written as a product of univariate functions in the individual input variables. In contrast to PCE, which work on an expanded multivariate polynomial basis, canonical LRA retain separated from the tensor product, leading to a number of unknown coefficients that increase linearly with the input dimension of the original model for fixed polynomial degrees and rank. This property makes LRA particularly attractive for high dimensional problems where the number of instances is relatively limited [68, 69].

### 3.3.1 Mathematical formulation

As in previous sections, a deterministic computational model $\mathcal{M}$ mapping an input random vector $\mathbf{X} = (X_1, ..., X_M)$ with a joint PDF $f_{\mathbf{x}}$ onto a scalar response $Y$ with independent components $X_i$ and associated marginals $f_{X_i}$ (Equation 3.9).

$$\mathbf{X} \in \mathcal{D}_{\mathbf{X}} \subset \mathbb{R}^M \mapsto Y = (\mathcal{M}) \in \mathbb{R} \tag{3.9}$$

A rank-one function of $\mathbf{X}$ is defined as the Equation 3.10, where each $v^{(i)}$ is a univariate function on the $i$-th input variable.

$$w(\mathbf{X}) = \prod_{i=1}^{M} v^{(i)}(X_i) \tag{3.10}$$

A canonical low-rank approximation of rank $R \in \mathbb{N}$ is then obtained by expression the model response as a finite sum of such rank-one components as expressed in Equation 3.11, where $a_r \in \mathbb{R}$ are scalar weighting factors and $v_r^{(i)}$ denotes the univariate function in the $i$-th dimension associated with the $r$-th rank-one term.

$$\mathcal{M}_{LRA}(\mathbf{X}) = \sum_{r=1}^{R} a_r \prod_{i=1}^{M} v_r^{(i)}(X_i) \tag{3.11}$$

For minor values of $R$, this representation yields a canonical low-rank approximation of the deterministic computer model [69].

The univariate functions $v_r^{(i)}$ are further expanded onto families of univariate polynomials $\{\varphi_k^{(i)}\}_{k\geq 0}$ that are orthonormal with respect to the corresponding marginal distributions $f_{X_i}$ as represented on Equation 3.12, where $p_i$ denotes the maximum polynomial degree used in dimension $i$ and $\gamma_{k,r}^{(i)}$ are scalar polynomial coefficients.

$$v_r^{(i)}(X_i) = \sum_{k=0}^{R} \gamma_{k,r}^{(i)} \varphi_k^{(i)}(X_i) \tag{3.12}$$

The resulting LRA surrogate can be described by the Equation 3.13 [68].

$$\mathcal{M}_{LRA}(\mathbf{X}) = \sum_{r=1}^{R} a_r \prod_{i=1}^{M} \left( \sum_{k=0}^{R} \gamma_{k,r}^{(i)} \varphi_k^{(i)} \right) \tag{3.13}$$

The univariate polynomials $\varphi_k^{(i)}$ are orthonormal with the corresponding marginal distributions of $X_i$ and should follow the condition in Equation 3.14, where $\delta_{jk}$ represents the Kronecker delta [68].

$$\int_{\mathcal{D}_{X_i}} \varphi_j^{(i)}(x_i) \varphi_k^{(i)}(x_i) f_{X_i}(x_i) dx_i = \delta_{jk} \tag{3.14}$$

The construction of a canonical LRA surrogate starts with an experimental design $\mathcal{D}\{\mathbf{x}^{(i)}\}_{i=1}^{N}$ sampled from $f_{\mathbf{x}}$ and the corresponding model evaluations $y^{(i)} = \mathcal{M}(\mathbf{x}^{(\mathbf{i})})$. The coefficients $a_r$ and $\gamma_{k,r}^{(i)}$ ara obtained by minimising a least-squares error criterion over the design, typically thought and alternating least squares (ALS) algorithm that updates the univariate factors dimension by dimension while holding the others fixed. Rank selection $R$ and maximal degrees $p_i$ are chosen using adaptive cross-validation or information criteria [68].

### 3.3.2 Relation to polynomial chaos expansions

As univariate polynomials are orthonormal with respect to the marginals of $\mathbf{X}$, both PCE and canonical LRA, can be classified as polynomial spectral approximations of a deterministic computer model. PCE represents a fully expanded multivariate orthonormal basis $\Psi_\alpha(\mathbf{X})$ indexed by multi-indices $\alpha$, whereas LRA uses the tensor-product structure in a sum of rank-on terms. At fixed maximum polynomial degrees $p_i$, the number of unknown coefficients in a PCE grows combinatorially with the dimension of the DoE, while for a canonical LRA it grows only linearly with the dimension of the DoE when the rank is moderate [68, 69].

Linear scaling has been repeatedly observed in numerical studies, where canonical LRA surrogates have proven particularly efficient when the input dimension is large and the available experimental design is small relative to the deterministic computer model [69, 70]. Reference [69] compares canonical LRA with PCE in analytical functions and finite-element models in structural mechanics and heat conduction. The study reports that for high-dimensional problems, with limited training data, LRA can achieve lower generalisation errors than PCE including better prediction of tail responses.

In addiction, the polynomial structure of LRA allows analytical post-processing of the surrogate to compute moments and, with post-processing, Sobol indices [71].

### 3.3.3 Advantages

Canonical LRA can significantly reduce the number of unknown coefficients compared to a full multivariate PCE of comparable degree by retaining a canonical tensor product structure and working with a sum of rank-one terms. Considering that the model response can be well approximated by a low canonical rank, the number of coefficients, and hence the size of the leat-square problems to be solved scales only linearly with the input dimension [68].

Canonical LRA can be constructed in a non-intrusive form from input–output pairs. Alternating least-squares schemes, possibly combined with regularisation and cross-validation, provide a practical method of estimating the coefficients dimension by dimension and updating the rank until pre-defined error criteria are met [69, 70].

As LRA relies on orthonormal polynomial bases in each dimension, the resulting surrogate admits analytic expressions for the mean and variance of the response, which can be computed directly from the coefficients without further Monte Carlo sampling. Moreover, recent work has shown that Sobol indices can be obtained at a low computational cost by post-processing the coefficients. This places canonical LRA on a similar base as PCE with respect to derivative-free global sensitivity analysis [67, 68, 70].

Canonical LRA and related low-rank methods have been applied to a range of high-dimensional uncertainty quantification problems, structural reliability, heat diffusion, supersonic aircraft design, and power-system probabilistic analyses. In many of these studies, LRA has been shown to match or outperform PCE and other surrogates, where the dimensionality is high and available training data are relatively scarce [69, 70, 72].

### 3.3.4 Limitations

The efficiency of canonical LRA is based on the assumption that the response of the model is well approximated by a low canonical rank. For high-order interactions between many inputs that exist and cannot be captured by a small number of rank-one terms, the required rank may become large, and the advantages over PCE surrogates. In extreme cases, the approximation problem may become a problem of alternating least squares (ALS) iterations that slowly converge or to suboptimal local minima [70].

Although LRA shares the same polynomial output as PCE, their implementation is more intricate. Polynomial degrees and truncation strategies must be selected, but also de ALS update schemes, stopping criteria, and rank selection rules. For this reason, the PCE surrogate is typically a substitute for the LRA surrogate [71].

### 3.3.5 Applicability to the present study

In the present work, the deterministic computational model is a three-dimensional finite-element representation of a DIPT system with moderate high-dimensional input space, comprising geometric parameters of the transmitter and receiver coils, as well as positional and mineralisation variables. The number of inputs is sufficiently large that PCE faces a non-trivial basis selection problem, yet the total number of simulations is constrained by computational cost. This is precisely the configuration for which LRA was designed. Linear scaling of the number of unknown coefficients with the input dimension offers a way to build accurate polynomial surrogates.

Moreover, the availability of analytic expressions for the mean and variance of the LRA surrogate, and the possibility of computing Sobol indices by post-processing its polynomial coefficients, align well with the overarching objective of this thesis, namely a rigorous global sensitivity analysis of the DIPT system under geometric and positional uncertainties

In this study, PCE will be adopted as the primary surrogate for global variance-based sensitivity analysis, due to their long track record in uncertainty quantification and their particularly simple closed-form expressions for Sobol indices [71]. In parallel, canonical LRA surrogates will also be constructed on the same experimental designs and used to compute LRA–based Sobol indices by post-processing their polynomial coefficients. Comparing the PCE and LRA–based sensitivity measures will provide additional consistency verification on the robustness of the global sensitivity conclusions and will highlight potential advantages and limitations of each surrogate for the present DIPT configuration.

## 3.4 Support vector machines for regression

Support vector machines (SVM) were originally developed within the framework of statistical learning theory and Vapnik-Chervonenkis theory as a method for classification and regression. They aim to control generalisation error by balancing empirical risk and model complexity thought structural risk minimisation. In the regression setting, the resulting method is commonly termed the support vector regression (SVR) [73].

Within engineering design, SVR has become a standard non-parametric surrogate for approximation expensive deterministic models $\mathcal{M} : \mathbb{R}^M \to \mathbb{R}$, particularly when the input–output mapping is non-linear and the available experimental design is of moderate size [74].

### 3.4.1 Mathematical formulation

Let $\mathbf{X}$ be the random input vector with independent and joint PDF $f_X(\mathbf{X})$, and let the scalar model response be$Y = \mathcal{M}(\mathbf{X})$. From a set of N evaluations of the DoE (Equation 3.15).

$$\mathcal{D} = \left\{ \left(\mathbf{x}^{(i)}, y^{(i)}\right) \right\}_{i=1}^{N}, y^{(i)} = \mathcal{M}\left(\mathbf{x}^{(i)}\right) \tag{3.15}$$

SVR determines the surrogate $\mathcal{M}_{\mathrm{SVR}}$ by solving an optimisation problem that minimises the norm of the regression function in feature space, subject to the requirement that prediction errors remain within a prescribed tolerance $\varepsilon$, apart from a set of penalised slack variables. In $\mathcal{H}$ the regression function is taken as affine, where $\mathbf{w} \in \mathcal{H}$ and $b \in \mathbb{R}$ are unknown parameters (Equation 3.16).

$$\mathcal{M}_{SVR}(\mathbf{x}) = \mathbf{w}^{\intercal}\varphi(\mathbf{x}) + b \tag{3.16}$$

Kernels commonly used in engineering applications include linear kernels, polynomial kernels, and Gaussian, exponential, and Matérn with parameters [74].

### 3.4.2 Advantages

SVR inherits several attractive properties from SVM theory that are directly relevant for surrogate techniques. First, the learning problem is convex, so the solution is unique and global for fixed hyperparameters. Second, the use of margin-based regularisation and a sparse set of support vectors tend to yield a reasonable generalisation even when the number of input measurements is comparable or larger than the sample size.

From a practical point of view, SVR is applicable to small to moderate sizes and strongly non-linear input-output relations, which are typical in computational mechanics and electromagnetics. Numerous studies have reported competitive accuracy of SVR surrogates compared to GPR and other surrogates for engineering design.

### 3.4.3 Limitations

Despite these advantages, several limitations are important in the present context. First, the predictive output of the classical SVR model is a point estimate, and no predictive variance or full predictive distribution is available directly. Probabilistic prediction intervals for SVR require additional modelling assumptions or post-processing techniques. Recent literature emphasises that this is an active research area rather than a standard feature of SVR [75]. Second, while the training problem is convex, its computational cost grows quadratically or cubically over time, which can be restrictive for very large DoEs. Third, the performance of SVR depends critically on the choice of the kernel family and hyperparameters. In practice, grid search and more sophisticated optimisation strategies are needed, and the result model can be sensitive to these choices, particularly in high-dimensional spaces [74].

Finally, in contrast to PCE or LRA surrogates, SVR generally does not provide an explicit orthogonal decomposition with respect to the input data. The regression function is expressed as a linear combination of kernel sections that do not form and orthogonal bases aligned with Sobol's decomposition of variance, except for special constructions. This lack of intrinsic variance decomposition means that global sensitivity indices cannot typically be extracted or calculated from the surrogate coefficients and has emerged as a new field of study [76].

### 3.4.4 Applicability to the present study

The present case study falls within the class of problems that can be analysed using SVR surrogates and has shown suitable performance for the analysis of electromagnetic systems. In particular, the reference [8] compared SVR, a multigene genetic programming algorithm (MGPA), and a space PCE for the analysis of static IPT systems under misalignment, air-gap variation, and receiver rotation. This study concluded that PCE provided a better trade-off between accuracy and computational cost for the IPT configuration considered. SVR was also found to be a valuable option, but polynomial-based surrogates (PCE, LRA) offer additional interpretability for sensitivity analysis.

For the DIPT systems considered in this work, SVR could therefore serve as an alternative surrogate to cross-check the predictions of the PCE surrogates. In particular, SVR may be beneficial in regimes where the response emphasises localised non-linear features. However, given the central objective of obtaining global sensitive analysis, SVR will not be further applied for this objective.

## 3.5 Polynomial chaos expansions

With the broad family of surrogate techniques introduced in the previous sections, polynomial chaos expansion (PCE) occupies a distinctive position as an uncertainty quantification method [77]. The primary objective of PCE is to construct a surrogate of the original deterministic computer model. In PCE, the model response is represented as a series expansion in terms of the ability to represent the model response with high–level of accuracy. The following subsection presents the basic principles of PCE, its mathematical formulation, and its application to the current study.

### 3.5.1 Mathematical formulation

In the PCE framework, the model response is expressed as an expansion in terms of orthonormal polynomials of the input random variables. Let $\mathbf{X} = (X_1, ..., X_M)^\intercal \in \mathbb{R}^M$ be a random vector with independent components, characterised by a joint PDE $f_\mathbf{X}(\mathbf{x})$ in a domain $\mathcal{D}_\mathbf{X} \subset \mathbb{R}^M$. Consider a deterministic computational model $Y = \mathcal{M}(\mathbf{X})$, $Y \in \mathbb{R}$ with finite variance (Equation 3.17 so that $Y$ belongs to the space of square-integrable random variables.

$$\int_{\mathcal{D}\mathbf{X}} M^2(\mathbf{x}), f\mathbf{X}(\mathbf{x}), \mathrm{d}\mathbf{x} < \infty, \tag{3.17}$$

Under these assumptions, PCE provides a spectral representation of $\mathcal{M}(\mathbf{X})$ on the basis of multivariate polynomials that are orthonormal to $f_\mathbf{X}$ [57].

The model response can be written as on Equation 3.18, where $\alpha = (\alpha_1, ..., \alpha_M)^\intercal \in \mathbb{N}^M$ is a multi-index that identifies the polynomial degree in each input variable, $\Psi_\alpha(\mathbf{X})$ is a multivariate polynomial that is orthonormal with respect to $f_\mathbf{X}$, and $c_\alpha \in \mathbb{R}$ are the corresponding expansion coefficients.

$$Y = \mathcal{M}(\mathbf{X}) = \sum_{\boldsymbol{\alpha} \in \mathbb{N}^M} c_\alpha \Psi_{\boldsymbol{\alpha}}(\mathbf{X}) \tag{3.18}$$

Multivariate polynomials are orthonormal due to the orthogonal relations represented on Equation 3.19, where $\delta_{\alpha\beta}$ is the Kronecker symbol extended to multi-indices.

$$\int_{\mathcal{D}\mathbf{X}} \Psi\boldsymbol{\alpha}(\mathbf{x}), \Psi_{\boldsymbol{\beta}}(\mathbf{x}), f_\mathbf{X}(\mathbf{x}), \mathrm{d}\mathbf{x} = \delta_{\boldsymbol{\alpha\beta}}, \tag{3.19}$$

For practical applications, the infinite sum in 3.18 must be truncated to a finite number of terms. Introduction a finite index set $\mathcal{A} \subset \mathbb{N}^M$ of selected multi-indices, the truncated PCE is as an approximation as represented on Equation 3.20 with $P = \mathrm{card}(\mathcal{A})$ being the number of retained polynomial basis functions [57].

$$\mathcal{M}(\mathbf{X}) \approx M^{PCE}(\mathbf{X}) = \sum_{\boldsymbol{\alpha} \in \mathcal{A}} c_{\boldsymbol{\alpha}} \Psi_{\boldsymbol{\alpha}}(\mathbf{X}) \tag{3.20}$$

### 3.5.2 Truncation schemes

Truncation schemes define which polynomial basis functions are retained in the expansion and therefore control the complexity and sparsity of the surrogate.

The index set $\mathcal{A}$ controls the effective complexity of the surrogate, because it specifies which multivariate polynomials $\Psi_\alpha$ are retained in the truncated expansion. It typicality starts from a total-degree set $\mathcal{M}_{M,p} = \{\alpha : |\alpha| \leq p\}$, and then applies additional truncation rules to avoid the combinatory growth of the basis with the number of inputs and the polynomial degree.

The maximum interaction truncation limits the number of variables that may appear simultaneously in any polynomial term, by enforcing $\|\alpha\|_0 \leq r$, where $\|\alpha\|$ counts the non-zero components of $\alpha$. This explicitly bounds the maximum interaction order represented in the surrogate, which is often consistent with prior expectations in engineering problems and substantially reduced the basis size at high dimensions [57].

The hyperbolic truncation uses a $q$–norm to define the admissible set $\mathcal{A}_{M,p,q} = \{\alpha \in \mathcal{A}_{M,p} : \|\alpha\|_q \leq p\}$ (Equation 3.21) [57].

$$\|a\|_q = \left( \sum_{i=1}^{M} a_i^q \right)^{1/q}, \quad 0 < q \leq 1 \tag{3.21}$$

For $q = 1$, this imposes a stronger penalty on configurations in which multiple components of $\alpha$ attain large values simultaneously, thereby preferentially promoting high-degree univariate effects over mixed interactions of comparable order [57].

### 3.5.3 Basis–adaptative

In numerous applications, it is unclear in advance which finite polynomial basis will yield a sufficiently accurate approximation of the computational model. The basis must be rich enough for the truncated expansion to account for the main features of the response. On the other hand, the number of terms that can be safely identified is limited by the size of the DoE, so that overly large bases tend to produce unstable regressions and over-fitting. Basis–adaptative PCE addresses this trade–off by selecting a suitable $\mathcal{A}$ from a family of candidate bases.

Basis adaptivity is implemented by constructing a sequence of nested candidate bases and comparing their performance using an estimate of the generalisation error. Starting from a small initial basis, defined by a low maximal degree $p_0$ and an initial value for the hyperbolic truncation parameter $q_0$, one computes the PCE coefficients and an *a posteriori* error estimate, such as the leave-one-out cross validation error. The basis is enriched by increasing the maximal degree $p$ or by relaxing the $q$–norm constraint, and the procedure is repeated until either a prescribed accuracy threshold is reached or a maximum number of iterations is exceeds. The final surrogate is chosen as the PCE with the smallest estimated generalisation error.

Figure 3.1 illustrates the hyperbolic truncation sets defined in equation 3.21 for different combinations of maximal degree $p$ and parameter $q$. Each column is the figure correlated to a fixed value of $p$, and each row to a fixed value of $q$. For $q = 1$, the hyperbolic truncation coincides with the standard total–degree scheme [57].

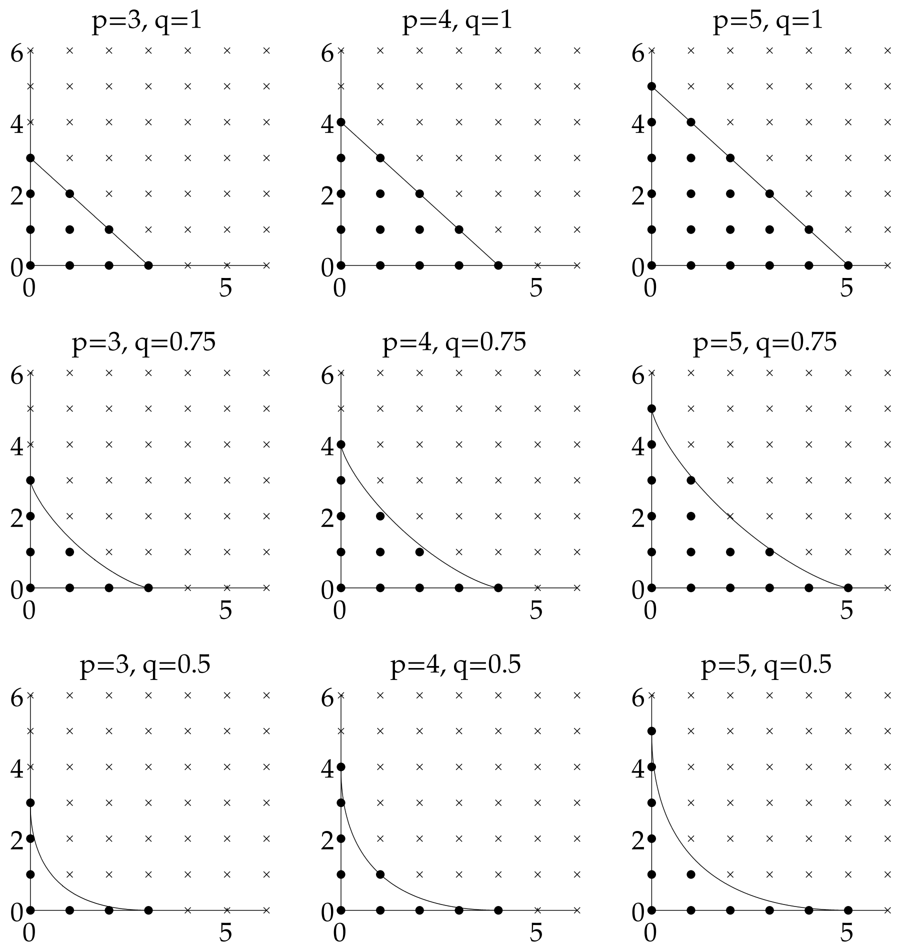


Figure 3.1: Hyperbolic truncation sets in two dimensions for different maximal degrees $p$ (columns) e and $q$ (rows) [57].

For $q < 1$ the truncation still progressively excludes the high-degree terms involving interacting variables [57].

The application of this algorithm uses post–processing error estimation, which is addressed in the following subsection.

### 3.5.4 Post–processing error estimation

Post–processing error estimation in PCE aims at quantifying, after the coefficients have been identified, how the surrogate reproduces the deterministic model. In the least-squares method, this is done by post–processing the residuals on the experimental design and, when, available, on an independent validation set.

The accuracy of the model and its predictive quality can be quantified by estimating the relative generalization error. $\epsilon_{gen}$ (Equation 3.22).

$$\epsilon_{gen} = \frac{\mathbb{E}\left[(\mathcal{M}(\mathbf{X}) - \mathcal{M}_{PCE}(\mathbf{X}))^2\right]}{\mathrm{Var}[Y]} \tag{3.22}$$

Essentially, the generalisation error allows us to perceive, on average, how significant the error is in relation to the input variation compared to the output variability.

The validation error can be obtained in cases where there is a validation sample and can approximate the generalisation error. Let $\{\mathbf{x}_{val}^{(i)}\}_{i=1}^{n_{val}}$ be the validation set, with the corresponding evaluations $y_{val}^{(i)} = \mathcal{M}(\mathbf{x})_{val}^{(i)}$ and the sample mean of the validation set response $\mu_{val} = \dfrac{1}{n_{val}} \sum_{i=1}^{n_{val}} y_{val}^{(i)}$. The relative validation error is given by Equation 3.23.

$$\epsilon_{val} = \frac{n_{val} - 1}{n_{val}} \frac{\sum_{i=1}^{n_{val}} \mathcal{M}(\mathbf{x}_{val}^{(i)}) - \mathcal{M}_{PCE}(\mathbf{x}_{val}^{(i)})}{\sum_{i=1}^{n_{val}} \left(\mathcal{M}(\mathbf{x}_{val}^{(i)}) - \hat{\mu}_{val}\right)^2} \tag{3.23}$$

If the study case involves an expensive computational model and there is no validation set, there are two ways to estimate the generalisation error: through the normalised empirical error and through the leave-one-out cross-validation error.

The normalised empirical error $\epsilon_{emp}$ is an estimator of the generalisation error (Equation 3.24). In this expression $\mu_Y$ represents the sample mean of the DoE response.

$$\epsilon_{emp} = \frac{\sum_{i=1}^{n_{val}} \mathcal{M}(\mathbf{x}^{(i)}) - \mathcal{M}_{PCE}(\mathbf{x}^{(i)})}{\sum_{i=1}^{n_{val}} \left(\mathcal{M}(\mathbf{x}^{(i)}) - \hat{\mu}_Y\right)^2} \tag{3.24}$$

However, because the normalised empirical error is evaluated on the same data used to fit the coefficients, it is known to be optimistically biassed: for ordinary least squares it decreases monotonically as the polynomial degree increases, irrespective of the size of the experimental design. This makes it unsuitable as a model-selection criterion in adaptive PCE algorithms, where over-fitting must be detected and avoided.

To address the over-fitting limitation of the normalised empirical error, the leave-one-out (LOO) cross-validation error emerges as an alternative based on the statistical learning theory.

Conceptually, the leave-one-out (LOO) error is defined as follows. For each index

$i = 1, \ldots, N$, the point $(\mathbf{x}^{(i)}, y^{(i)})$ is temporarily removed from the dataset, a PCE surrogate is reconstructed using only the remaining points, and the resulting surrogate is evaluated at $\mathbf{x}^{(i)}$ with the real value $y^{(i)}$. Let $\mathcal{M}_{\mathrm{PCE}\backslash i}$ denote this surrogate built without the $i$-th observation. The relative LOO error is then defined by the Equation 3.25, where $\hat{\mu}_Y = \frac{1}{N}\sum_{i=1}^{N}\mathcal{M}(\mathbf{x}^{(i)})$ is the sample mean of the model responses over the experimental design [57, 78].

$$\epsilon_{\mathrm{LOO}} = \frac{\sum_{i=1}^{N}\left(\mathcal{M}(\mathbf{x}^{(i)}) - \mathcal{M}_{\mathrm{PCE}\backslash i}(\mathbf{x}^{(i)})\right)^2}{\sum_{i=1}^{N}\left(\mathcal{M}(\mathbf{x}^{(i)}) - \hat{\mu}_Y\right)^2}, \tag{3.25}$$

Building $N$ separate PCE models is not necessary in the least-squares minimisation algorithm Let $A$ be the $N \times P$ regression matrix whose entries are $A_{ij} = \Psi_j\left(\mathbf{x}^{(i)}\right),\ i = 1, ..., N \wedge j = 0, ..., P-1$ and let $h_i$ be the $i$–th diagonal entry of $H$, where $H = A(A^{\intercal}A)^{-1}A^{\intercal}$. The LOO error can be expressed directly by the terms of the ordinary residuals as represented in the Equation 3.26.

$$\epsilon_{\mathrm{LOO}} = \frac{\sum_{i=1}^{N}\left(\frac{\mathcal{M}(\mathbf{x}^{(i)}) - \mathcal{M}_{\mathrm{PCE}\backslash i}(\mathbf{x}^{(i)})}{1-h_i}\right)^2}{\sum_{i=1}^{N}\left(\mathcal{M}(\mathbf{x}^{(i)}) - \hat{\mu}_Y\right)^2}, \tag{3.26}$$

Both empirical and LOO errors tend to underestimate the true generalisation error when the number of basis functions $P$ is not small compared to $N$. To compensate, a multiplicative correction factor $T(P, N)$, originally proposed in the reference [79] and adapted to PCE in the reference [78], must be applied. The corrected LOO error is written as represented in Equation 3.27.

$$\epsilon^*_{LOO} = \epsilon_{LOO}\, T(P, N) \tag{3.27}$$

The multiplicative correction factor is given by Equation 3.28 [79].

$$T(P, N) = \frac{N}{N-P}\left(1 + \frac{\mathrm{tr}\left[\left(\frac{1}{N}A^{\top}A\right)^{-1}\right]}{N}\right) \tag{3.28}$$

### 3.5.5 Computation of the coefficients

Once the polynomial basis $\Psi_\alpha(\mathbf{X}) : \alpha \in \mathcal{A}$ has been fixed, the remaining task is to estimate the coefficients $c_\alpha$ in the truncated expansion using only a finite set of evaluations of the original model. Two classic strategies are projection and least-squares regression, and both form the basis for the sparce least angle regression (LARS) approach used in this work.

In this work, the uncertain model inputs are collected in the random vector $\mathbf{X} = (X_1, \ldots, X_M)^\top$ with joint probability density $f_{\mathbf{X}}(\mathbf{x})$ supported on $\mathcal{D}_{\mathbf{X}} \subset \mathbb{R}^M$. The components $X_j$ are assumed mutually independent, so that

$$f_{\mathbf{X}}(\mathbf{x}) = \prod_{j=1}^{M} f_{X_j}(x_j), \qquad \mathbf{x} = (x_1, \ldots, x_M)^\top \in \mathcal{D}_{\mathbf{X}}. \tag{3.29}$$

The multivariate polynomial basis $\{\Psi_{\boldsymbol{\alpha}}(\mathbf{X})\}_{\boldsymbol{\alpha}\in\mathcal{A}}$ used in the PCE is constructed as a tensor product of univariate orthonormal polynomials that are each associated with the marginal distribution $f_{X_j}$ (e.g. Hermite polynomials for Gaussian variables, Legendre polynomials for uniform variables).

The projection method exploits the orthonormality of the polynomial basis with respect to the input. Each coefficient can in principle be obtained by projection as in Equation 3.30.

$$c_{\boldsymbol{\alpha}} = \mathbb{E}\big[\mathcal{M}(\mathbf{X})\, \Psi_{\boldsymbol{\alpha}}(\mathbf{X})\big]. \tag{3.30}$$

Writing the expectation as an integral leads to Equation 3.31, where $\{\mathbf{x}^{(i)}, w^{(i)}\}_{i=1}^{N}$ are the quadrature nodes and weights constructed to match the input distribution.

$$c_{\boldsymbol{\alpha}} = \int_{\mathcal{D}_{\mathbf{X}}} \mathcal{M}(\mathbf{x})\, \Psi_{\boldsymbol{\alpha}}(\mathbf{x})\, f_{\mathbf{X}}(\mathbf{x})\, \mathrm{d}\mathbf{x}, \approx \sum_{i=1}^{N} w^{(i)}\, \mathcal{M}(\mathbf{x}^{(i)})\, \boldsymbol{\Psi}_{\boldsymbol{\alpha}}(\mathbf{x}^{(i)}), \tag{3.31}$$

In PCE, the multivariate basis $\Psi_{\boldsymbol{\alpha}}(\mathbf{X})$ is built as tensor products of univariate orthonormal polynomials $\{\psi_k^{(j)}\}_{k\geq 0}$, each associated with the marginal distribution of $X_j$. In this work, all input variables are modelled with continuous uniform distributions over their respective design intervals, so the corresponding univariate basis is given by Legendre polynomials, as summarised in Table 3.3.

Table 3.3: Univariate orthonormal polynomial family and associated marginal probability distribution used in this work.

| Marginal distribution of $X_j$ | Support | Orthonormal polynomials $\{\psi_k^{(j)}(x)\}$ |
|---|---|---|
| $\mathcal{U}\big(x_j^{\min}, x_j^{\max}\big)$ | $x \in \big[x_j^{\min}, x_j^{\max}\big]$ | Legendre |

The Least-squares regression approach treats the coefficients as unknown parameters in a linear regression model. The truncated PCE can be written as Equation 3.32, where $\epsilon_{\mathcal{A}}$ denotes the truncation error.

$$Y = \mathcal{M}(\mathbf{X}) = \sum_{\alpha \in \mathcal{A}} c_\alpha \mathbf{\Psi}_\alpha(\mathbf{X}) + \epsilon_{\mathcal{A}} \tag{3.32}$$

As the multi-indices in $\mathcal{A}$ are $\{\alpha^{(1)}, .., \alpha^{(P)}\}$, with $P = \text{card}(\mathcal{A})$, the coefficient vector $\mathbf{c} = (c_{\alpha^{(1)}}, ..., c_{\alpha^{(P-1)}})$ the polynomial vector is $\mathbf{\Psi}(\mathbf{X}) = (\Psi_{\alpha^{(1)}}, ..., \Psi_{\alpha^{(P-1)}})$. Then $Y = \mathbf{c}^\intercal \mathbf{\Psi}(\mathbf{X}) + \epsilon_{\mathcal{A}}$. In the least-squared PCE, the minimisation problem is represented by the Equation 3.33 [57].

$$\hat{\mathbf{c}} = \arg\min \mathbb{E}\left[\hat{\mathbf{c}}^\intercal \mathbf{\Psi}(\mathbf{X}) - \mathcal{M}(\mathbf{X})\right] \tag{3.33}$$

In high-dimensional problems, the number of terms in a full PCE grows rapidly with the input dimension and the maximal polynomial degree. As a result, a classical (dense) expansion typically contains many basis functions whose contribution to the response variance is negligible, while still requiring additional model evaluations to identify their coefficients. In most applications, however, only low-order interactions between inputs are truly important. This empirical observation is often summarised as the sparsity-of-effects principle. Sparse PCE methods exploit this principle by constructing expansions in which only a subset of the candidate polynomials$\Psi_\alpha$ has non-zero coefficients, reducing both the number of model evaluations needed and the risk of over-fitting [57].

Within the PCE framework, sparsity is promoted at two levels. First, truncation schemes such as maximum interaction order and hyperbolic truncation already remove many mixed high-order terms from the candidate basis, leading to a thin multi-index set $\mathcal{A}$. Second, given this candidate basis, sparse regression methods are used to identify and retain only those polynomials that are supported by the data. The constrained optimisation problem adds a penalty term and takes the form of Equation 3.34, which is a modification of the least-squares minimisation problem (Equation 3.33) [57]. The regularisation term forces minimisation in favour of a small active set, imposing the sparsity of $\mathbf{c}$.

$$\widehat{\mathbf{c}} = \arg\min_{\mathbf{c}\in\mathbb{R}^{\mathcal{A}}} \left\{ \frac{1}{N} \sum_{i=1}^{N} \left( \mathbf{c}^\top \mathbf{\Psi}(\mathbf{x}^{(i)}) - \mathcal{M}(\mathbf{x}^{(i)}) \right)^2 + \lambda \|\mathbf{c}\|_1 \right\}. \tag{3.34}$$

The constrained minimisation problem can be solved with algorithms such as forward stage regression or least-angle regression LARS that is applied in the present study [57, 80, 81].

LARS is an efficient linear regression tool that works by moving the regressors from a candidate set to an active set, as it being the best one. The algorithm starts with coefficients equal to zero for a candidate set and an empty active set. The iterative process starts with finding the regressor most correlated with the residuals. Then, the coefficients of all polynomials currently in the active set are updated simultaneously, along a direction that keeps their correlations with the residual equal to each other, until some new candidate polynomial becomes equally correlated with the residual. The LOO error is calculated for the current iteration. All coefficients are updated, and the multivariate orthonormal polynomial is moved from the candidate set to the active set. The process is repeated until the size of the active set is $\min(P, N-1)$. Finally, the candidate set of regressors with the lowest LOO error is selected as the sparse basis [57].

### 3.5.6 Advantages

PCE provides a spectral representation of the model response in an orthonormal polynomial basis that is tailored to the input distributions. For a given surrogate, the statistical moments of the response follow directly from the expansion coefficients. Moreover, the orthonormality of the basis implies a correspondence between groups of coefficients and variance contributions associated with specific subsets of inputs. As a consequence, first–order and total Sobol′ indices can be computed analytically by simple post-processing of the PCE coefficients, without any additional data from the deterministic computational model [57].

From a computational standpoint, sparce PCE is a non-intrusive surrogate strategy that only requires deterministic evaluations of the original finite-element model on a suitable experimental design. In contrast to direct Monte Carlo or quasi–Monte Carlo sampling on the Maxwell model, which would be prohibitively expensive for the large number of parameter combinations explored in this study. The use of hyperbolic truncation and LARS further promotes sparsity by automatically selecting a small active set of polynomials that capture the dominant effects and low-order interactions.[57, 81] In the context of the DIPT model, this allows the smooth dependence of the coupling coefficients and magnetic flux density on the geometric design variables and misalignment parameters to be represented accurately with a relatively compact surrogate, which can then be reused for Sobol′ analysis.

### 3.5.7 Limitations

Despite these advantages, polynomial chaos expansions also present some inherent limitations. The number of candidate terms in a full expansion grows combinatorially with both the input dimension and the maximal polynomial degree [57, 78]. Even when sparse truncation and adaptive selection are employed, the quality of the surrogate critically depends on the ability of the sparse basis to capture the dominant interactions with a limited number of terms.

PCE is particularly effective for smooth responses with moderate non-linearity. When the model exhibits strong localised features, sharp gradients, or weak regularity, high polynomial degrees may be required, and the resulting expansions may become less stable and more expensive to evaluate. In the present application, the dimensionality of the geometric design space remains moderate, but the rapid growth of the candidate basis still motivates the use of hyperbolic truncation and sparse regression to keep the expansions tractable [57].

A further limitation is that any PCE surrogate reflects the assumed probabilistic model for the inputs. The construction of the orthonormal basis and the interpretation of the coefficients are based both on the choice of marginal distributions and the dependence structure [78].

### 3.5.8 Applicability to the present study

The characteristics of the present DIPT case study are aligned with the assumptions under which regression based sparse PCE is effective. The number of uncertain inputs, consisting of the geometric design variables and the misalignment parameters, remains moderate, and the Maxwell based model yields responses for the coupling coefficients and magnetic flux density that vary smoothly over the corresponding design domain. Under these conditions, a sparse polynomial basis can represent the dominant trends and low order interactions with relatively few active terms, so that accurate estimates of moments, Sobol' indices, and tail probabilities can be obtained at very limited additional cost once the coefficients have been identified [57, 81].

In conclusion, PCE is suitable for the subsequent analysis carried out in the present work. A single DoE of Maxwell simulations is used to construct separate surrogates for the key outputs, and these surrogates are then employed for global sensitivity analysis and as inexpensive models in the multi objective optimisation study.

## 3.6 Random forest regression

Random forest regression is a method that combines a large number of decision trees into a single predictive model. Each tree is built by repeatedly splitting the input space into smaller regions, using rules that aim to group together training observations with similar response values. To enable diversity among the trees, each one is grown on a resample of the original training data, and, at each split, only a random subset of the input variables is considered. For a new input, every tree assigns the point to one of its terminal regions and predicts the mean of the training responses within that region. The random forest prediction is obtained by averaging the outputs of all trees, which tends to reduce prediction variance while preserving the ability to represent complex, non linear relationships between inputs and outputs. This construction can be interpreted as a particular form of bootstrap aggregation, in which many over-fitted but low-bias trees are combined to produce a more stable regression function [82, 83].

The random selection of input variables in each split further decorrelates the trees, which improves the effectiveness of the averaging step. Random forests can be viewed as local-averaged data-adaptive estimators that approximate the regression function by aggregating information from training observations that fall in similar regions of the input space. This perspective explains why random forests are particularly effective in problems where interactions between inputs play an important role [82, 83].

### 3.6.1 Advantages

Random forest regression offers several properties that make it attractive for engineering applications. It does not require the specification of an explicit functional form for the input output relationship: the partitioning induced by the trees adapts automatically to the structure of the data, and can represent strong non-linearities and interactions without prior assumptions about their form. The use of many trees, each fitted to a perturbed version of the data, together with the averaging of their predictions, leads to a substantial reduction in variance compared to a single decision tree and typically provides good predictive accuracy with limited tuning settings [82].

### 3.6.2 Limitations

Despite these advantages, random forest regression has limitations that are relevant in the present context. The regression function produced by a forest results in a response surface that is not smooth. This lack of smoothness is a disadvantage when derivatives of the response with respect to the inputs are required, for example in gradient-based optimisation or in the construction of response surfaces with smooth contours. Furthermore, random forests do not extrapolate in a controlled manner outside the range of the training data. Predictions in regions with few or no nearby observations are essentially averages of distant points and may not reflect the true behaviour of the underlying physical model [83].

Another limitation is interpretability, as this method does not provide a compact analytic expression for the regression function. This stands in contrast to spectral methods such as PCE, for which the surrogate is given explicitly in terms of basis functions and coefficients. In addition, quantities such as moments, probability distributions, or variance-based sensitivity indices cannot be derived in closed form from a random forest and have to be estimated by Monte Carlo sampling on the surrogate, which introduces an additional source of numerical error. Finally, although random forests are relatively robust, their performance still depends on tuning parameters such as the number of trees, the minimal number of observations in a leaf, and the number of variables considered at each split, which must be chosen carefully to avoid under or over-fitting [82, 83].

### 3.6.3 Applicability to the present study

In the present study, random forest regression is used as a surrogate model to support the NSGA–II algorithm in the multi-objective optimisation of geometric design parameters. A forest is trained on a dataset of DoE Maxwell simulations, using as inputs the geometric variables and misalignment parameters, and as outputs the quantities that define the optimisation objectives and constraints, such as the coupling coefficients and the maximum magnitude of the magnetic flux density. Once trained, the forest provides fast and reasonably accurate predictions over the design domain spanned by the training data, which makes it suitable for repeated evaluations within an evolutionary optimisation loop.

For NSGA–II algorithm, the random forest serves as a surrogate that allows the evaluation of candidate geometries. This significantly reduces the computational cost of exploring large populations and many generations while preserving the main trends and interaction effects captured in the original simulations. The optimisation search is explicitly restricted to the region of the input space covered by the training designs, a selected optimal candidate design from Pareto fronts are subsequently re-evaluated with the Maxwell model to verify the surrogate predictions. In this way, the random forest acts as an efficient screening tool that enables practical multi-objective optimisation of the DIPT coupler geometry under geometrical restrictions.

## 3.7 Global sensitivity analysis

Global sensitivity analysis (GSA) enables quantification of the correlation between certain input parameters and output parameters in a deterministic computational model. The process begins by decomposing the variance of the model output as a function of the contributions of each individual input parameter [84].

Approaches to GSA can be classified into sample-based methods, linearisation methods, and global methods. Sample-based methods analyse correlations based on Monte Carlo samples. Linearisation methods are applicable to linear models or models that can be linearised around a given value. They are not applicable to non-linear models or those with high-order interactions. The Perturbation method and the Cotter method are referred to. Global methods are capable of evaluating linear and non-linear models by observing their variance and distribution. Morris' elementary effects, Borgonovo sensitivity indices, and Sobol' indices are cited, which will be applied in this study [71].

## 3.8 Sobol' indices

The variance of a deterministic computational model can be determined by the sum of the variances of the inputs to that model. Variance based global sensitivity analysis aims at quantifying how the uncertainty in each input variable, and in their possible interactions, contributes to the overall variance of a model output [71].

Let $Y = \mathcal{M}(\mathbf{X}) = \mathcal{M}(X_1, \dots, X_M)$ denote the response of the scalar model (either from the high fidelity model or from a surrogate), and $\mathbf{X} = (X_1, \dots, X_M)$ be a vector of $M$ mutually independent input random variables. Sobol' indices provide a decomposition of $\mathrm{Var}[Y]$ into additive contributions that are uniquely associated with individual variables and with their interactions of increasing order. For independent inputs, the model response can be expanded into a hierarchy of summands of increasing dimension, as represented in Equation 3.35, where $f_0 = \mathbb{E}[Y]$ is a constant equal to the mean model response.

$$f(\mathbf{x}) = f_0 + \sum_{i=1}^{M} f_i(x_i) + \sum_{1 \le i < j \le M} f_{ij}(x_i, x_j) + \cdots + f_{1,2,\dots,M}(x_1, \dots, x_M), \tag{3.35}$$

The total Sobol' indices can be expressed by Equation 3.36.

$$D = \mathrm{Var}[Y] = \int f^2(\mathbf{x})\, \mathrm{d}\mathbf{x} - f_0^2, \tag{3.36}$$

Equation 3.37 defines a function for partial variances [71, 85].

$$D_{i_1,\dots,i_s} = \int f^2_{i_1,\dots,i_s}(x_{i_1}, \dots, x_{i_s})\, \mathrm{d}x_{i_1} \dots \mathrm{d}x_{i_s}, \quad 1 \le i_1 < \cdots < i_s \le M. \tag{3.37}$$

### 3.8.1 First-order and total Sobol' indices

The first order and total Sobol' indices associated with each input variable are the most relevant quantities used in engineering applications. The first order Sobol' index of $X_i$ is defined by Equation 3.38.

$$S_i = \frac{D_i}{D} = \frac{\mathrm{Var}\big[\mathbb{E}(Y \mid X_i)\big]}{\mathrm{Var}[Y]}. \tag{3.38}$$

The total Sobol' index of $X_i$, denoted $S_{T_i}$, aggregates the main effect of $X_i$ and all interaction effects in which $X_i$ participates. It is defined as the sum of all Sobol' indices that involve $X_i$,

$$S_i^T = \sum_{\{i_1,\dots,i_s\} \ni i} S_{i_1,\dots,i_s}, \tag{3.39}$$

which is not convenient for computation because it would require evaluating every higher order index. Instead, an approximation can be made by computing the sensitivity measure for all variables except the one that is being evaluated $S_i^T = 1 - S_{\sim i}$

### 3.8.2 PCE-based computation of Sobol′ indices

Consider the first partition of the truncation set $\mathcal{A}$ according to the inputs in each polynomial term (Equation 3.40).

$$\mathcal{A}_i = \Big\{ \boldsymbol{\alpha} \in \mathcal{A} : \alpha_k \neq 0 \iff k \in v,\ k = 1, \ldots, M \Big\}, \tag{3.40}$$

that is, $\mathcal{A}_i$ contains all multi-indices for which the polynomial $\Psi_{\boldsymbol{\alpha}}(\mathbf{X})$ depends. The truncated PCE can then be reordered as represented on Equation 3.41.

$$\mathcal{M}(\mathbf{X}) = c_{\mathbf{0}} + \sum_{i \subset \{1,\ldots,M\},\, i \neq \emptyset} \ \sum_{\boldsymbol{\alpha} \in \mathcal{A}_i} c_{\boldsymbol{\alpha}}\, \Psi_{\boldsymbol{\alpha}}(\mathbf{X}). \tag{3.41}$$

The approximate first–order Sobol′ index of $X_i$ is given by Equation 3.42.

$$S_i^{\mathrm{PCE}} = \frac{\displaystyle\sum_{\boldsymbol{\alpha} \in \mathcal{A}_{\{i\}}} c_{\boldsymbol{\alpha}}^2}{\displaystyle\sum_{\boldsymbol{\alpha} \in \mathcal{A} \setminus \{\mathbf{0}\}} c_{\boldsymbol{\alpha}}^2}. \tag{3.42}$$

The approximate total Sobol′ index is represented by Equation

$$S_{T_i}^{\mathrm{PCE}} = \frac{\displaystyle\sum_{\boldsymbol{\alpha} \in \mathcal{A}_i^{\mathrm{tot}}} c_{\boldsymbol{\alpha}}^2}{\displaystyle\sum_{\boldsymbol{\alpha} \in \mathcal{A} \setminus \{\mathbf{0}\}} c_{\boldsymbol{\alpha}}^2}. \tag{3.43}$$

In conclusion, Sobol′ indices can be evaluated exactly from a PCE surrogate by post processing the expansion coefficients [67, 71].

### 3.8.3 LRA–based Sobol′ indices

In addition to polynomial chaos expansions, this work also employs canonical LRA surrogates to estimate Sobol′ indices. An LRA represents the model response as a finite sum of rank-one terms, each written as a product of univariate polynomial functions of the individual input variables. The coefficients of these univariate polynomials and the weights of each rank-one term are determined during the LRA identification stage, using the same DoE dataset that is used to build the PCE models.

Once a sufficiently accurate LRA surrogate has been trained, the Sobol′ indices can be obtained analytically by post-processing the LRA coefficients. The starting point is the standard definition of first-order and total Sobol' indices in terms of conditional expectations based on variance.

The first-order index of an input variable is written as the variance of the conditional mean of the model response, normalised by the total variance, whereas the total index is the unit minus the variance of the conditional mean with respect to all remaining variables.

The Sobol' indices obtained by LRA are used to corroborate the indices calculated by the PCE coefficients, contributing to their validation.

# 4 Finite Element Analysis

The study and optimisation of resonant DIPT systems is still a technical challenge, opting for methods that use FEA simulation or the analytical deduction of mathematical expressions that define the electromagnetic behaviour of the coupling. Computer simulations require the prior execution of a three-dimensional model, the configuration of materials, and other physical aspects. They require a considerable amount of simulation time and consume a vast amount of computing resources due to the analysis of many complex variables and mesh optimisation. Research efforts have focused on the surrogate modelling of resonant IPT systems [8, 86]. However, investigations specifically addressing the dynamic aspects of these systems remain absent from the current body of literature. Currently, research on the design of resonant DIPT systems specifically geared towards micromobility applications remains absent. This manuscript aims to address this research gap by contributing to the field of resonant DIPT systems focused on micromobility. The initial phase involved the construction of a detailed three-dimensional representation of the system specifically tailored for an e-motorcycle, followed by electromagnetic simulation [87].

Ansys Maxwell software was employed to perform electromagnetic simulations, given its reputation as a reference tool in the industry and applicability to the system in question. Presented as a tridimensional and bidimensional eddy current solver for electromagnetics, the software allows field parameters to be calculated as well as representation of the magnetic fields created. The solver employs adaptive meshing techniques that require the definition of the geometry, material properties, electric excitation, and required output data. Adaptive meshing is applied throughout the iterative solving process, reducing error and eliminating the need to define a mesh with complex geometry. The Ansys Maxwell magnetic transient solver enables the transient study of moving models, circuit coupling, and induced eddy currents based on the application of volumetric meshing and is applicable to resonant DIPT systems. Section 4.1 discusses the initial geometry of the model under study and its dimensions.

## 4.1 Model geometry

The model under study is dimensionally similar to the references [8, 88]. In the study [88], the coupling efficiency in the transition between primary coils was optimised by using a supplementary coil. However, results indicated that this supplementary coil generated peaks when passing over the transition section. Consequently, the initial setup in this study consisted of two primary coil assemblies that were rectangular in shape. Each coil had its length extended significantly to reach 2000 mm, as it is a more economical option and reduces the number of passages by transition per distance travelled.

The secondary coil was adapted to the size of the rear wheel of an e-motorcycle. A rectangular coil surrounding the rear wheel was chosen for compactness and to allow manoeuvrability without interfering with objects passing by the sides of the vehicle or accidental contact with the ground. Its design is based on the idea presented in the reference [89]. The design of the shield has been extended to promote the reduction of the magnetic field density in the upper area where the driver of the vehicle is located. Figure 4.1 illustrates the topology of the model to be optimised.

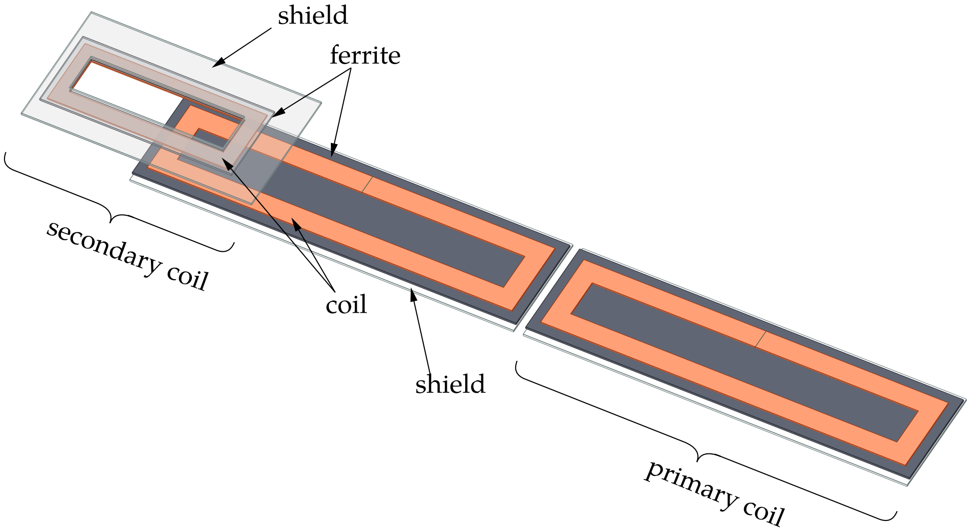


Figure 4.1: Topology of the proposed optimisation model consisting of a shielded coupling.

The geometry of the model was built directly in the Ansys Maxwell environment, using parametrised dimensions associated with optimisation variables. The model was implemented using named parameters for all relevant lengths and widths, allowing automatic manipulation and optimisation by parametric calculation. Table 4.1 summarises the variables to be optimised, their symbology, and their initial values. The selected parameters include the interior and exterior width and length dimensions of the coils, shielding, and ferrite layers, the distance between these elements, as well as the number of primary and secondary coil windings.

The parameters mentioned in Table 4.1 and illustrated in Figure 4.2 were selected as the most influential in terms of coupling, power transfer efficiency, and the robustness of the system to misalignments. The parameters were implemented as named variables in Maxwell, allowing a study of systematic variation in a parametric study that supports the construction of a dataset. This dataset will be a tool for capturing the impact of each variable in the face of different misalignment scenarios along the movement of the vehicle and its secondary coil along the primary coils on the roadway.

Table 4.1: Geometric variables to optimise, initial values and units.

| Primary coil parameters | Symbol | Nominal value | Unit |
|---|---|---|---|
| Coil interior width | $w_{i,1}$ | 200 | mm |
| Coil exterior width | $w_{e,1}$ | 400 | mm |
| Coil interior length | $l_{i,1}$ | 1700 | mm |
| Coil exterior length | $l_{e,1}$ | 1900 | mm |
| Ferrite exterior width | $w_{f,1}$ | 500 | mm |
| Ferrite thickness | $t_{f,1}$ | 5 | mm |
| Shield exterior width | $w_{s,1}$ | 550 | mm |
| Shield thickness | $t_{s,1}$ | 5 | mm |
| Spacing between shield and ferrite | $s_{sf,1}$ | 10 | mm |
| Spacing between coil and ferrite | $s_{cf,1}$ | 0 | mm |
| Number of windings | $N_1$ | 10 | — |
| Secondary coil parameters | Symbol | Nominal value | Unit |
| Coil interior width | $w_{i,2}$ | 200 | mm |
| Coil exterior width | $w_{e,2}$ | 350 | mm |
| Coil exterior length | $l_{i,2}$ | 950 | mm |
| Ferrite exterior width | $w_{f,2}$ | 400 | mm |
| Ferrite exterior length | $l_{f,2}$ | 1000 | mm |
| Ferrite thickness | $t_{f,2}$ | 5 | mm |
| Shield exterior width | $w_{s,2}$ | 650 | mm |
| Shield thickness | $t_{s,2}$ | 5 | mm |
| Spacing between shield and ferrite | $s_{sf,2}$ | 10 | mm |
| Spacing between coil and ferrite | $s_{cf,2}$ | 0 | mm |
| Number of windings | $N_2$ | 10 | — |

The geometry of the primary coil defines the distribution of the magnetic field along the respective segment of the road, which critically influences the efficiency under conditions of alignment and misalignment. Increasing the size of the primary coil improves tolerance to lateral misalignment, since the secondary coil remains within the main flux region for a greater distance. However, increasing the size of the primary coil reduces the flux density in the area where optimal alignment is achieved, contributing to a reduction in mutual inductance. It also increases the volume of copper required, which translates into an increase in coil resistance and losses. Therefore, the dimensions of the primary coil must balance the efficiency of the coupling, energy losses, and tolerance to misalignment.

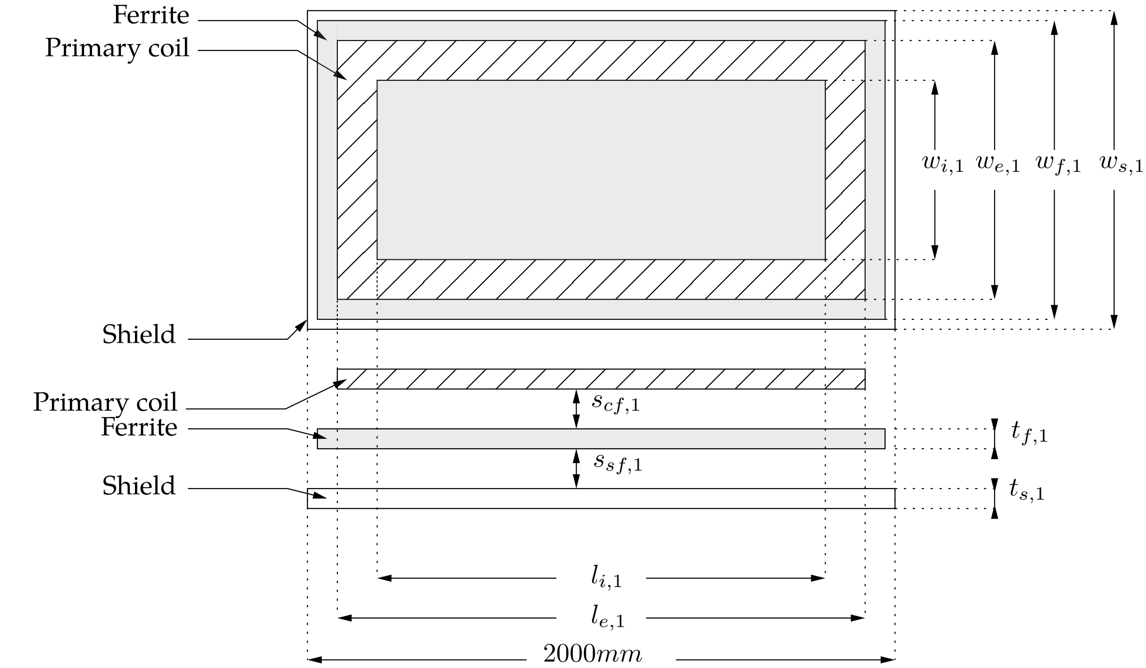


(a)

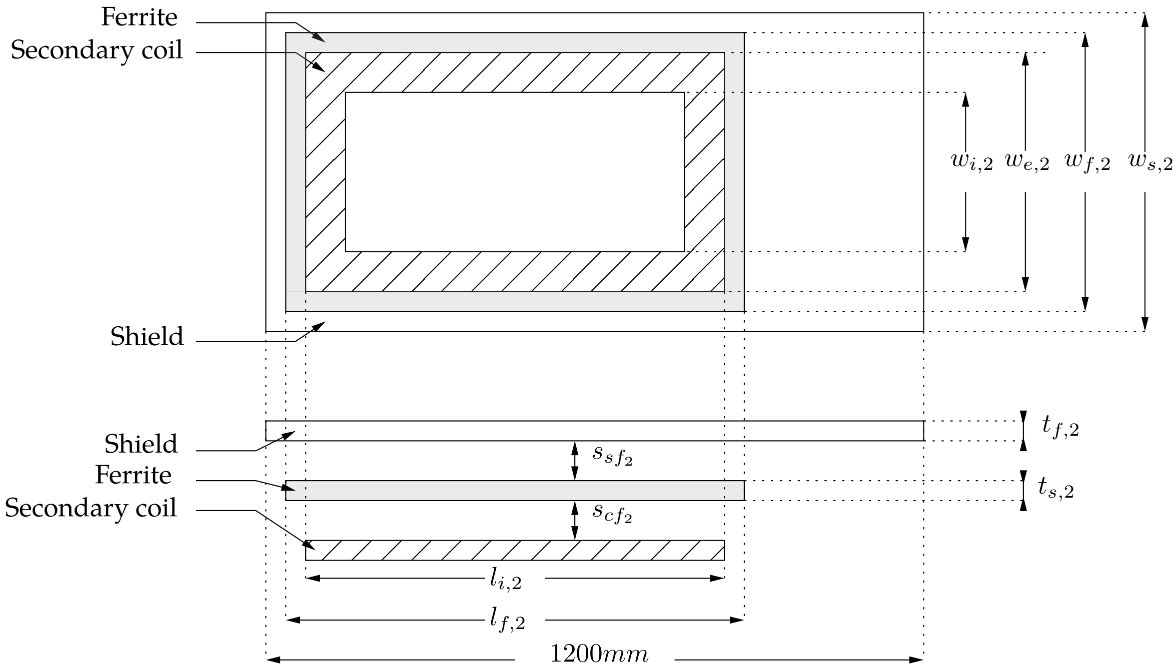


(b)

Figure 4.2: Schematic representation of the geometry dimensions. Top and side view of the: a) Primary coil; b) Secondary coil.

The geometry of the secondary coil, which is mounted on the vehicle, is constrained by space and weight limits. The dimensions of the inner and outer width of the secondary coil and the outer length were selected so that the geometry could be optimised according to the compromise between integration compactness and sufficient area to intercept the magnetic flux generated by the primary coil. A smaller secondary coil increases power density but is less tolerant of misalignment, while a wider coil is more robust to misalignment but increases weight, cost and reduces efficiency in perfect alignment.

Ferrite plates are used to provide a low-reluctance path for magnetic flux, guiding it through the coupling region and reducing leakage to the neighbourhood. The flux controller improves the mutual inductance between the primary and secondary coils, improving the efficiency of the transferred power, and reducing EMF leakage to meet ICNIRP standards. The length of the ferrite influences the primary and secondary coils in significantly different ways. The ferrite layer in the primary coil helps to confine the magnetic field in the roadway, ensuring that the flux generated interacts with the secondary coil instead of dispersing into the ground and surroundings. Although ferrite improves performance on misalignment, its extension well beyond the area of the coil increases the cost and complexity of the installation without a significant gain in efficiency. For road infrastructure, the increase in weight is not as relevant as it is for the secondary system, but the mechanical robustness of the driveway and the cost of materials and installation are. In the case of the secondary coil, the ferrite serves to guide the flux through the coil area, maximising the induced current and tolerance to lateral and angular misalignment. However, increasing the surface area of the ferrite increases the weight on the vehicle. Ferrite is brittle, so its application in vehicles requires special care in the design phase in favour of its durability. For both the primary and secondary systems, varying the size of the ferrite has little effect on the energy transfer efficiency. The SAE J2954 standard states that the ferrite should extend slightly beyond the perimeter of the coil and that the increase in benefit from the improvement in energy transfer efficiency cancels out with the increase. The aim of the study will also be to identify the optimum range of ferrite extension for each of the systems.

Conductive shielding is necessary to limit stray magnetic fields and contribute to the regulation of exposure regulations. The application of shielding on the roadway underneath the primary system is provided for in the SAE J2954 standard, helping to reduce EMF losses and exposure to pedestrians [3]. A shield with considerable dimensions helps to contain the magnetic field. However, increased shielding increases eddy current losses, which generate heat and degrade the system's efficiency. This effect is especially relevant at 85 kHz, where induced currents cause thermal issues. The total weight is not critical for the primary installation, but thermal dissipation and energy loss impose an upper limit.

Secondary shielding is designed to protect vehicle occupants and sensitive electronics from EMF leakage. It also prevents induced currents in the vehicle's metal parts. Increasing the secondary shield increases the weight of the vehicle and the size of its base, which is the upper limit. There will be a point at which increasing the shielding area will not improve EMF leakage over the region 3 referred to by SAE J2954 [3]. Shielding must be dimensioned to meet the limits established in the applicable standards while maintaining eddy current losses within acceptable limits.

The position along the longitudinal movement in the direction of EV circulation is given by the variable $x$, where this value comprises the total length of the two primary coils.

Misalignments are classified as lateral misalignments, where the position of the vehicle is offset from the axis of symmetry of the primary system, and angular misalignments, where the vehicle is inclined in relation to the plane orthogonal to the plane of the primary coils (Figure 4.3).

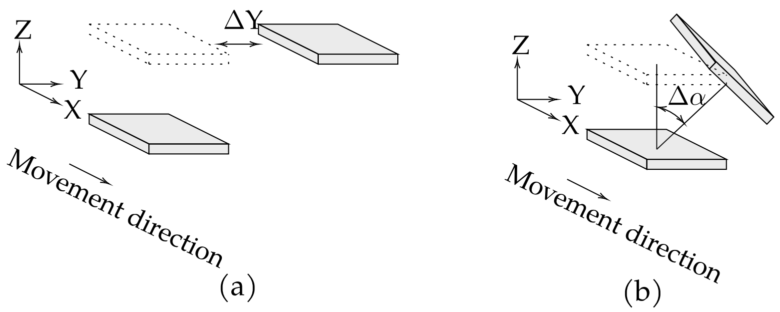


Figure 4.3: Classification of movement misalignment in e-motorcycles: a) Lateral (y axis); b) Rotation (x axis).

Table 4.2 represents the movement and misalignment control variables.

Table 4.2: Control variables.

| Control parameters | Symbol | Unit |
|---|---|---|
| Longitudinal movement | $x$ | mm |
| Lateral misalignment | $y$ | mm |
| Angular misalignment | $\alpha$ | degrees |

## 4.2 Model construction

The model was constructed directly in the Ansys Electronics Desktop Student interface. The global coordinate system was established as the reference for the primary side. For the secondary coil, the construction is based on the relative coordinate system, where the displacement and misalignments of the secondary side are applied, forcing all objects constructed in relation to this reference to follow the change in position (Figure 4.4).

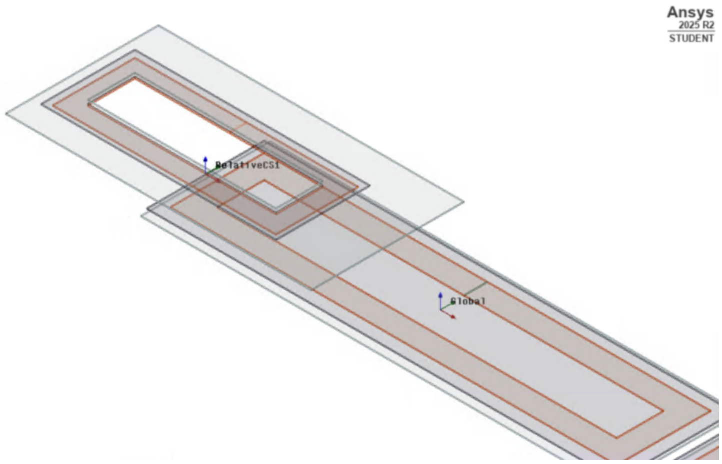


Figure 4.4: Global and relative coordinate systems used in finite-element modelling.

### 4.2.1 Primary

The primary winding of the DIPT coupler is represented in the finite element model as a single-layer rectangular conductor centred at the origin of the global Cartesian reference frame. The geometry is constructed as a rectangular coil obtained by subtracting an inner rectangular volume from a larger outer rectangular volume.

The corresponding position vectors, dimensions along each axis, and the coordinate system adopted for both volumes are summarised in Table 4.3.

Table 4.3: Geometric parametrisation of the primary coil (total volume and removed volume).

| | Volume | Removed volume |
|---|---|---|
| X position | 950 mm | $-\,l_{i,1}/2$ |
| Y position | $-\,w_{e,1}/2$ | $-\,w_{i,1}/2$ |
| Z position | 0 mm | 0 mm |
| X size | $l_{e,1}$ | $l_{i,1}$ |
| Y size | $w_{e,1}$ | $w_{i,1}$ |
| Z size | 5 mm | 5 mm |
| Coordinate system | Global | Global |

The exterior volume,represented in Table 4.3, defines the overall envelope of the winding with exterior length $l_{e,1}$ and interior width $w_{e,1}$ in the $x$ and $y$ directions, respectively. The removed volume, has interior length $l_{i,1}$ and interior width $w_{i,1}$ and is fully embedded in the outer block. The Boolean subtraction between these two volumes leaves a rectangular coil geometry that represents the copper track of the primary pad.

Both volumes are positioned in the global coordinate system so that their geometric centre coincides with the origin. In this way, the geometric parameters $l_{e,1}$, $l_{i,1}$, $w_{e,1}$ and $w_{i,1}$ directly control the overall footprint and window of the primary winding and can be directly related to the design variables of the optimisation study.

The thickness in the $z$-direction is fixed to 5mm, as the SAE J2954 refers to the use of litz conductors with an effective external diameter of approximately 5 mm for the charging pads [3].

The primary ferrite core is modelled as a single block of TDK PC95 material placed beneath the primary winding and centred with respect to the longitudinal axis of the coupler. Its geometry is defined in the global Cartesian reference frame, as summarised in Table 4.4. The block extends a fixed length of 2000 mm along the $x$–direction, while its width in the $y$–direction is controlled by the design variable $w_{f,1}$, corresponding to the exterior width of the primary ferrite slab, and its thickness in the $z$-direction is given by $t_{f,1}$, the ferrite thickness. The vertical position of the block is set so that its upper face lies a distance $s_{cf,1}$ below the lower surface of the primary winding, resulting in a $z$-coordinate of $-(s_{cf,1} + t_{f,1})$ for the origin of the prism. This parameterisation ensures that the ferrite core remains perfectly centred under the primary coil while allowing the core width, thickness, and coil–ferrite spacing to be varied systematically in the optimisation study.

Table 4.4: Geometric parametrisation of the primary ferrite.

| Parameter | Dimensions |
|---|---|
| X position | $-1000$ mm |
| Y position | $-w_{f,1}/2$ |
| Z position | $-(s_{cf,1} - t_{f,1})$ |
| X size | 2000 mm |
| Y size | $w_{f,1}$ |
| Z size | $t_{f,1}$ |
| Coordinate system | Global |

The primary shielding is modelled as a block located beneath the ferrite core of the ground assembly. Its geometry is defined directly in the global Cartesian reference frame, using the position vector and the edge lengths listed in Table 4.5.

Table 4.5: Geometric parametrisation of the primary shield.

| Parameter | Dimensions |
|---|---|
| X position | $-1000$ mm |
| Y position | $-w_{s,1}/2$ |
| Z position | $-(s_{cf,1} + s_{sf,1} + t_{f,1} + t_{s,1})$ |
| X size | 2000 mm |
| Y size | $w_{s,1}$ |
| Z size | $t_{s,1}$ |
| Coordinate system | Global |

The design variable $w_{s,1}$ controls the lateral extent of the shield, while the thickness $t_{s,1}$ determines the amount of conductive material available to attenuate the leakage field.

The vertical coordinate of the block origin encodes the stacking sequence coil, ferrite, and shield with spacings through the sum $s_{cf,1} + s_{sf,1} + t_{f,1} + t_{s,1}$, so that variations of spacing or layer thickness preserve the relative ordering of these components for all geometries in the design space. For the baseline configuration, the shield thickness is initialised at $t_{s,1} = 0.7$ mm, which is consistent with the thickness of 0.7 mm dimension reported in wireless charging pads of EVs designed under current IEC 61980–3 [47].

A sectioning was applied to the primary coil based on the YZ plane, of which only one section was retained. This section gives origin to the formulation of the current applied to the litz wire windings. This section is associated with an external excitation by the SS compensation power supply circuit referred to in section 4.4.

The second coil is obtained by reflection from a plane placed 5 mm from the far end of the original primary coil, orthogonally to the $x$ axis.

### 4.2.2 Secondary

The secondary coil is constructed, in analogy with the primary one, as the difference between two rectangular copper blocks attached to the relative coordinate system. The corresponding position vectors, edge lengths and coordinate system for the total volume and the removed interior volume are summarised in Table 4.6. By defining both blocks in the relative coordinate system, all longitudinal displacements, lateral misalignments, and angular misalignments are applied directly to this local coordinate system, so that the whole secondary assembly (coil, ferrite and shielding) moves while preserving the relative placement of its components. The removed volume defines the window that must accommodate the rear wheel and suspension envelope of the target electric motorcycle. Consequently, the internal dimensions of the secondary coil, as well as those of the underlying ferrite and shielding layers, are dictated by these packaging constraints and are therefore treated as fixed in the optimisation study, whereas only the outer dimensions and layer spacings are allowed to vary. The removed volume is also applied to the secondary shielding and ferrite, accounting also for spacings.

Table 4.6: Geometric parametrisation of the secondary coil (total volume and removed volume).

| Parameter | Volume | Removed volume |
|---|---|---|
| X position | $-l_{i,2}/2$ | $-400$ mm |
| Y position | $-w_{e,2}/2$ | $-w_{i,2}/2$ |
| Z position | 150 mm | 150 mm |
| X size | $l_{i,2}$ | 800 mm |
| Y size | $w_{e,2}$ | $w_{i,2}$ |
| Z size | 5 mm | $t_{f,2} + t_{s,2} + s_{cf,2} + s_{sf,2} + 5$ mm |
| Coordinate system | Relative | Relative |

A terminal was applied to connect to an external load power supply circuit with SS compensation (Section 4.4).

The secondary ferrite is modelled as a rectangular volume attached to relative coordinate system. Its geometric parametrisation is reported in Table 4.7, where $l_{f,2}$ and $w_{f,2}$ denote the longitudinal and lateral dimensions of the block and $t_{f,2}$ its thickness.

Table 4.7: Geometric parametrisation of the secondary ferrite.

| Parameters | Dimensions |
|---|---|
| X position | $-\,l_{f,2}/2$ |
| Y position | $-\,w_{f,2}/2$ |
| Z position | $+s_{cf,2} + 155$ mm |
| X size | $l_{f,2}$ |
| Y size | $w_{f,2}$ |
| Z size | $t_{f,2}$ |
| Coordinate system | Relative |

The removed volume within the ferrite uses exactly the same internal dimensions $l_{i,2}$ and $w_{i,2}$ as the window previously defined for the secondary coil, ensuring that the ferrite window coincides with the aperture required to accommodate the rear wheel of the e-motorcycle. As a consequence, the internal dimensions of the secondary coil, ferrite, and shielding are fully dictated by packaging constraints and remain fixed throughout the optimisation study, while only their exterior dimensions and spacings are allowed to vary.

The secondary shielding is represented by a rectangular block attached to the relative coordinate system. Its geometric parameterisation is reported in Table 4.8.

Table 4.8: Geometric parametrisation of the secondary shielding.

| Parameters | Dimensions |
|---|---|
| X position | $-525$ mm |
| Y position | $-\,w_{s,2}/2$ |
| Z position | $+s_{cf,2} + s_{sf,2} + t_{f,2} + 155$ mm |
| X size | 1300 mm |
| Y size | $w_{s,2}$ |
| Z size | $t_{s,2}$ |
| Coordinate system | Relative |

The block has a fixed longitudinal extent of 1300 mm and is positioned with its leading edge at $x = -525$ mm, so that it covers the region directly below the secondary pad while accommodating the packaging constraints of the rear section of the motorcycle. The lateral dimension of the shield is controlled by the design variable $w_{s,2}$, which determines how far the conductive plate extends beyond the lateral footprint of the secondary winding and ferrite. In the vertical direction, the origin of the shielding block is placed at a height $z + s_{cf,2} + s_{sf,2} + t_{f,2} + 5$ m, so that its position reflects the coil, spacing, ferrite, spacing, and shield of the stacking sequence and remains consistent for all misalignment conditions. Because the shield is defined in the same relative coordinate system as the secondary coil and ferrite, any longitudinal, lateral, or angular misalignment is applied uniformly to the whole secondary assembly, ensuring that their relative geometry is preserved while the vehicle pad moves with respect to the ground assembly.

### 4.2.3 Magnetic field leakage control planes

In this work, $\max |B|_{plane}$ denotes the maximum magnitude of the complex magnetic flux density on a control plane as represented on Equation 4.1, where $A_{plane}$ is the area of the control plane and $|B|$ is the magnitude of complex magnetic flux density obtained from the AC–Magnetic solution.

$$\max |B|_{top} = \max_{(x,y)\in A_{top}} |B(x, y, z_{top})| \tag{4.1}$$

$$\max |B|_{left} = \max_{(x,y)\in A_{left}} |B(x, y, z_{left})| \tag{4.2}$$

$$\max |B|_{right} = \max_{(x,y)\in A_{right}} |B(x, y, z_{right})| \tag{4.3}$$

Considering that an e-motorcycle handlebar is approximately 800 mm long, adding the 200 mm distance from the EVs to the measurement plane referred to in SAE J2954 and IEC 61980-3 and approximately 150 mm width from the origin of the $y$ axis, the lateral control planes were placed 1200 mm from the origin of this axis. The top control plane was placed 250 mm from the highest surface to accommodate the plastic casing and support structure of the e-motorcycle, added to the fixed height of the secondary coil of 150 mm. the control plane is placed 400 mm from the origin of the $z$ axis [3, 47]. The top control plane is subject to angular misalignment, following the secondary coil and, in turn, the EV occupant. Figure 4.5 represents the control planes over the finite–element model.

## 4.3 Materials and electromagnetic properties

In this section, the materials selected for simulation in Ansys Maxwell are presented. The selection of materials and their electromagnetic properties is essential for modelling the real behaviour and efficiency of the system. The properties were selected according to the IEC 61980-3 and SAE J2954 standards [3, 46].

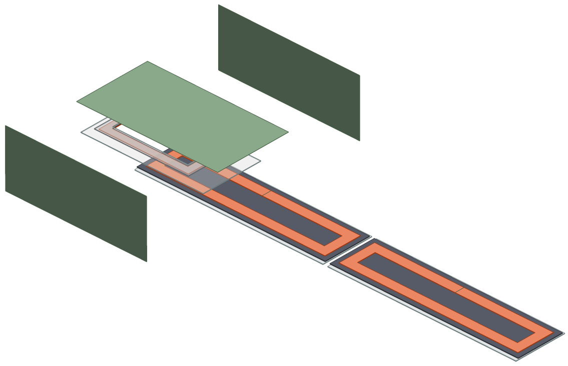

Figure 4.5: Control planes over the finite–element model.

### 4.3.1 Windings

Litz wire was used to model the coil windings, having an external diameter of 5 mm placed adjacently, in accordance with the guidelines of the SAE J2954 standard [3]. The use of this type of conductor is based on its capability to mitigate eddy current losses. The properties of the copper incorporated in the windings are represented in Table 4.9 .

Table 4.9: Electromagnetic properties assigned to the copper of litz wires in the ANSYS Maxwell simulations.

| Parameter | Symbol | Assigned value |
|---|---|---|
| Relative permittivity (–) | $\varepsilon_r$ | 1.000 |
| Relative permeability (–) | $\mu_r$ | 0.999 |
| Bulk conductivity (S/m) | $\sigma$ | $5.8 \times 10^7$ |

The SAE J2954 standard refers only to the outer diameter of the litz wire, without mentioning other construction aspects. For a specific operation frequency, it is possible to determine the number and diameter of strands and sub-bundles needed to mitigate the effects of the skin effect and proximity effect. The skin effect is the tendency of current in an AC circuit to flow along the outer edges of the conductor, resulting in increased electrical resistance. The proximity effect is the tendency of current to flow in undesirable patterns, such as loops or concentrated distributions, due to the presence of magnetic fields generated by nearby conductors.

The skin depth $\delta$ can be determined by Equation 4.4, where $\rho$ represents the resistivity of the copper conductor, $f$ represents the frequency of the sinusoidal current in the winding, and $\mu_0$ represents the permeability of free space.

$$\delta = \sqrt{\frac{\rho}{\pi f \mu_0}} \tag{4.4}$$

The litz wire is constructed in copper and is subjected to a test temperature of 20ºC, with a resistivity of $\rho = 1.72 \times 10^{-8}\Omega \cdot m$. The operating frequency $f$ is 85 kHz and the permeability of free space is $4\pi \times 10^{-7}H/m$. The skin depth for the case study is approximately 0.2264 mm. The diameter of a single wire should be, at most, approximately one third of the skin depth [90]. The maximum theoretical diameter for a single wire considering this orientation should be $0.075mm$. Consulting a catalogue from a manufacturer, for example Elektrisola, it emerges that the calculated value is close to the range of 0.102 – 0.079 mm for operating frequencies of 50 – 100 kHz respectively. Considering that the closest value by excess of commercial single wire diameters is 0.080 mm [90].

The litz wire must have an external diameter of 5 mm in accordance with SAE J2954, and a single wire diameter $d_{sw}$ of 0.080 mm. A taped cable with a 0.2 mm outer coating $t_{OC}$ of polyethylene naphthalate (PEN) was selected for thermal class 130–180 in accordance with standard EN IEC 60317-11 [91]. The packing factor $k_{PF}$ considered will be 1.30 [90].

$$OD_{LW} = k_{PF} \cdot \sqrt{n_{sw}} \cdot d_{sw} + t_{OC} \tag{4.5}$$

The number of single wires $n_{sw}$ for the case study will be 2130.18. This is rounded to 2000, as the number of single wires can vary by up to $\pm 25\%$ [92].

The length of the twist or length of lay shall not exceed 60 mm and shall have an 'S' twist (counter-clockwise), in accordance with standard EN IEC 60317-11 [91]. The length of lay is 20 mm, in accordance with the specifications of the manufacturer Elektrisola [93]. The twisted length factor (TLF) is considered in FEA simulation, referring to the ratio of the twisted-strand length to the bundle length. TLF is given by Equation 4.6, where $n_{sw}$ represents the total number of single wires in the litz wire, $d_{sw}$ the diameter of a single wire, $k_{PF}$ the packing factor and $p$ the length of lay.

$$TLF = \frac{\pi^2 n_{sw} d_{sw}^2}{4 k_{PF} p^2} \tag{4.6}$$

For the case study, given that the number of single wires is $n_{sw} = 2000$, $d_{sw} = 0.080mm$, the packing factor $k_{PF} = 1.3$ and the length of lay or pitch $p = 20mm$, the TLF will be approximately 1.061.

### 4.3.2 Ferrite

The ferrite cores integrated into the model are designed in strict accordance with the specifications defined in the SAE J2954 standard, which refers the use of TDK PC95 ferrite tiles. This directive is followed due to the as the IEC 61980 standard guidelines, as these standards do not offer comprehensive guidance or detailed specifications regarding this particular matter. The SAE J2954 standard defines, for WPT1 systems (power classification up to 3.7 kVA) and ground clearances Z1 (100 to 150 mm) or Z2 (140 to 210 mm), the use of PC95 (TDK) ferrite, as well as the tests performed [3]. Table 4.10 represents the relevant properties for simulating the system in Ansys Maxwell.

Table 4.10: Typical TDK PC95 ferrite properties [94].

| Parameter | Symbol | Assigned value |
|---|---|---|
| Relative permitivity (–) | $\varepsilon_r$ | 1.000 |
| Bulk condutivity (S/m) | $\sigma$ | 0.167 |

Considering that the relative permeability of TDK PC95 ferrite is non-linear, the relationship between magnetic flux density ($B$) and magnetic field strength ($H$) was obtained for various temperatures from the technical documentation in reference [95] (Figure 4.6).

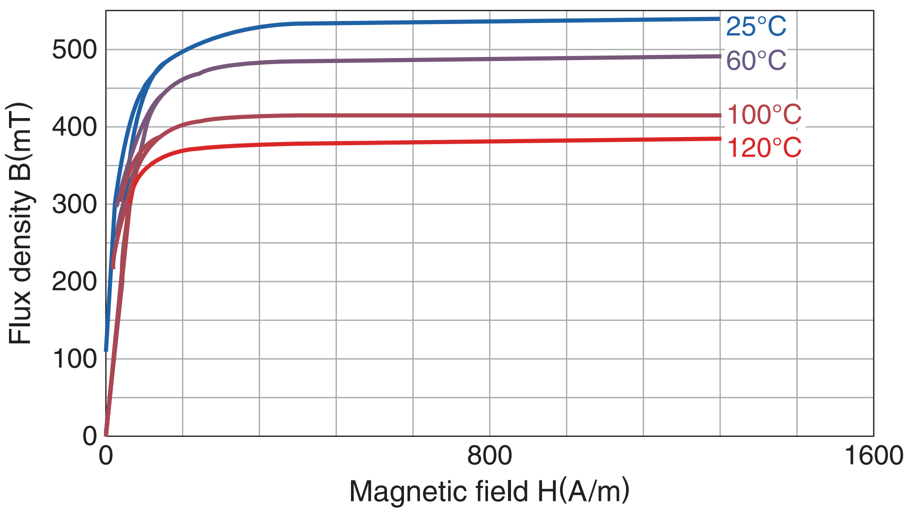


Figure 4.6: Temperature-dependent $B - H$ curves of TDK PC95 ferrite [95].

As the IEC 61980-1 and SAE J2954 standards state that practical tests should be conducted at a temperature of 20 ± 5 ºC [3, 44]. For this study, the B-H curve for 20ºC should be obtained from the curves for other temperatures.

In Ansys Maxwell, the characterization of a material's non-linear relative permeability can be effectively defined through the application of B-H curves corresponding to varying temperature conditions. These curves serve as a crucial tool in understanding how the magnetic properties of a material respond to changes in temperature. By analysing the B-H curves at different temperature points, one can derive a comprehensive understanding of the material's behaviour, thereby enabling precise modelling of its magnetic characteristics under a range of thermal environments. It is possible to specify multiple temperature-dependent B-H curves, which is particularly useful in temperature-dependent studies. In this case, given that the temperature will be constant at 20 °C, curves for various temperatures could be inserted, with Ansys Maxwell responsible for interpolating the B-H curve points at 20 °C necessary for the calculation. For this case, $m$ temperature-dependent curves are considered in the form given by Equation 4.7, where $T_0$, $T_k$ and $T_m$ are the known B-H curves.

$$\begin{gathered} T_0 : (0,0), (H_{01}, B_{01}), \cdots (H_{0i}, B_{0i}), \cdots (H_{0n}, B_{0n}) \\ \cdots \\ T_k : (0,0), (H_{k1}, B_{k1}), \cdots (H_{ki}, B_{ki}), \cdots (H_{kn}, B_{kn}) \\ \cdots \\ T_m : (0,0), (H_{m1}, B_{m1}), \cdots (H_{mi}, B_{mi}), \cdots (H_{mn}, B_{mn}) \end{gathered} \tag{4.7}$$

For a given temperature $T_i$, in this case 20ºC, and a given $H_i$, the magnetic flux density is obtained by Equation 4.8 based on the $B - H$ curves for temperatures $T_k$ and $T_{k+1}$ and the known magnetic flux densities $B_{ki}$ and $B_{k+1}$.

$$B_i = B_k + \frac{T_i - T_k}{T_{k+1} - T_k} (B_{k+1} - B_k) \tag{4.8}$$

Another approach would be the use of a thermal modifier that allows the properties of a material to be adjusted according to temperature. It consists of an equation that relates the property to temperature. However, as with the use of temperature-dependent $B - H$ curves, interpolation and calculation require more computational resources and, consequently, longer simulation times.

Considering that the simulation will not be temperature-dependent, but rather at a fixed temperature of 20ºC, it would reduce the computational resources needed to calculate the B-H curve for this temperature based on existing curves and insert it onto Ansys Maxwell. The $B - H$ curve could be calculated by a simple linear interpolation for 20ºC, according to Equation 4.8 or by the Jiles-Atherton physical model for magnetic hysteresis.

Numerical data was extracted in the form of points representing the $B-H$ curves at different temperatures using computer vision-assisted WebPlotDigitizer v5 software from the Figure 4.6 [96]. The software allows the identification of the coordinate axes and their calibration. Subsequently, the curves were identified and numerical datasets were created using colour identification by computer vision and manual adjustment. The curve data were extracted into comma-separated values (CSV) files for each temperature. To perform calculations and comparisons between the simple linear interpolation and the Jiles-Atherton hysteresis model, it was necessary to develop a comprehensive dataset of magnetization curves that is not only clean and consistent but also indexed according to temperature.

Raw data were provided from several temperatures. The files containing mixed decimal commands and semicolon delimiters were replaced with decimal points and standardised delimiters to commands, ensuring reliable numerical processing by pandas and other Python numerical libraries. This essential normalisation step guaranteed consistent floating-point representation across all temperature series.

For some temperatures (25, 60, and 100 °C), the datasets did not include the origin (0,0). To reinforce the physical behaviour for $B(H = 0) = 0$, which is the beginning of the magnetisation curve, a smooth, monotonic seed was created connecting the leftmost end of the curve with the origin $(H_1, B_1)$. The logarithmic form of the approximation is $B(H) = k \ln (zH + 1)$, calibrated by $z = 1/H_1$ and $k = B_1/\ln (zH_1 + 1)$, so that the segment passes through the origin and the leftmost end of the curve. The datasets for these temperatures were recorded ensuring continuity and a realistic approach to the origin. Although heuristic, this operation prevents the appearance of artefacts in spline interpolation routines. Furthermore, the final 20 °C dataset to be imported into Ansys Maxwell must contain a source, an initial positive slope, be single-valued, and have no repeated pairs [97].

All temperature curves were merged via an external join over the series of magnetic fields, producing a dataset ordered by $H$. To enable pointwise temperature interpolation and consistent numerical operations, each temperature series was resampled onto a shared uniform magnetic field grid, using SciPy linear interpolation. The original dataset was mapped to $H \in [0, 1250]$ with steps of 10 A/m. The choice of resampling with a uniform grid and a modest step size of 10 A/m resembles a balance between preserving details of features near the knee and keeping the table concise for downstream solvers and scripts. A constant grid is crucial for constructing and interpolating temperature at fixed $H$ and for calibrating a physical parametric hysteresis model with constant discretisation.

After generation a cleaned and origin-anchored dataset, a baseline single-valued 20ºC curve is calculated using linear interpolation from the 20ºC and 60ºC temperature series, as they are the nearest ones. The interpolation operation is given by the Equation 4.8.

In the Jiles-Atherton model, the volumetric magnetization $M$ is decomposed into irreversible and reversible components (Equation 4.9)

$$M = M_{irr} + M_{rev} \tag{4.9}$$

and the irreversible magnetization is obtained by solving a first order equation driven by the anhysteretic magnetization $M_{an}$ for a quasi-static case. The irreversible component is given by Equation 4.10.

$$M_{irr} - M_{an} + k\delta \frac{dM_{irr}}{dH_{eff}} = 0 \tag{4.10}$$

Where $k$ is a coefficient linked to hysteresis loss and $\delta = sign(H_{eff})$ which describes the branch direction of the effective field $H_{eff}$. $M_{an}$ is the anhysteretic curve that follows the Langevin function (Equation 4.11).

$$M_{an}(H_{eff}) = M_S \left[ \coth\left(\frac{H_{eff}}{a}\right) - \frac{a}{H_{eff}} \right] \tag{4.11}$$

Where $M_s$ represents the saturation magnetization, and $a$ is the shape parameter that controls the *Langevin* curvature of $M_{an}$. The effective field $H_{eff}$ is given by the Equation 4.12.

$$H_{eff} = H + \alpha M \tag{4.12}$$

The differential susceptibility is given by Equation 4.13, where $\delta_M$ is the logical function that suppresses non-physical solutions and $c$ is the reversibility coefficient.

$$\frac{dM}{dH_{eff}} = \frac{\delta_M}{k\delta}(M_{an} - M) + c\frac{dM_{an}}{dH_{eff}} \tag{4.13}$$

The five J–A parameters $M_s, a, k, c, \alpha$ produce a hysteresis loop whose flux density $B$ follows Equation 4.14, where $\mu_0 = 4\pi \times 10^{-7} H/m$ [98].

$$B(H) = \mu_0 \left(H + M_{an}(H_{eff})\right) \tag{4.14}$$

Equations 4.11, 4.12 and 4.14 represent the anhysteretic branch (Langevin). If $k$ and $c$ are omitted, the resulting $B(H)$ is a single-valued function, which can be imported into Ansys Maxwell and directly compared to a linear temperature-interpolated curve at 20ºC. Analogous to reference [98], the parameters were identified by non-linear least-squares. Only the parameters $M_s$, $a$ and $\alpha$ were calculated, deferring $k$ and $c$ as coefficients related to reversibility and hysteresis loss.

Following these governing equations, the anhysteretic backbone was identified at each temperature $T \in \{25, 60, 100, 120\}$ ºC by non-linear least squares on the $B(H, T)$ data. The effective field was enforced implicitly at every sampling point through $H_{eff} = H + \alpha(T)M_{an}(H_{eff})$, and the pointwise residual was minimised at each sample (Equation 4.15).

$$r(T) = B_{dataset}(H, T) - \mu_0 \left(H + M_{an}(H_{eff})\right) \tag{4.15}$$

The anhysteretic branch was evaluated as represented on Equation 4.16.

$$M_{an}(H_{eff}) = M_S(T)\left[\coth\left(\frac{H_{eff}}{a(T)}\right) - \frac{a(T)}{H_{eff}}\right] \tag{4.16}$$

Prior to fitting, each $B(H)$ trace was lightly smoothed by a shape-preserving Piecewise Cubic Hermite Interpolating Polynomial (PCHIP) interpolator as a way of suppressing the computer-vision assisted software roughness without introducing overshoot. The parameters were identified with the use of the SciPy function for solving non-linear least-squares optimization, with soft-$L_1$ loss, physically plausible bounds on the parameters and increased weight in the knee region (50–300 A/m). Small convergence tolerances were considered so that iterations terminated only when further reductions in the objective were negligible.

A consolidated summary of the identified anhysteretic J–A parameters is reported in Table 4.11. For each dataset temperature $T \in \{25, 60, 100, 120\}$ °C, the triplets $M_s$, $a$ and $\alpha$ were obtained by a robust non-linear least squared against the corresponding temperature-specific $B(H,T)$ datasets as well as residual statistics.

A compact set of complementary residual statistics was adopted to characterize agreement and misfit. Mean Absolute Error (MAE) given in Tesla, reports the typical absolute deviation and is robust to isolated outliers owing to its linear penalty. Root Mean Square Error (RMSE) given in Tesla, emphasises peaks in the error throughout quadratic penalisation ans and therefore sensitive to local mismatches around the knee. Finally, $R^2$ summarises the overall concordance between curves independent of absolute units. Reporting MAE alongside $R^2$ thus balances a physical interpretability and sensitivity to local discrepancies.

Table 4.11: Jiles–Atherton (anhysteretic) parameters and error metrics per temperature.

| Temp. (°C) | $M_s$ (A/m) | $a$ (A/m) | $\alpha$ (–) | MAE (T) | RMSE (T) | $R^2$ |
|---|---|---|---|---|---|---|
| 25 | $4.378 \times 10^5$ | $1.591 \times 10^1$ | $2.3527 \times 10^{-5}$ | 0.004462 | 0.010803 | 0.972171 |
| 60 | $3.979 \times 10^5$ | $1.336 \times 10^1$ | $3.1525 \times 10^{-19}$ | 0.004622 | 0.007931 | 0.982976 |
| 100 | $3.390 \times 10^5$ | $1.114 \times 10^1$ | $2.7774 \times 10^{-23}$ | 0.007308 | 0.014482 | 0.942612 |
| 120 | $3.090 \times 10^5$ | $9.056 \times 10^0$ | $4.7321 \times 10^{-23}$ | 0.003969 | 0.010444 | 0.957927 |

As the temperature increases, the magnetisation decreases monotonically from $4.378 \times 10^5$ to $3.090 \times 10^5$ A/m, while the shape parameter reduces from $1.591 \times 10^1$ to $9.056 \times 10^0$, indicating a gradual softening of the knee. The mean-field coupling $\alpha$ collapses to numerically negligible values, implying that the Weiss-type feedback is not required to reproduce the anhysteretic backbone at this temperatures. The fits are accurate across the range, with $RMSE$ between $7.9$ and $14.5mT$ and $R^2$ between $0.943$and $0.983$.

Focusing on the operational condition of 20 °C, the projected parameters $M_s = 4.435 \times 10^5$ A/m, $a = 1.628 \times 10^1$ A/m and $\alpha = 2.689 \times 10^{-5}$. Substituting this triplet into the implicit anhysteretic law produces a single-valued, solver-ready $B(H)$ dataset. Pairwise comparisons statistic against the linear 20ºC projection on the common filed grid $H$ indicate high concordance with the linear interpolation method dataset as $MAE = 4.49mT$, $RMSE = 11.25mT$ and $R^2 = 0.9704$. The residual structure is concentrated around the knee region and the high-field asymptote, which consistent with the backbone representation that omits the explicit loop opening ($k$ and $c$). Consequently, the 20 °C J–A based dataset is appropriate as a single-valued constitutive relation for AC Magnetic analysis in Ansys Maxwell.

Figures 4.7 and 4.8 characterise the agreement between the 20 °C curves. In Figure 4.7 the linear projection is nearly coincident over the full range, with small systematic differences around the knee where J–A model exhibits slightly smoother transition to saturation.

The scatter plot in Figure 4.8 recasts the same relation in pairwise form. Points lie tightly close around the equality line, with the largest deviations confined to intermediate flux densities.

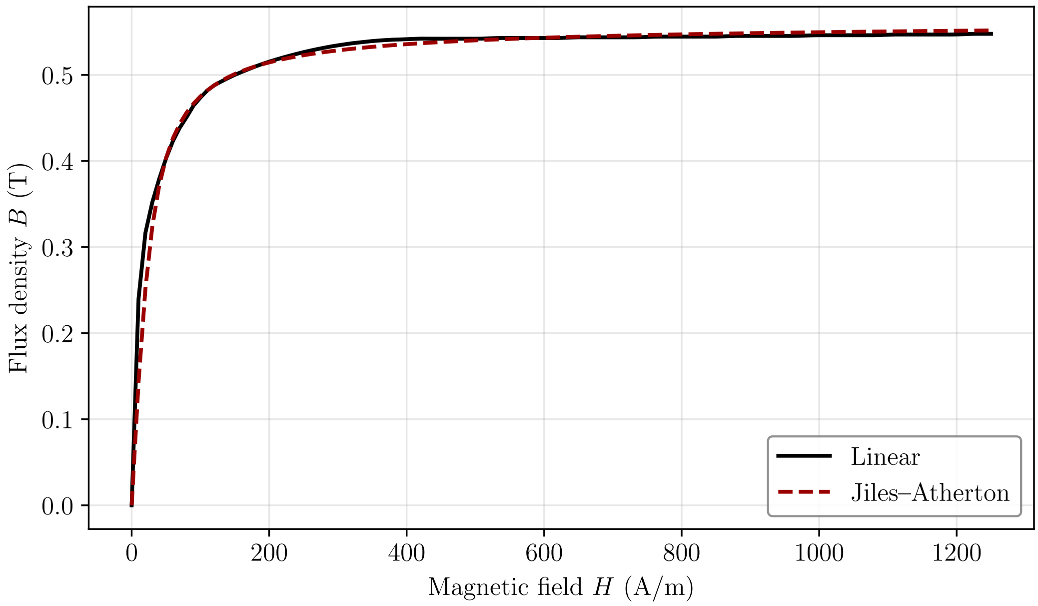


Figure 4.7: Comparison of 20ºC $B - H$ curves for TDK PC95 ferrite by linear interpolation and anhysteretic Jiles–Atherton fit identified by non-linear least squares.

Given that Maxwell requires a single-valued $B(H)$ relation, the anhysteretic J–A backbone identified here provides a more physics-informed alternative to purely linear temperature projection while remaining fully compatible with the solver requirements. At 20 °C, the J–A curve exhibits strong concordance with the linear baseline yet reproduces Langevin-type curvature around he knee, which the linear cannot. On this basis, J–A dataset was selected for the simulations. It preserves the robustness, better results underlying material physics near the knee.

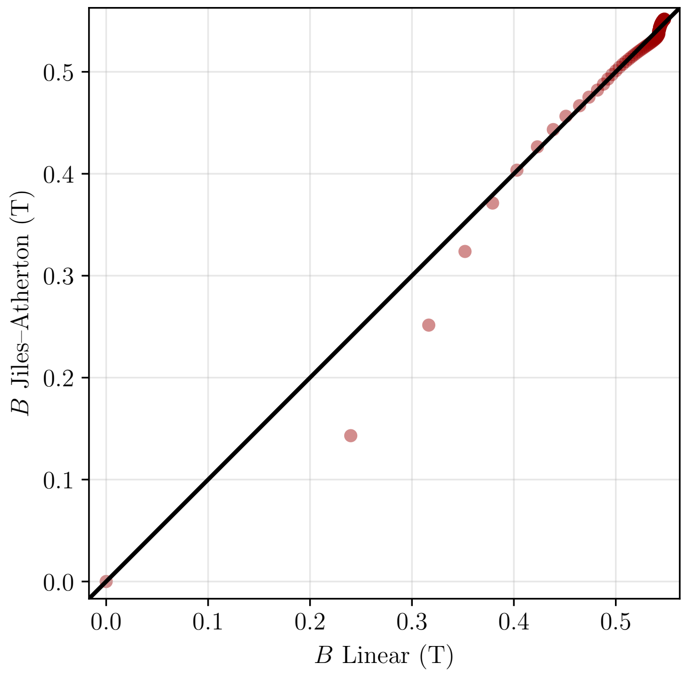


Figure 4.8: Scatter fo paired 20 °C flux density ordinates of Jiles–Atherton fit over the 1:1 parity line.

### 4.3.3 Shieldings

To confine EMF leakage and induced currents in nearby structural parts, a conductive plate of aluminium was modelled as a shielding. This approach follows established mitigation practices in IPT systems operating in the 85 kHz band defined for automotive wireless charging, and is consistent with the compliance objectives set by SAE J2954 and IEC 61980-3 standards. SAE J2954 further provides practical guidance for vehicle and ground assemblies, including minimum aluminium shielding plate thickness of 0.7 mm, which was adopted here as the baseline for FEA modelling. The IEC 61980-3 standard does not mention a thickness, but in the auxiliary drawings it represents the shielding as 1 mm, without issuing guidelines regarding this measurement.

According to reference [99], the field magnitude decays exponentially with depth. At the operating frequency of $f = 85\text{kHz}$, using aluminium with $\mu_r = 1.000$ and $\sigma = 38 \times 10^7 \text{S/m}$, the skin depth will be given by Equation 4.17.

$$\delta = \sqrt{\frac{2}{\omega\mu\sigma}} = \sqrt{\frac{2}{2\pi f \mu_0 \mu_r \sigma}} = 0.28\text{mm} \tag{4.17}$$

Considering the minimum thickness of $0.7$ mm referred to in the SAE J2954 standard, it can be seen that it approximately follows the triple thickness rule to reduce the skin depth. Considering that the thickness $t = 0.7$ mm, therefore $t/\delta = 2.5$, the decay of the magnetic field for a thickness $t$ is given by Equation 4.18.

$$B(t) = B(0)e^{-t/\delta} \tag{4.18}$$

Therefore, for a plate thickness $t$, the transmitted fraction would be approximately $e^{-t/\delta}$. For the case study, it would be $e^{-t/\delta} = 0.008211$, meaning that only $8.2\%$ of the field amplitude would be transmitted, or $20\log_{10} e^{-t/\delta} = 2.7$dB.

The Table 4.12 represent the electromagnetic properties assigned tot he aluminium shielding in the Ansys Maxwell.

Table 4.12: Aluminium properties used for the shielding in Ansys Maxwell [100].

| Parameter | Symbol | Assigned value |
|---|---|---|
| Relative permittivity (–) | $\varepsilon_r$ | $1.000$ |
| Relative permeability (–) | $\mu_r$ | $1.000$ |
| Bulk conductivity (S/m) | $\sigma$ | $38 \times 10^7$ |

Aluminium is modelled as non-magnetic, and a good conductor and as a shielding actuator reducing the magnetic field on the areas that do not contribute to the efficiency of the system.

## 4.4 Excitations and external circuit

In this study, the primary coils are excited by a current-source regulated at 38 A (rms) at a frequency of 85 kHz. The transmitting side employs an SS compensation network. On the secondary side, the secondary coil also has an SS compensation network and powers a purely resistive 10 Ω load, which represents the equivalent input resistance of the rectifier and DC–DC stage of the on-board charger.

The use of an SS topology that powers a nominal resistive load is consistent with many IPT and DIPT prototypes reported for the charging of EVs, where transmission efficiency and transfer power are evaluated using series–series compensation under fixed load conditions [8, 101]

Furthermore, selecting an operating frequency of 85 kHz aligns the design with the frequency band recommended by the SAE J2954 and IEC 61980-3, which specifies 85 kHz as the nominal resonant frequency for automotive WPT systems [3, 47].

## 4.5 Design of Experiments and generation of datasets

Two numerical datasets were constructed to support the surrogate modelling, sensitivity analysis and optimisation tasks, both having as outputs the coupling coefficients and the maximum magnitude of the magnetic flux density on the top, left and right control planes. The first dataset comprises 2200 instances and was generated by varying only the geometric design parameters of the coupler, while keeping the relative position between the pads fixed at $x = 1000$mm, $y = 0$mm and $\alpha = 0$. This dataset was specifically devised for the global sensitivity analysis: a sparse PCE surrogate model was identified from these samples and the corresponding Sobol' indices were computed to quantify the relative influence of each geometric variable. A second dataset, containing 2500 instances, was then constructed by sampling the control variables within the bounds $0\text{mm} \leq x \leq 4000\text{mm}$,$-300\text{mm} \leq y \leq 300\text{mm}$ and $-20\ ° \leq \alpha \leq 20°$. This second dataset provides a joint representation of geometric and positional variability over the relevant misalignment space and forms the basis for the subsequent surrogate modelling and multi-objective optimisation studies. The geometrical boundaries are represented in Table 4.13.

Table 4.13: Design variables and geometrical bounds applied to generate the design of experiments for the control parameters and primary and secondary coil geometry.

| Symbol | Description | Geometrical bounds | | |
|---|---|---|---|---|
| | Control parameters | Min | Max | Unit |
| $x$ | Longitudinal movement | 0 | 4000 | mm |
| $y$ | Lateral misalignment | -300 | 300 | mm |
| $\alpha$ | Angular misalignment | -20 | 20 | degrees |
| | Primary coil parameters | Min | Max | Unit |
| $w_{i,1}$ | Coil interior width | 25 | 450 | mm |
| $w_{e,1}$ | Coil exterior width | 350 | 600 | mm |
| $l_{i,1}$ | Coil interior length | 500 | 1750 | mm |
| $l_{e,1}$ | Coil exterior length | 1850 | 1950 | mm |
| $w_{f,1}$ | Ferrite exterior width | 400 | 650 | mm |
| $t_{f,1}$ | Ferrite thickness | 5 | 50 | mm |
| $w_{s,1}$ | Shield exterior width | 500 | 1000 | mm |
| $t_{s,1}$ | Shield thickness | 0.7 | 20 | mm |
| $s_{sf,1}$ | Spacing between shield and ferrite | 0 | 50 | mm |
| $s_{cf,1}$ | Spacing between coil and ferrite | 0 | 50 | mm |
| $N_1$ | Number of windings | 5 | 10 | — |
| | Secondary coil parameters | Min | Max | Unit |
| $w_{i,2}$ | Coil interior width | 200 | 250 | mm |
| $w_{e,2}$ | Coil exterior width | 350 | 400 | mm |
| $l_{i,2}$ | Coil exterior length | 950 | 1000 | mm |
| $w_{f,2}$ | Ferrite exterior width | 350 | 650 | mm |
| $l_{f,2}$ | Ferrite exterior length | 950 | 1050 | mm |
| $t_{f,2}$ | Ferrite thickness | 5 | 50 | mm |
| $w_{s,2}$ | Shield exterior width | 400 | 700 | mm |
| $t_{s,2}$ | Shield thickness | 0.7 | 20 | mm |
| $s_{sf,2}$ | Spacing between shield and ferrite | 0 | 50 | mm |
| $s_{cf,2}$ | Spacing between coil and ferrite | 0 | 50 | mm |
| $N_2$ | Number of windings | 5 | 10 | — |

## 4.6 Solver convergence

Ansys Maxwell employs an adaptative finite-element analysis in which coarse mesh is solved, local error is estimated, and the mesh is selectively refined in regions of highest error. This process improves the accuracy of the solution. After each adaptative pass, the solver recomputes the fields and repeats this cycle until used-defined stop criteria are satisfied ou the maximum number of passes is reached. In non-transient solutions, refinement is driven by energy-based error metrics, such as Total Energy, Energy Error (%), ΔEnergy (%), directly related to the Number of Tetrahedra.

This study applied an Ansys AC Magnetic analysis, considering that the fields are harmonic at a specified frequency and that the method solves $H$. The solver calculates the Total Energy, which is given as the integral volume of the energy density (Equation 4.19).

$$U = \iiint_V \frac{1}{4} Re\{B \cdot H^* + (E \cdot D^*)\} dV \tag{4.19}$$

In this Equation, $B$ stands for the magnetic flux density, $H$ is the magnetic field strength, $E$ is the electric field and $D$ is the electric displacement. The superscript $^*$ denotes a complex conjugate and $\cdot$ represents a dot product. The factor $1/4$ is found in the expression as peak values are considered.

After each adaptative pass, the solver evaluates a finite-element residual for the governing equations and from it derives and energy-based error indicator. The reported Energy Error (%) is a normalised metric by the total magnetic field energy of the current adaptative pass (Equation 4.20).

$$\text{Energy Error}(\%) = \frac{U_{error}}{U_{total}} \times 100 \tag{4.20}$$

Relative to the previous pass, the solver also reports the change in total energy between consecutive passes — labelled as $\Delta U(\%)$. The quantity is computed as in Equation 4.21.

$$\Delta U(\%) = \frac{|U^{(p)} - U^{(p-1)}|}{U^{(p-1)}} \tag{4.21}$$

These metrics explain and govern the mesh growth, with the Number of Tetrahedra increasing only where the discretisation contributes most to the Energy Error (%) defined in Equation 4.20. In the regions with high error, the solver subdivides those elements first. Hence, the element count rises pass-by-pass at a certain predefined rate. The adaptative process proceeds until both the Energy Error (%) and $\Delta U$ (%) falls below the user-specified Percent Error at which the refinement ceases.

Table 4.14 summarises the adaptative settings used for the AC Magnetic Simulations.

Table 4.14: Solver settings for the adaptive AC Magnetic analysis.

| | |
|---|---|
| Maximum Number of Passes | 50 |
| Percent Error (target) | 1 % |
| Refinement per Pass | 30 % |
| Minimum Number of Passes | 5 |
| Minimum Converged Passes | 5 |
| Solve Matrix | Only after converging |

These parameters set the convergence targets that underpin the Energy Error (Equations 4.20 and $\Delta$ Energy (Equation 4.21, and therefore frame the interpretation of the convergence history represented in Figure 4.9

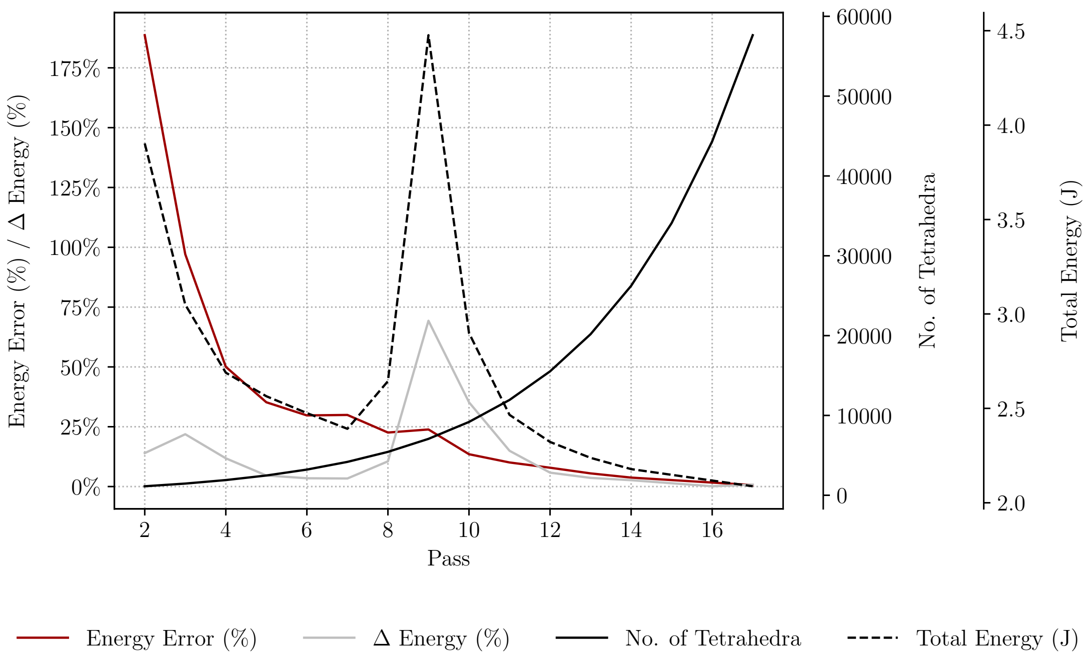


Figure 4.9: Convergence history of the AC Magnetic solution: Energy Error (%), $\Delta$ Energy (%) between passes, Total Energy $U$ (J) and Number of Tetrahedra for each adaptative pass.

In the early passes (2-5), the energy error decreases rapidly as the coarse mesh is corrected in the highest-gradient regions. The $\Delta$ Energy exhibits a decreasing trend, while the Number of Tetrahedra increases modestly but consistently. In the middle passes (8-10), the sharp spike in $\Delta$ Energy and Total Energy indicates a significant change in the mesh. This is a common change when the mesh refinement finally resolves a thin edge or skin-depth layer, after which the energy baseline re-levels. This sudden increase in $\Delta$ Energy and Total Energy is favourable, indicating that a critical feature has been correctly meshed. In the late passes (12-18), both Energy Error and $\Delta$ Energy decay to a value that tends towards zero as the Number of Tetrahedra increases significantly. Convergence is achieved when the Energy Error and $\Delta$ Energy decay to values below 1%.

## 4.7 Computational infrastructure and software

All numerical simulations and post processing were performed on a dedicated HP Z620 workstation. The system is equipped with an Intel® Xeon® CPU E5–2620 0 running at 2.00 GHz, providing six physical cores and twelve logical processors, and with 128 GB of system memory. A discrete NVIDIA Quadro 410 graphics processing unit was used to support the graphical interface of the finite element pre and post processing tools. Analyses were performed using the Ansys Maxwell and Ansys Circuit modules within the Ansys Electronics Desktop Student 2025 R2 software.

This software suite was used to set up the three dimensional finite element models, to solve the AC magnetic field problems for the different misalignment scenarios, and to extract the circuit level quantities required for the subsequent optimisation and sensitivity analysis stages. The overall computational cost of the study was dominated by the repeated solution of these three dimensional Maxwell models for different combinations of geometric parameters and misalignment conditions.

# 5 Global sensitivity analysis

This chapter presents the global sensitivity analysis of the DIPT system based on PCE surrogates. It begins by describing the construction, validation, and error metrics of the replacement models, as well as the definition of the training sets and the input and output variables. Next, the probability density functions of the responses are obtained, and the Sobol indices associated with the coupling coefficients and magnetic flux density in the control planes are calculated and discussed. Finally, the information provided by the sensitivity indices is synthesised to identify the most influential geometric parameters, analyse the trade-offs between coupling efficiency and exposure to electromagnetic fields, and support the selection of decision variables for the optimisation problem.

## 5.1 Construction and validation of PCE surrogate models

The PCE surrogates were constructed in the UQ[py]Lab framework from the electromagnetic simulation campaign performed in Maxwell. The input space is defined by the 22 geometric variables of the coupler, limited by the intervals in Table 4.13, from which 2200 geometric combinations were generated and evaluated.

### 5.1.1 Training datasets and input-output definition

The DoE in was generated in Maxwell using the Optimal Space-Filling (OSF) Design, which is an optimised Latin hypercube sampling maximizing the distances between experiments or points. This strategy ensures that no two points are too close from each other and that the variable bounding is fully populated and represented. In this setting, the OSF algorithm starts from a Latin hypercube sampling and iteratively repositions the points so as to maximise the minimum pairwise distance while preserving the constraints, which leads to an almost uniform coverage of the 22 dimensional input domain and is particularly suited to computer experiments and surrogate modelling. A pseudo-random seed equal to zero was used to make the resulting DoE reproducible [97].

The number of samples was selected as a compromise between accuracy and computational cost: for regression-based PCE, the size of the experimental design is typically chosen to be of the same order or a few times larger than the number of retained polynomial basis terms, in order to obtain a well-conditioned least-squares system, and

2200 OSF points were therefore adopted as the maximum affordable sample size on the available hardware. The same DOE is used for all quantities of interest (coupling coefficients and maximum magnetic flux density on the control planes), and its suitability for surrogate construction is assessed a posteriori by the cross-validation and error metrics discussed in Section 5.1.3.

The raw results were exported from Maxwell in several tables for coupling coefficients, magnetic flux density on the control planes, and other auxiliary outputs, and subsequently consolidated into a single dataset. During this pre-processing stage, non-essential columns were removed, units were made consistent with the notation adopted in this work, and column names were harmonised.

### 5.1.2 Polynomial basis, truncation scheme and sparsity strategy

Given that all geometric variables are modelled as independent uniform random inputs within the bounds of Table 4.13, the PCE surrogates are built in UQ[py]Lab using the tensor products of univariate orthonormal polynomials associated with the uniform distribution, which corresponds to a Legendre–type polynomial basis [102].

The training configuration summarised in Table 5.1 shows that all surrogates are built on the same experimental design, with 22 input variables and 2200 full model evaluations, while the degree of polynomial and the truncation parameters are tailored to each quantity of interest. The values represent the final evaluation on the PCE surrogates.

Table 5.1: Summary of the PCE configuration, polynomial truncation and basis sizes for the different input parameters.

| Parameter | $k_{11,2}, k_{12,2}$ | $\max \lvert B\rvert_{\text{top}}$ | $\max \lvert B\rvert_{\text{left}}$ | $\max \lvert B\rvert_{\text{right}}$ |
|---|---|---|---|---|
| No. of input variables | 22 | 22 | 22 | 22 |
| Maximal degree | 4 | 7 | 7 | 7 |
| $q$-norm | 1.00 | 0.50 | 0.50 | 0.50 |
| Size of full basis | 1875 | 826 | 826 | 848 |
| Size of sparse basis | 174 | 87 | 60 | 92 |
| Full model evaluations | 2200 | 2200 | 2200 | 2200 |

For the coupling coefficients $k_{11,2}$ and $k_{12,2}$ , the full basis contains 1875 candidate terms, so the least-squares system used to identify the PCE coefficients is determined. For the magnetic-flux-density surrogates, the hyperbolic truncation leads to smaller full bases, 826 to 848 terms, which increases this ratio to approximately 2.6, yielding more comfortable conditions for regression. After sparse regression, only 174, 87, 60, and 92 terms are retained for $k_{11,2}$, $k_{12,2}$ ,$\max |B|_{\text{top}}$, $\max |B|_{\text{left}}$ and $\max |B|_{\text{right}}$ respectively. This reduction indicates that the information contained in the 2200 training samples can be represented by a relatively small subset of polynomial interactions, suggesting that the effective dimensionality of the problem is lower than the nominal 22 inputs and that the calibrated PCE surrogates are both parsimonious and adequately supported by the available training data.

The convergence plots in Figure 5.1 represent, for all quantities of interest, the LOO error $\epsilon_{LOO}$ decreases very rapidly during the first LARS iterations and then approaches a plateau, indicating that only a relatively small number of basis functions is needed to capture the dominant response features. In Figure 5.1a, corresponds to the coupling-coefficient surrogates $k_{11,2}$ $k_{12,2}$. It is visible that the error drops by several orders of magnitude within the first 20 to 30 iterations, after which additional terms provide only marginal improvements, which is consistent with the very small final $\epsilon_{LOO}$ values in Table 5.2.

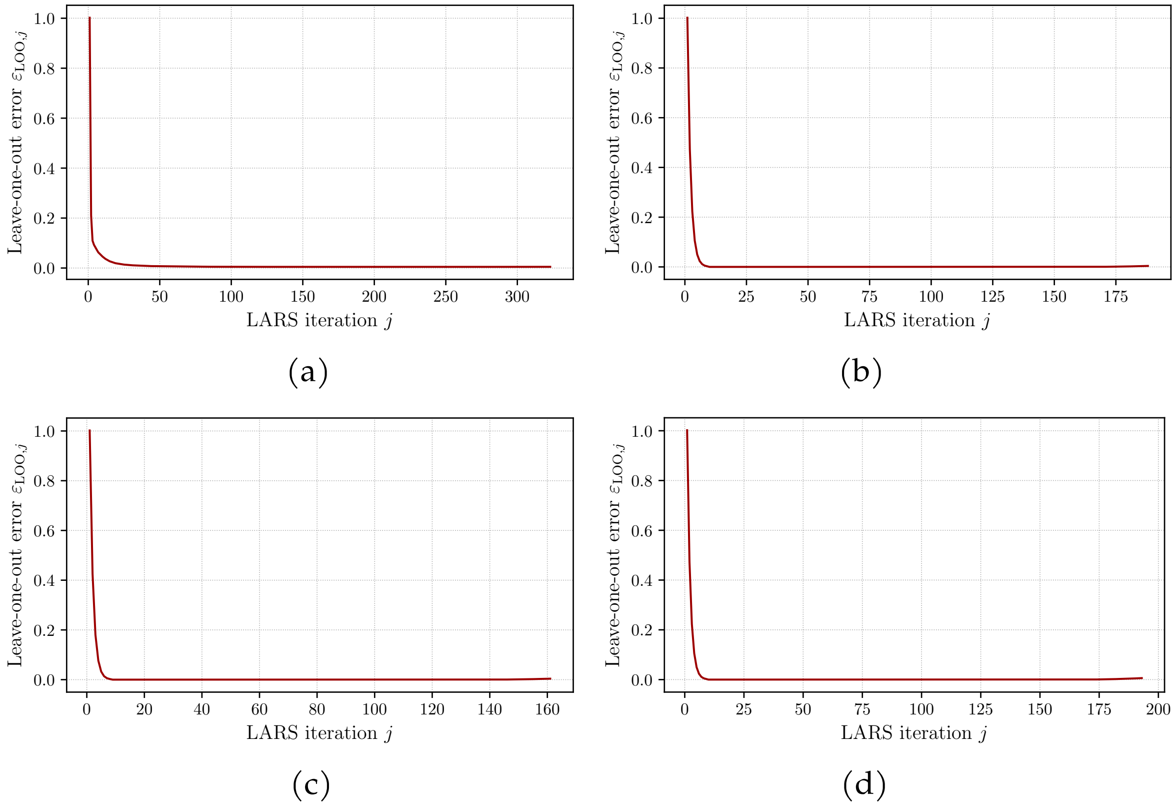


Figure 5.1: Evolution of the leave-one-out error $E_{\mathrm{LOO}}$ along the LARS iterations for the sparse PCE surrogates of: a) coupling coefficients $k_{11,2}$ and $k_{12,2}$, b) maximum magnetic flux density on the top control plane $\max|B|_{\mathrm{top}}$, c) maximum magnetic flux density on the left control plane $\max|B|_{\mathrm{left}}$ and d) maximum magnetic flux density on the right control plane $\max|B|_{\mathrm{right}}$.

The magnetic-flux-density surrogates in Figure 5.1 b,c and d represent a similar qualitative behaviour, with a steep initial decay followed by a slower convergence phase, although the asymptotic $\epsilon_{lOO}$ levels remain higher than for the coupling coefficients, reflecting the stronger non-linearity of the responses. In general, Figure 5.1 confirms that the sparse PCE strategy produces stable surrogates whose predictive precision improves quickly with the number of active basis functions and then saturates, according to the basis sizes reported in Table 5.1.

### 5.1.3 Error metrics

The validation metrics in Table 5.2 indicate that the PCE surrogates reproduce the original model responses with considerable accuracy for all quantities of interest.

Table 5.2: Leave-one-out validation errors and basic statistics of the PCE surrogates for the different quantities of interest.

| Parameter | $k_{11,2}$,$k_{12,2}$ | $\lvert B\rvert_{\text{top}}$ | $\lvert B\rvert_{\text{left}}$ | $\lvert B\rvert_{\text{right}}$ |
|---|---|---|---|---|
| $\epsilon_{LOO}$ | $3.728 \times 10^{-3}$ | $3.890 \times 10^{-2}$ | $6.171 \times 10^{-2}$ | $5.669 \times 10^{-2}$ |
| Modified $\epsilon_{LOO}$ | $4.479 \times 10^{-3}$ | $4.256 \times 10^{-2}$ | $6.563 \times 10^{-2}$ | $6.233 \times 10^{-2}$ |
| Mean value | 0.3763 | 52.3925 | 24.2474 | 23.5579 |
| Standard deviation | 0.0692 | 12.9193 | 6.6475 | 6.5193 |
| Coefficient of variation | 18.390% | 21.659% | 27.415% | 27.674% |

The LOO error for the coupling coefficients $k_{11,2}$ and $k_{12,2}$ is $\epsilon_{\text{LOO}} = 3.728 \times 10^{-3}$. For the magnetic flux density on the three control planes, the LOO errors are more pronounced but still relatively small. The modified LOO errors are only slightly larger than the original LOO errors for all outputs.

The remaining statistics provide further insight into how these errors compare with the natural variability of each response across the design space. The standard deviations of the PCE predictions are at least one order of magnitude larger than the corresponding LOO errors, showing that the surrogate models capture most of the underlying variation rather than numerical noise. The coefficients of variation, ranging from $18.390\,\%$ for the coupling coefficients to about $27.674\,\%$ for $\max\lvert B\rvert_{right}$, confirm that the responses exhibit substantial relative variability with respect to their mean levels, particularly for the lateral control planes. Because the surrogate errors are very small compared with both the mean and the standard deviation, the PCE models can be regarded as sufficiently accurate for global sensitivity analysis, where reliable estimates of trends and relative changes in $k_{11,2}$, $k_{12,2}$ and the magnetic flux density are more important than reproducing individual simulations exactly.

## 5.2 Probability density functions

The agreement between the surrogate and the deterministic computational model can also be assessed by comparing the PDFs of the quantities of interest. Figure 5.2a represents the estimated PDF of the coupling coefficients $k_{11,2}$ and $k_{12,2}$ obtained from the PCE surrogate and from the FEM simulations.

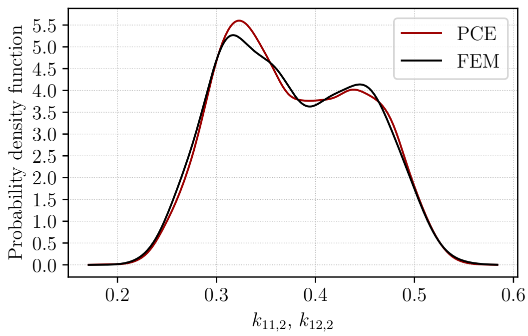


(a)

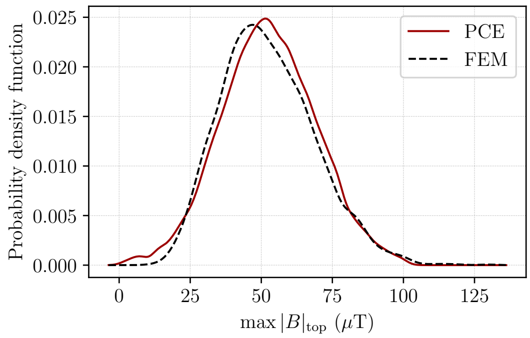


(b)

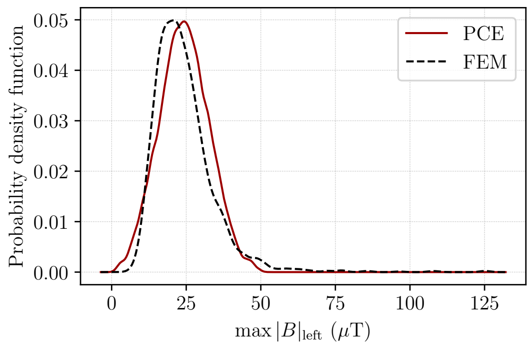


(c)

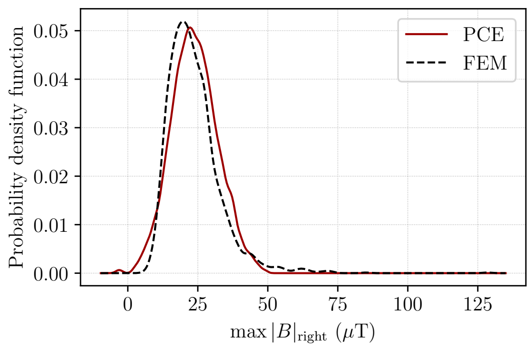


(d)

Figure 5.2: Comparison of estimated probability density functions by polynomial chaos expansions surrogate and finite element method for the a) $k_{11,2}$ and $k_{12,2}$; b) $\max|B|_{top}$ and c) $\max|B|_{left}$ and d) $\max|B|_{right}$

The two curves almost coincide over the whole support of the distribution and exhibit the same multimodal structure, with a dominant mode around $k \approx 0.33$ and a secondary shoulder at higher coupling values. The PCE curve is slightly smoother and presents a marginally higher peak probability, which is consistent with the small but LOO errors reported in Table 5.2. Overall, the surrogate accurately reproduces both the location and the shape of the distribution of the coupling coefficients, including the tails.

A similar level of agreement is observed for the maximum magnitude of the complex magnetic flux density on the three control planes, as depicted in Figure 5.2b, c and d. For the top plane, the PCE and FEM PDFs are almost indistinguishable, with the generic shape centred around $\max |B|_{\text{top}} \approx 55\ \mu$T and a comparable spread.

For the lateral planes, the PCE PDFs retain the same qualitative shape as the FEM curves and peak at very similar values of $\max |B|_{\text{left}}$ and $\max |B|_{\text{right}}$, although a slight systematic shift towards higher flux densities and a marginal broadening of the distributions can be observed. These differences are small in magnitude when compared with the overall width of the distributions and with the variability reported in Table 5.2, confirming that the PCE surrogates capture not only the mean response but also the uncertainty structure of the magnetic field with sufficient accuracy for the subsequent sensitivity and optimisation studies.

## 5.3 Sensibility analysis

The total Sobol' indices $S_T$ obtained for the coupling coefficients $k_{11,2}$ and $k_{12,2}$ are represented on the Figure 5.3 show a highly concentrated sensitivity pattern. When the geometric parameters are ordered by decreasing $S_T$, the interior length of the primary coils $l_{i,1}$ clearly dominates the variance decomposition, with $S_T \approx 0.815$. The second most important parameter is the exterior width of the secondary ferrite $w_{f,2}$ with $S_T \approx 0.110$. Together, these two geometrical variables account approximately for $92.5\%$ of the output variance. The next group of parameters has markedly smaller, but non-negligible, contributions. The space between the primary coils and the ferrite $s_{cf,1}$ ($S_T \approx 0.018$), the exterior width of the primary coils ($w_{e,q}$) ($S_T \approx 0.014$) and the interior width of the secondary coil $w_{i,2}$ ( $S_T \approx 0.011$). All remaining geometric parameters have total indices below $2 \times 10^{-2}$, the most relevant among them being the spacing between the primary coils and the widths of the ferrite and secondary coil, whose values are in the range $10^{-2}$ to $10^{-3}$. The parameters associated with the thickness of the shield, as well as the number of windings, have negligible total indices ($10^{-4}$). This pattern indicates that the variance of $k_{11,2}$ is mainly controlled by the longitudinal extent of the primary coils $l_{i,1}$ and, to a lesser extent, by the transverse ferrite footprint on the secondary side $w_{f,2}$, while most other dimensions act as second–order influences. When organised by subsystems, the primary coils represent the majority of the influence ($\sum S_T \approx 0.840$), followed by the ferrite of the secondary coil ($\sum S_T \approx 0.125$) and the primary ferrite ($\sum S_T \approx 0.026$). The shields account for only about $0.01 \sim 0.02$.

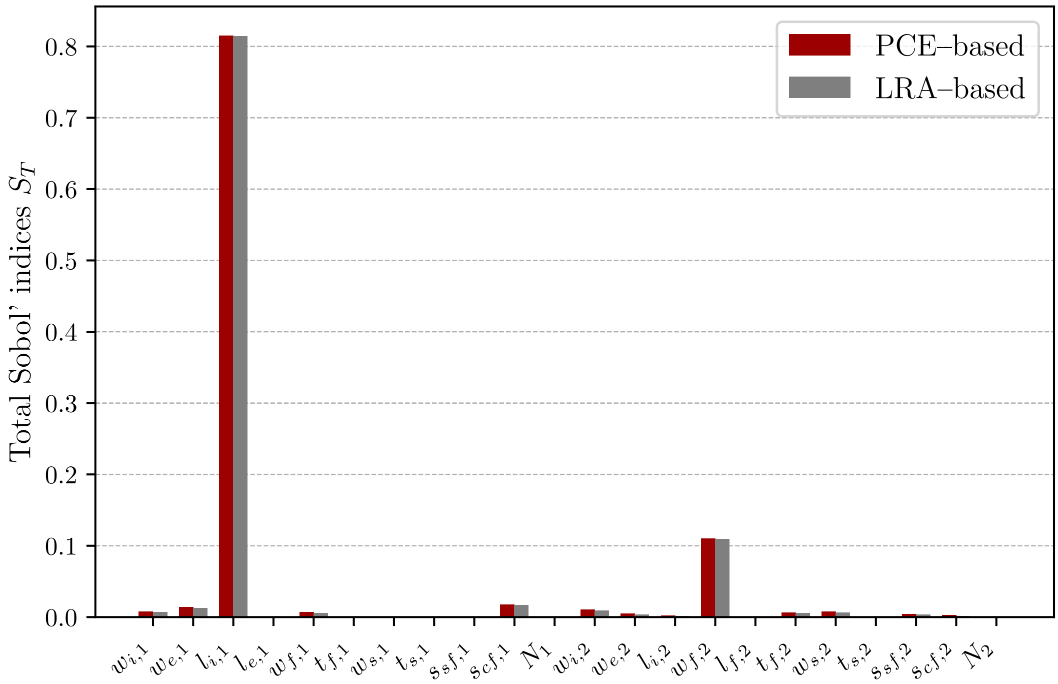


Figure 5.3: Total Sobol' indices $S_T$ for the coupling coefficients $k_{11,2}$ and $k_{12,2}$ for the DIPT coupler, comparing PCE–based and LRA–based estimates for all geometric design variables under nominal misalignment.

The prominent role of the interior length of the primary coil $l_{i,1}$ in the present sensitivity pattern is repeatedly shown to depend strongly on the length and width of the coil. For rectangular couplers, the study by [103] agrees with the finding that variations in the longitudinal dimension dominate the response of the coupling. In the broader DIPT literature [104, 105].

The width of secondary ferrite $w_{f,2}$ emerges as the second most influential parameter and also plays a role that is compatible with previous studies of ferrite plate optimisation in DIPT. The reference [106] studied a parametric optimisation of a 3 kW DIPT prototype and showed that the coupling factor is highly sensitive to the effective ferrite area and only weakly sensitive to its thickness in the non-saturated regime. In the present model, the relatively large $S_T(w_{f,2})$ together with the much smaller total effects of the thickness of both ferrites $(t_{f,1}, t_{f.2})$ are consistent with this research.

The week influence of shield dimensions and spacing between coils and ferrite mainly represents a fine tuning f the leakage–field distribution and local field homogeneity rather than affecting the overall coupling. This statement agrees with studies in which ferrite shielding ad spacings are adjusted to balance field-confinement and loss, while the dominant trends in coupling are still imposed by the coil dimensions themselves. In the present sensitivity results, this is reflected by the fact that ferrite dimensions on the receiver side still show non-negligible $S_T$ , while shield-related parameters, which primarily shape leakage rather than main flux, have near-zero total effects on the coupling coefficient once the principal coil dimensions are fixed.

The first–order Sobol' indices $S_1$ in Figure 5.4 convey a very similar picture. The primary coil interior length $l_{i,1}$ has $S_1 = 0.809$, so its main effect alone explains most of the variance of the coupling coefficients. The width of the secondary ferrite $w_{f,2}$ contributes another $S_1 = 0.104$, and the spacing between the primary coil and the ferrite has $S_1 = 0.0163$. Thus, three physically interpretable parameters account for approximately $92.9\%$ of the variance.

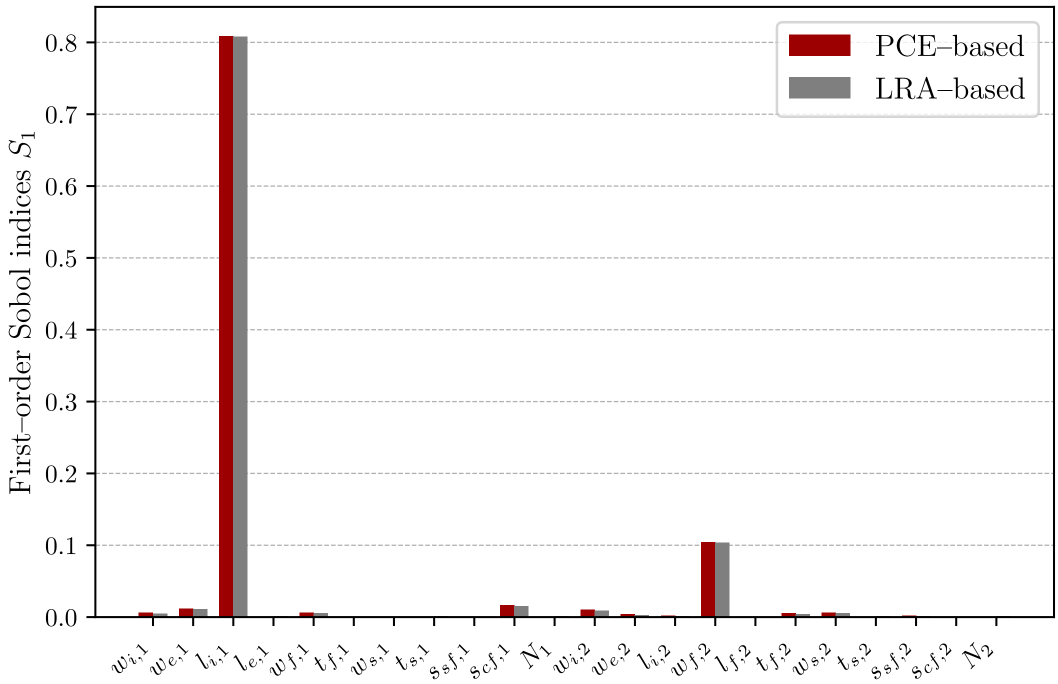


Figure 5.4: First–order Sobol' indices $S_T$ for the coupling coefficients $k_{11,2}$ and $k_{12,2}$ for the DIPT coupler, comparing PCE–based and LRA–based estimates for all geometric design variables under nominal misalignment.

When the $S_1$ indices are grouped by subsystems, the structure becomes even clearer. Summing the first–order indices of the primary coil dimensions ($w_{i,1}$, $w_{e,1}$, $l_{i,1}$ and $l_{e,1}$) yields $S_1 = 0.827$ representing the major influence on the coupling coefficients. Secondary ferrite parameters ($w_{f,2}$, $l_{f,2}$, $t_{f,2}$, $s_{sf,2}$ and $s_{cf,2}$) contribute $S_1 = 0.113$, while all remaining parameters, primary and secondary ferrites, shielding, and windings, jointly contribute less than $5\%$.

Adding all first–order indices yields $\sum S_1 = 0.986$, so first–order leaves $1.4\%$ for higher–order interactions between geometric variables. As expected, the sum of the total indices $\sum S_T = 1.014$, which includes the interaction contributions, can be summed to values greater than one. This percentage $\sum S_1$ is below one and $\sum S_T$ is sightly above, which is exactly the regime described in the literature on sensibility analysis [107].

Comparing the total and first–order Sobol' indices for each variable for each variable confirms that the most influential parameters act almost additively. For the interior length of the primary coil $l_{i,1}$, the difference between the total and first–order indices is $\Delta S = S_T - S_1 \approx 0.815 - 0.809 = 0.006$, representing a small percentage of variance originating from interactions with this geometric variable. For the width for secondary ferrite $w_{f,2}$, the corresponding difference is $\Delta S \approx 0.110 - 0.104 = 0.006$, and for the spacing between the primary coil and the ferrite $s_{cf,1}$ it is approximately $\Delta S \approx 0.0014$. In contrast, some low–influence parameters present relatively larger ratios of $(S_T - S_1)/S_T$, but the absolute contribution to variance remains negligible because both total and first–order indices are close to zero.

Figure 5.5 represents the total Sobol' indices $S_T$ for the maximum magnitude of the complex magnetic flux density $|B|_{top}$ evaluated on the "top" plane, comparing PCE–based and LRA–based estimates. The magnetic flux on the "top" plane is mostly governed by primary–side excitation and coil geometry. The largest total index is associated with the primary number of windings $N_1$, which corresponds to $S_T \approx 0.345$. The interior width $w_{i,1}$ and length of the primary coil $l_{i,1}$ also play an major role in $S_t \approx 0.188$ and $S_T \approx 0.191$, respectively.

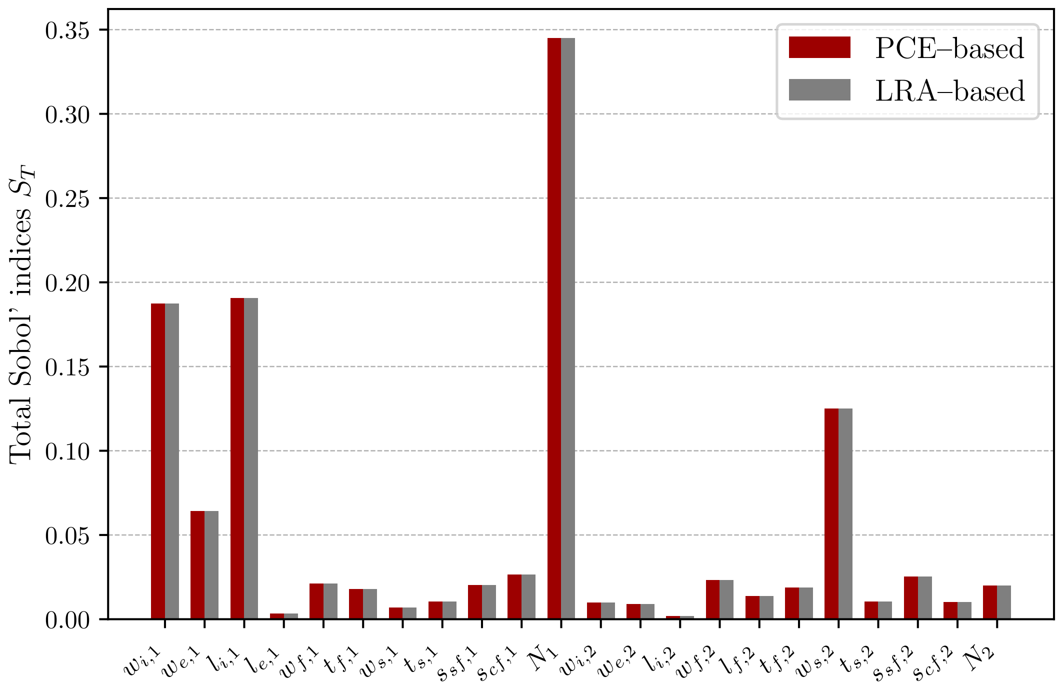


Figure 5.5: Total Sobol' indices $S_T$ for the maximum magnitude of the complex magnetic flux density $\max |B|_{top}$ evaluated on the top plane, comparing PCE–based and LRA–based estimates for all geometric design variables under nominal misalignment.

Quantitatively, the total effect for these three parameters combined sums $S_T(N_1) + S_T(w_{i,1}) + S_T(l_{i,1}) \approx 0.72$. Since the sum of all total indices is $\sum S_T \approx 1.16$, these three primary side quantities account for about $0.72/1.16 \approx 62\%$ of the total effect and with at least $72\%$ of the variance. A second group of influential parameters involves the secondary shield and ferrite geometries. The width of the secondary shield $w_{s,2}$, which exhibits a substantial total index of $S_T \approx 0.126$, while the width and thickness of the secondary ferrite and the spacing between the shield and the ferrite on the secondary side contribute with values in the range of $0.02$ to $0.03$. In contract, the remaining secondary side dimensions show only modest total effects $S_T \lesssim 0.02$. These results indicate that, on the secondary side, the maximum magnitude of the complex magnetic flux density $\max |B|_{top}$ is mode sensitive to how the ferrite–shield assembly guides and contains the field, rather than to fine details of the secondary winding.

When the total indices are grouped by physical subsystems, the dominance of the primary side becomes explicit. Summing over all geometrical parameters on the primary side yields a cumulative total effect $\sum S_T \approx 0.89$ whereas the corresponding sum for the dimensions on the secondary side yields $\sum S_T \approx 0.27$. As the total indices include interaction terms, these grouped sums do not represent disjoint fractions of variance, and their total $\sum S_T \approx 1.16$, slightly exceeds the unit, indicating the presence of non-negligible interactions between design variables.

This pattern is entirely consistent with the underlying electromagnetic theory. The magnetic flux density generated by a coil is linked to the magnetic force which is proportional to the product of the number of windings and the current. Since in the present study, the excitation current is fixed, variations of the number of windings of the primary coil directly influence the magnetomotive force and thus the local field levels. This strong dependence of the field on coil geometry and the number of windings is emphasised in recent work on IPT transmitter oil design [108].

The first–order Sobol' indices in Figure 5.6 represent the purely additive contribution of each geometrical parameters to the variance of the maximum magnitude of the complex magnetic flux density $\max |B|_{top}$ evaluated on the top plane.

The ranking of the first–order indices confirms the strong dominance of the primary–side system. The largest first–order index is achieved by the number of windings of the primary coil $N_1$, with $S_1 \approx 0.33$. The interior dimensions of the primary coil are the next most influential, a with the interior length $l_{i,1}$ and width $w_{i,1}$ corresponding to $S_1 \approx 0.18$ and $S_1 \approx 0.14$, respectively. Together, they account for about $0.65$ of the variance in $\max |B|_{top}$, which confirms the magnetomotive force on the primary winding.

At the level of individual variables, the leading contributors to $\max |B|_{top}$, $w_{i,1}$, and $l_{i,1}$, remain predominantly additive, with their interaction shares modest compared to their main effects, such as $S_T - S_1 \approx 0.016$ and $S_T - S_1 \approx 0.009$, respectively. In particular, the secondary shield width $w_s, 2$ and a group of ferrite and spacing variables hate total effect indices that are largely or almost entirely due to interactions, with $S_T - S_1$ accounting for approximately $80$ to $100\%$ of their total contribution. Together, the variables with a $S_1 \approx 0$ but non-zero $S_T$ already accumulate $\sum S_T \approx 0.09$ which is not a negligible share. The structure and contribution of geometric variables are consistent with the physics of DIPT and the relevant literature.

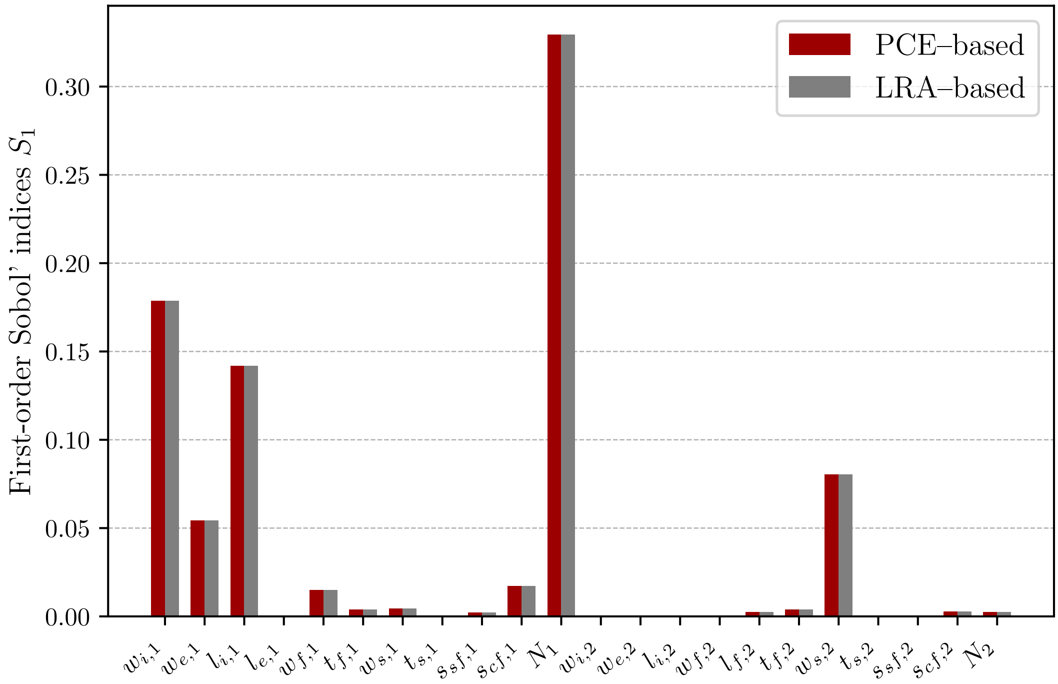


Figure 5.6: First–order Sobol' indices $S_1$ for the maximum magnitude of the complex magnetic flux density $\max |B|_{top}$ evaluated on the "top" plane, comparing PCE–based and LRA–based estimates for all geometric design variables under nominal misalignment.

Figures 5.7 and 5.8 show the total and first–order Sobol' indices of the maximum magnitude of the complex magnetic flux density evaluated on the left (a) and right (b) control planes, respectively. As the coupler geometry and the nominal operation conditions are symmetric with respect to the longitudinal mid-plane of the system, the PCE– and LRA–based Sobol' indices for the left and right planes are numerically indistinguishable. Each bar in the left plane lot has counterpart of essentially identical height in the right plane plot. PCE and LRA estimates are visually coincident across all variables.

The total Sobol' indices $S_T$ in Figure 5.7 captures both the main and interaction effects. The primary coil dimensions and number of windings remain the leading contributors, such the interior width, length, exterior width, and number of windings, with $S_T \approx 0.22$, $S_T \approx 0.15$, $S_T \approx 0.08$ and $S_T \approx 0.27$, but several parameters that were negligible at first–order bow display non–trivial effects. In particular, the primary shield thickness $t_{s,1}$, the spacing between the primary shield and ferrite and between the coil and ferrite present very small first–order indices but $S_T$ values in the range of $0.02$ to $0.06$. Similar patterns are found on the secondary side, where interior length, exterior width, ferrite length and thickness and number of windings have almost zero first–order indices but non-zero total indices, with $S_T$ values between approximately $0.01$ and $0.03$.

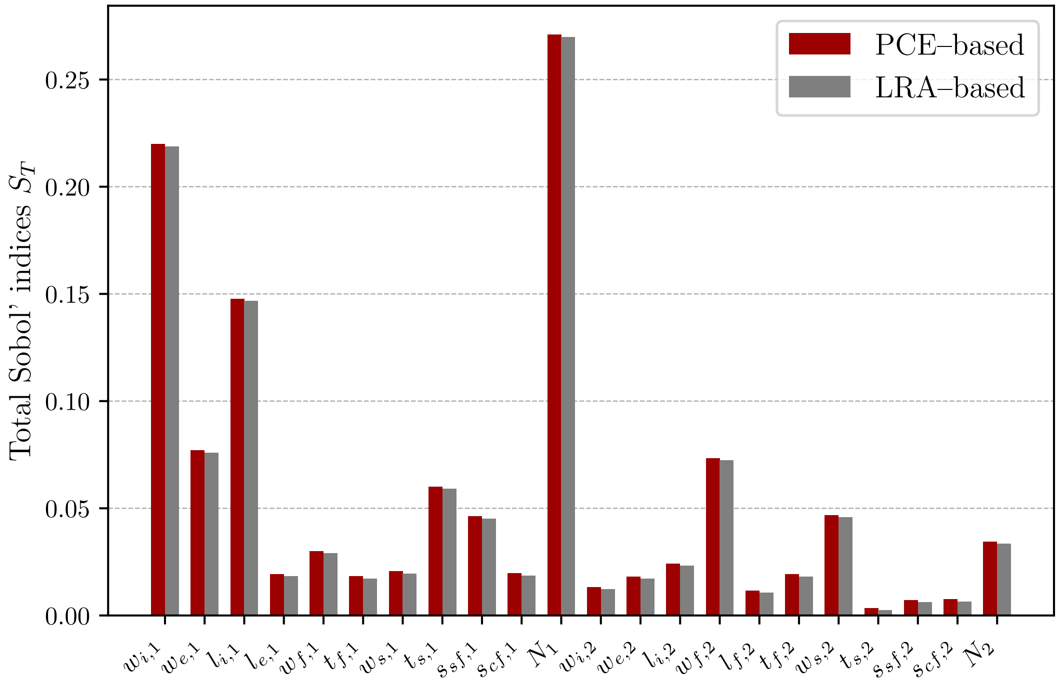


(a)

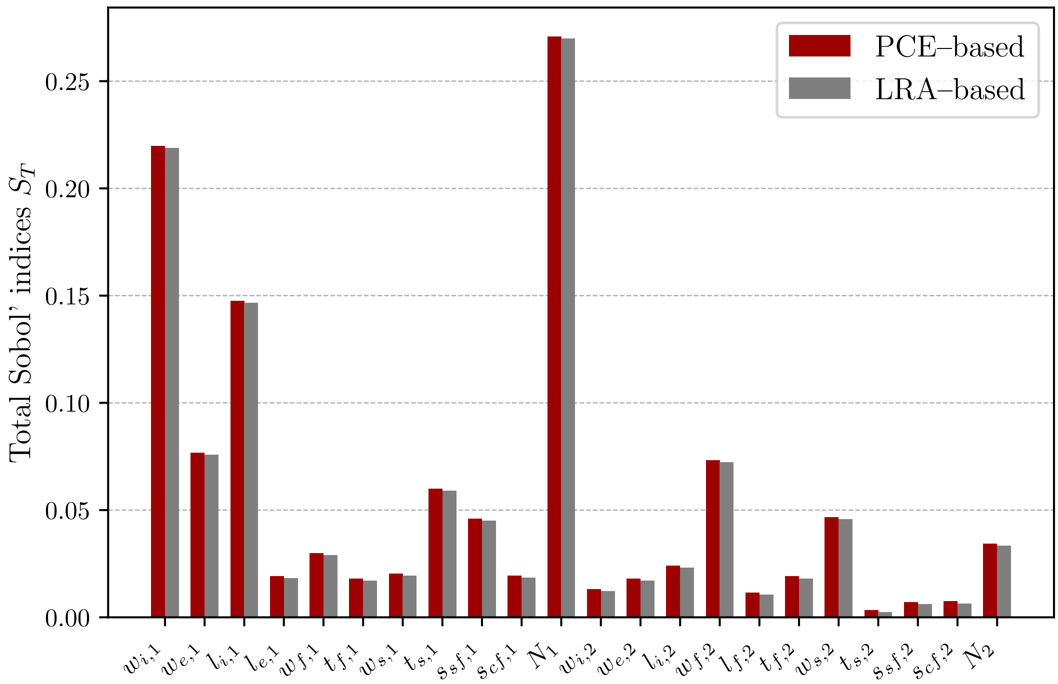


(b)

Figure 5.7: Total Sobol' indices $S_T$ for the maximum magnitude of the complex magnetic flux density $\max|B|$ comparing PCE–based and LRA–based estimates for all geometric design variables under nominal misalignment, with evaluation on the: a) left plane; b) right plane.

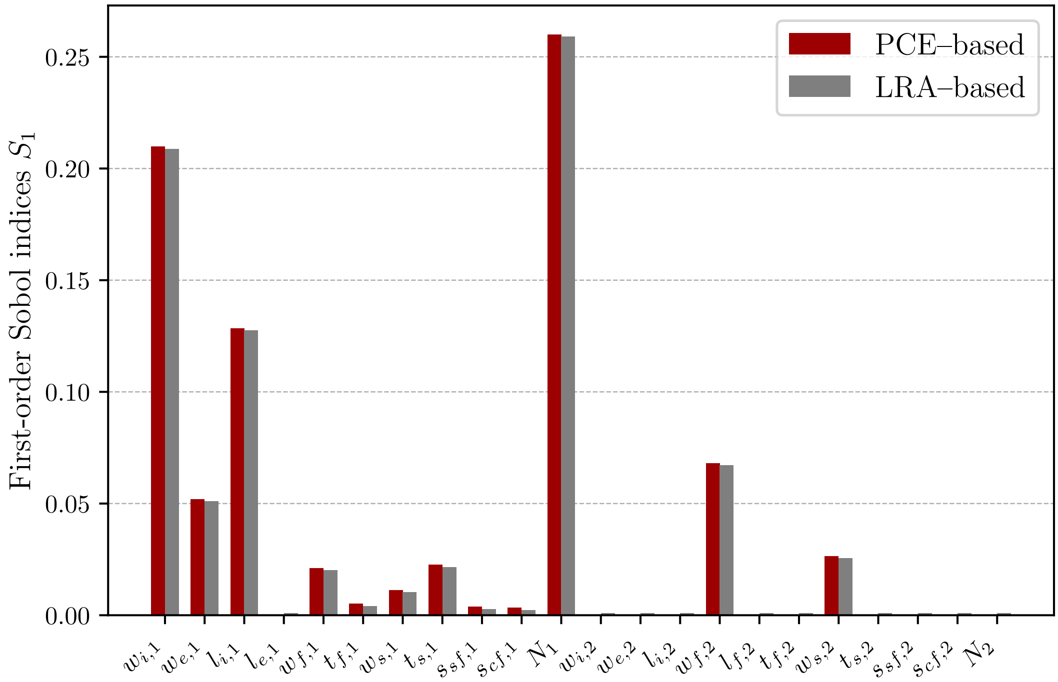


(a)

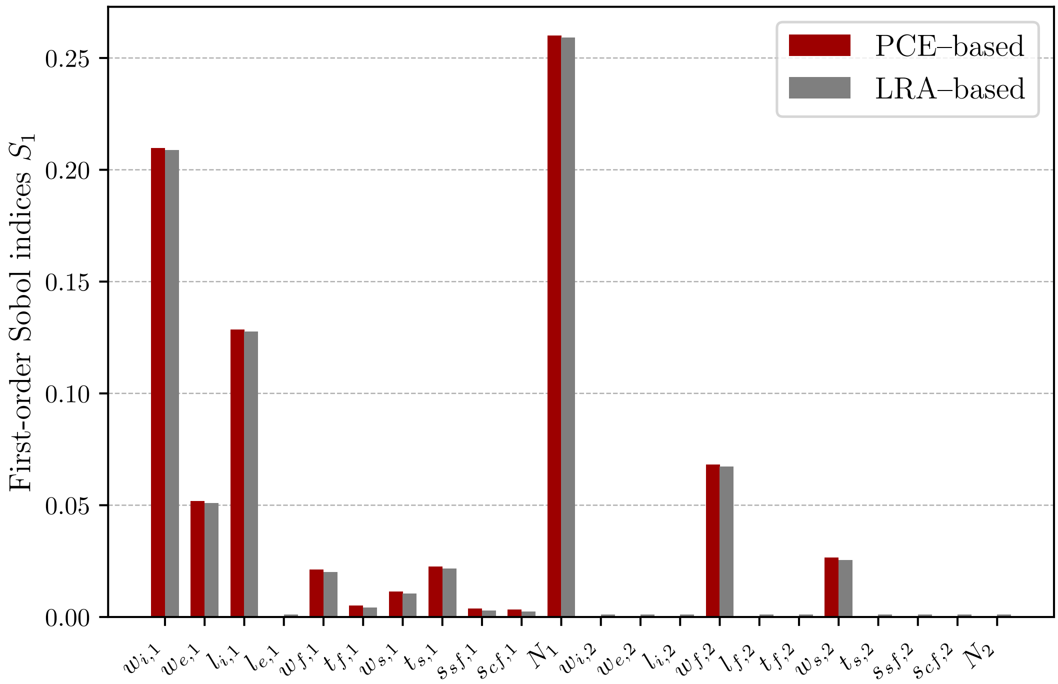


(b)

Figure 5.8: First–order Sobol' indices $S_1$ for the maximum magnitude of the complex magnetic flux density $\max|B|$ comparing PCE–based and LRA–based estimates for all geometric design variables under nominal misalignment, with evaluation on the: a) left plane; b) right plane.

The sum of total indices on all primary-side it produces $\sum S_T \approx 0.93$, while the secondary side variables contribute with $\sum S_T \approx 0.26$, as the global sum is $\sum S_T \approx 1.19$

is greater than the unit.

In terms of first–order indices $S_1$, Figure 5.8 confirms that the lateral control planes are dominated by the same primary side drivers as the top plane, but with a slightly different balance between coil windows and shielding effects. On both left and right planes, the largest first–order index is associated with the primary number of windings $N_1$, with $S_T \approx 0.26$, indicating that variations in the primary winding explain almost one third of the variance of $\max|B|$. The interior dimensions of the primary winding follow as the next most influential geometric parameters, with $S_1 \approx 0.21$ for the interior width $w_{i,1}$ and $S_1 \approx 0.13$ for the primary interior length $l_{i,1}$. Taken together, these variables with $N_1$ already account for approximately $0.6$ of the summed first–order indices. These variables represent the dominant additive design group that controls the field level in the lateral planes. Secondary side contributions at first–order are appreciably smaller but not negligible. The secondary ferrite width $w_{f,2}$ exhibits $S_1 \approx 0.07$, while the secondary shield width $w_{s,2}$ reaches $S_1 \approx 0.03$. Other secondary dimensions and clearances are essentially negligible at first–order, with $S_1$ values close to zero.

When the indices are grouped by sub-system, primary side parameters account for about $\sum S_1 \approx 0.72$, whereas the entire secondary side assembly contributes only with $\sum S_1 \approx 0.009$, reinsuring the conclusion that the lateral leakage field is primary controlled by the excitation and geometry of the primary system, with the secondary ferrite and shield dimension exerting a subordinate influence.

Finally, the fact that both the total and first–order Sobol' indices have been obtained from PCE and LRA surrogates, rather than from Monte Carlo simulations on the full Maxwell 3D model, is in line with the recent work on surrogate–assisted analysis of DIPT and IPT systems [8].

Overall, the Sobol indices obtained in this study characterise the relative importance of geometric variables for the nominal coupling condition (central position). In general terms, sensitivity analysis literature indicates that these indices depend on the distribution assumed for all input variables and may change when the statistics of other factors, such as misalignment, are fixed or modified.

## 5.4 Discussion and implications for optimisation

### 5.4.1 Identification of the most influential geometric parameters

The Sobol' indices obtained in the previous section provide a coherent picture of the geometric parameters that govern both coupling and magnetic field levels. For the coupling coefficients $k_{11,2}$ and $k_{12,2}$, the variance is mostly controlled by the interior length of the primary coil $l_{i,1}$ and, to a lesser extent, by the width of the secondary ferrite $w_{f,2}$. Other primary coil dimensions and a small number of clearances between coils and ferrites contribute at a secondary level, while shield dimensions and the number of windings have almost negligible influence on the coupling. In contrast, the maximum magnitude of the complex magnetic flux density on the control planes is mainly driven by the primary-side excitation and window dimensions: the number of primary windings $N_1$ and the interior length and width of the primary coil ($l_{i,1}$ and $w_{i,1}$) consistently exhibit the largest total and first–order indices for all three planes. Secondary-side ferrite and shield widths have moderate influence on the field levels, whereas most of the remaining dimensions act only through small interaction effects.

Taken together, these results indicate that a relatively small subset of design variables controls the key performance indicators of the DIPT coupler. The primary coil interior dimensions and the number of primary windings form a first group of drivers that simultaneously affect coupling and magnetic flux density. The secondary ferrite width, secondary shield width and a few selected clearances form a second group that has a more pronounced impact on field redistribution than on the dimensionless coupling factor. The remaining geometric parameters can be regarded as tertiary, as their total Sobol′ indices are at least one order of magnitude smaller and their contribution to the overall variance is marginal. This hierarchy of influences is central for interpreting the physical behaviour of the system and for understanding which dimensions are effectively controlling the responses explored in the optimisation stage.

### 5.4.2 Trade-offs between coupling efficiency and EMF exposure

The variables that appear simultaneously among the leading contributors to the variance of $k_{11,2}$, $k_{12,2}$ and of the maximum magnetic flux density on the control planes encode structural couplings between these quantities. In particular, the interior length $l_{i,1}$ and width $w_{i,1}$ of the primary coil, together with the number of primary windings $N_1$, have large Sobol′ indices for at least one coupling-related output and for all field-related outputs.

Conversely, several parameters play an asymmetric role across the two groups of outputs. The width of the secondary ferrite $w_{f,2}$ has a strong total effect on the coupling coefficients but only a modest contribution to the variance of the magnetic flux density, while the secondary shield width and certain spacings between ferrite and shield are much more influential for $\max|B|$ than for $k_{11,2}$ and $k_{12,2}$.

In this context, the role of the Sobol′ indices is primarily interpretative rather than prescriptive. The sensitivity analysis identifies which parameters are expected to drive most of the variation in coupling and EMF exposure and therefore provides a natural framework to interpret the Pareto fronts obtained in Chapter 6 and to explain why certain design trends emerge across the optimal solutions.

# 6 Machine learning optimisation

For multi–objective optimisation problems, there is usually no single optimal solution but rather a set of trade-off solutions representing a compromise between objectives. Pareto fronts present a visual representation of the algorithm solutions allowing the identification of candidate designs. All candidate designs, despite showing improvements in one parameter, show poor results for another parameter [109, 110]

Among existing methods, the Non-Dominated Sorting Genetic Algorithm II (NSGA-II) is a widely applied algorithm for multi-objective optimisation. It incorporates a fast non-dominated sorting procedure to rank solutions into different levels and a mechanism to retain the best solutions between geometries. Using this type of algorithm, NGSA-II enhances computational efficiency and maintains a well-distributed Pareto front [110]

## 6.1 Optimisation problem formulation

The optimisation problem is expressed in terms of a geometric design vector g, which gathers all independent design variables and is restricted to the admissible set $\mathcal{G}$. For any given geometry g, the operating conditions of the system are described by the misalignment and longitudinal position vector $\mathbf{m} = (x, y, \alpha) \in \mathcal{D}$, which spans the prescribed ranges of lateral offset $y$, angular misalignment $\alpha$ and vehicle position $x$ along the longitudinal axis. The surrogate is evaluated over this operating domain $\mathcal{D}$ and returns, for each pair $(\mathbf{g}, \mathbf{m})$, the coupling coefficients $k_{11,2}(\mathbf{g}, \mathbf{m})$ and $k_{12,2}(\mathbf{g}, \mathbf{m})$. From these response maps, the quantities $k_{11,2}^{\min}(\mathbf{g})$, $k_{11,2}^{\max}(\mathbf{g})$, $k_{12,2}^{\min}(\mathbf{g})$ and $k_{12,2}^{\max}(\mathbf{g})$ are defined as the minimum and maximum values attained by each coupling coefficient when $\mathbf{m}$ varies over $\mathcal{D}$. The corresponding amplitudes

$$A_{11,2}(\mathbf{g}) = k_{11,2}^{\max}(\mathbf{g}) - k_{11,2}^{\min}(\mathbf{g}), \qquad A_{12,2}(\mathbf{g}) = k_{12,2}^{\max}(\mathbf{g}) - k_{12,2}^{\min}(\mathbf{g}),$$

measure, for each geometry, the spread between the best and worst values of the coupling coefficients across all admissible misalignment and motion scenarios. The multi-objective optimisation problem is therefore constructed to identify designs g that, on the one hand, maximise the robustness of the coupling by increasing the minimum values $k_{11,2}^{\min}(\mathbf{g})$ and $k_{12,2}^{\min}(\mathbf{g})$, and, on the other hand, reduce the sensitivity to misalignment by minimising the amplitudes $A_{11,2}(\mathbf{g})$ and $A_{12,2}(\mathbf{g})$. These objectives are pursued under two classes of constraints: geometric constraints, which define the admissible design set $\mathcal{G}$ and ensure that the resulting coil, ferrite, and shielding dimensions are physically realisable, and MF exposure constraints, which impose that the magnetic flux density $B_p(\mathbf{g}, \mathbf{m})$ on each control plane $p \in \{\text{top}, \text{left}, \text{right}\}$ remains below the prescribed limit $B_{\text{lim}} = 27\ \mu\text{T}$ for all operating conditions $\mathbf{m} \in \mathcal{D}$.

The resulting geometric design problem can therefore be expressed as the following multi-objective optimisation problem, in which the decision vector g is chosen to maximise the minimum coupling coefficients and minimise their amplitude of variation over the operating domain $\mathcal{D}$, while satisfying the geometric and MF constraints:

$$
\begin{aligned}
& \max_{\mathbf{g}} \quad k_{11,2}^{\min}(\mathbf{g}), \quad k_{12,2}^{\min}(\mathbf{g}) && (6.1)\\
& \min_{\mathbf{g}} \quad A_{11,2}(\mathbf{g}), \quad A_{12,2}(\mathbf{g}) && (6.2)\\
\text{subject to} \quad & \mathbf{g} \in \mathcal{G}, && (6.3)\\
& k_{11,2}^{\min}(\mathbf{g}) = \min_{\mathbf{m}\in\mathcal{D}} k_{11,2}(\mathbf{g},\mathbf{m}), \quad k_{11,2}^{\max}(\mathbf{g}) = \max_{\mathbf{m}\in\mathcal{D}} k_{11,2}(\mathbf{g},\mathbf{m}), && (6.4)\\
& k_{12,2}^{\min}(\mathbf{g}) = \min_{\mathbf{m}\in\mathcal{D}} k_{12,2}(\mathbf{g},\mathbf{m}), \quad k_{12,2}^{\max}(\mathbf{g}) = \max_{\mathbf{m}\in\mathcal{D}} k_{12,2}(\mathbf{g},\mathbf{m}), && (6.5)\\
& A_{11,2}(\mathbf{g}) = k_{11,2}^{\max}(\mathbf{g}) - k_{11,2}^{\min}(\mathbf{g}), \quad A_{12,2}(\mathbf{g}) = k_{12,2}^{\max}(\mathbf{g}) - k_{12,2}^{\min}(\mathbf{g}), && (6.6)\\
& C(\mathbf{g}) \le C_{\max}, && (6.7)\\
& \max |B|_p(\mathbf{g},\mathbf{m}) \le 27\mu\text{T}, \quad \forall\, \mathbf{m} \in \mathcal{D},\ \forall\, p \in \{\text{top}, \text{left}, \text{right}\}. && (6.8)
\end{aligned}
$$

In addition to the multi-objective formulation in Equations 6.1 — 6.8, the geometric design vector g is restricted to an admissible set $\mathcal{G}$ defined by (i) simple bound constraints on each scalar design variable and (ii) a set of geometric consistency constraints that enforce a physically realisable coil–ferrite–shield arrangement on both the primary and secondary sides.

The bound constraints ensure that every design variable remains within the interval explored in the electromagnetic model and consistent with DoE limitations. Denoting generically by $\xi_j$ the $j$-th scalar component of g, one has

$$
\xi_j^{\min} \;\le\; \xi_j \;\le\; \xi_j^{\max}, \qquad j = 1, \ldots, n_g, \tag{6.9}
$$

where $\xi_j^{\min}$ and $\xi_j^{\max}$ are the lower and upper bounds reported in Table 4.13 for all geometric parameters.

Beyond these box constraints, additional inequalities are imposed to ensure that the coil windows are strictly contained within the corresponding ferrite and shield envelopes and that the difference between the width and length is sufficient to accommodate the prescribed number of turns, assuming an effective turn thickness of $5\ \mathrm{mm}$ per side [3]. The resulting geometric constraints can be written as

$$
\begin{aligned}
w_{i,1} \;&<\; w_{e,1} \;\leq\; w_{f,1} \;\leq\; w_{s,1}, && (6.10)\\
l_{i,1} \;&<\; l_{e,1}, && (6.11)\\
w_{e,1} - w_{i,1} \;&\geq\; 10\,N_1, && (6.12)\\
l_{e,1} - l_{i,1} \;&\geq\; 10\,N_1, && (6.13)\\
N_1 &\in \mathbb{N}, && (6.14)\\
w_{i,2} \;&<\; w_{e,2} \;\leq\; w_{f,2} \;\leq\; w_{s,2}, && (6.15)\\
w_{e,2} - w_{i,2} \;&\geq\; 10\,N_2, && (6.16)\\
l_{f,2} - l_{i,2} \;&\geq\; 10\,N_2, && (6.17)\\
N_2 &\in \mathbb{N} && (6.18)
\end{aligned}
$$

The chains of inequalities in 6.10 — 6.18 ensure that the interior coil windows $(w_{i,1}, l_{i,1})$ and $(w_{i,2}, l_{i,2})$ are strictly embedded within the corresponding ferrite and shield footprints, while the differences $w_{e,k} - w_{i,k}$ and $l_{\cdot,k} - l_{i,k}$ provide sufficient space to accommodate $N_k$ the windings on both sides of the bounding, consistent with the adopted turn build model.

In addition to these geometric consistency requirements, an economic constraint is introduced to discourage excessively large and materially intensive designs that would provide only marginal improvements in coupling performance. A scalar material index $C(\mathbf{g})$ is defined as

$$C(\mathbf{g}) = \sum_{k=1}^{2} \left(w_{s,k}\, l_{s,k}\, t_{s,k} + w_{f,k}\, l_{f,k}\, t_{f,k}\right), \quad k \in \{1, 2\} \tag{6.19}$$

which is proportional to the total shield and ferrite volumes on the primary ($k = 1$) and secondary ($k = 2$) sides. The admissible design set is further restricted by

$$C(\mathbf{g}) \;\leq\; C_{\max}, \tag{6.20}$$

where $C_{\max}$ denotes the maximum acceptable material index based on cost, mass and packaging considerations. This additional inequality, see (6.7), prevents the optimiser from simply enlarging the material dimensions to achieve robustness against misalignment at the expense of an impractical increase in material usage.

## 6.2 Random forest surrogate error metrics

The error metrics in Table 6.1 indicate that the random forest surrogates reproduce the coupling coefficients with very considerable accuracy.

Table 6.1: Objectives and coupling-coefficient ranges for the initial design and the selected NSGA–II candidate designs.

| Target | $R^2_{\text{train}}$ | $R^2_{\text{test}}$ | $\text{RMSE}_{\text{train}}(\mu T)$ | $\text{RMSE}_{\text{test}}(\mu T)$ |
|---|---|---|---|---|
| $k_{11,2}$ | 0.9924 | 0.9467 | $9.531 \times 10^{-3}$ | $2.814 \times 10^{-2}$ |
| $k_{12,2}$ | 0.9917 | 0.9488 | $9.940 \times 10^{-3}$ | $2.629 \times 10^{-2}$ |
| $\max \lvert B \rvert_{top}$ ( $\mu$T) | 0.9458 | 0.6078 | $3.746 \times 10^{0}$ | $1.054 \times 10^{1}$ |
| $\max \lvert B \rvert_{left}$ ( $\mu$T) | 0.9833 | 0.8667 | $8.899 \times 10^{-1}$ | $2.630 \times 10^{0}$ |
| $\max \lvert B \rvert_{right}$ ( $\mu$T) | 0.9850 | 0.8825 | $9.783 \times 10^{-1}$ | $2.607 \times 10^{0}$ |

For $k_{11,2}$ and $k_{12,2}$,the combination of high $R^2$ and relatively small train–test degradation is consistent with the ability of ensemble tree methods to approximate complex non-linear mappings while maintaining good generalisation when a sufficient number of trees and samples are available. These results suggest that the random forest models are capable of capturing the main geometric trends of the coupling coefficients over the design space and are therefore suitable for use as inexpensive surrogates within the NSGA-II optimisation process.

For the maximum magnetic flux density, the performance is more heterogeneous. The lateral control planes exhibit strong predictive quality, with $R^2_{\text{test}} = 0.87$–$0.88$ and RMSE test below 3 $\mu$T, indicating that the surrogates explain most of the variance in $\max |B|$left and $\max |B|$right. In contrast, the top-plane surrogate achieves a markedly lower generalisation score of $R^2_{\text{test}} = 0.61$ and the corresponding test RMSE is approximately three times greater than for the lateral planes, signalling a more challenging response surface and a higher level of unexplained variability. In the context of the present optimisation study, these figures imply that random forest models provide reliable guidance for coupling-related objectives and for lateral field constraints, whereas predictions of $\max |B|_{\text{top}}$ should be interpreted with more caution.

## 6.3 Candidate designs and Pareto fronts

The numerical values in Table 6.2 summarise the objectives associated with the initial geometry and with four representative NSGA–II candidates. For all candidates, the worst-case coupling coefficients $k^{\min}_{11,2}$ and $k^{\min}_{12,2}$ are less negative than in the initial design, indicating an improvement in robustness with respect to misalignment. Candidate 3 attains the highest primary-side minimum ($k^{\min}_{11,2} = -0.0379$), but this comes at the price of the largest amplitudes $A_{11,2}$ and $A_{12,2}$ among the candidates, reflecting a stronger variation of the coupling coefficients across the operating domain $\mathcal{D}$. Candidate 1 is the most favourable in terms of the primary amplitude $A_{11,2}$, while candidate 2 exhibits the lowest secondary amplitude $A_{12,2}$, with both designs achieving noticeable reductions relative to the initial geometry. Candidate 4 sits between these extremes, combining improved minimum couplings on both sides with moderate amplitudes, and can therefore be interpreted as a compromise solution between robustness and sensitivity.

Table 6.2: Objectives of the initial design and of the selected NSGA–II candidate geometries.

| Design | $k_{11,2}^{\min}$ | $k_{11,2}^{\max}$ | $k_{12,2}^{\min}$ | $k_{12,2}^{\max}$ | $A_{11,2}$ | $A_{12,2}$ |
|---|---|---|---|---|---|---|
| Initial | -0.0618 | 0.3172 | -0.0873 | 0.3090 | 0.3789 | 0.3962 |
| 1 | -0.0397 | 0.3133 | -0.0576 | 0.3232 | 0.3530 | 0.3808 |
| 2 | -0.0438 | 0.3222 | -0.0553 | 0.2985 | 0.3659 | 0.3538 |
| 3 | -0.0379 | 0.3566 | -0.0550 | 0.3986 | 0.3945 | 0.4536 |
| 4 | -0.0401 | 0.3212 | -0.0485 | 0.3246 | 0.3613 | 0.3732 |

These tendencies are consistent with the Pareto diagrams in Figures 6.1–6.4, which display the population of non-dominated solutions obtained with NSGA–II and the positions of the initial design and of candidates 1–4. In Figure 6.1, the most desirable region corresponds to the lower-left area, where $k_{11,2}^{\min}$ and $A_{11,2}$ are high and low, respectively. The initial design is located towards the upper-right part of the front, confirming its relatively low robustness and large primary amplitude. Moving along the front towards lower $A_{11,2}$ leads to candidate 1, which substantially reduces the spread of $k_{11,2}$ at the cost of a more modest improvement in the minimum value. In contrast, candidate 3 lies closer to the region of very high $k_{11,2}^{\min}$ , but with a larger $A_{11,2}$, illustrating the compromise between maximising the worst-case coupling and controlling its variation. An analogous interpretation applies to Figure 6.2 for the secondary-side objectives, where candidate 2 clearly favours a reduction in $A_{12,2}$, candidate 3 prioritises $k_{12,2}^{\min}$, and candidate 4 appears near a knee region that balances both criteria.

The interaction between primary and secondary robustness is further clarified in Figure 6.3, which plots $k_{11,2}^{\min}(\mathbf{g})$ against $k_{12,2}^{\min}(\mathbf{g})$. The initial design occupies a corner of the diagram where both minima are relatively low, while the NSGA–II front spans a band of solutions in which improvements on one side tend to degrade the other. Candidate 3 is displaced towards the region of high primary robustness but exhibits only moderate gains on the secondary side, whereas candidate 2 behaves in the opposite manner. Candidate 4 is located near the centre of the front, showing simultaneous, though not extreme, improvements in both minimal values. Finally, Figure 6.4 reveals that the amplitudes $A_{11,2}$ and $A_{12,2}$ are also correlated: designs that strongly reduce the variation of one coupling coefficient often increase, or only slightly decrease, the variation of the other. Candidate 1 reduces $A_{11,2}$ while maintaining $A_{12,2}$ at a level close to the initial value, candidate 2 is particularly effective in reducing $A_{12,2}$, and candidate 4 again offers a balanced compromise with both amplitudes below those of the initial geometry.

These observations guided the selection of the candidates for detailed finite-element validation in the subsequent sections.

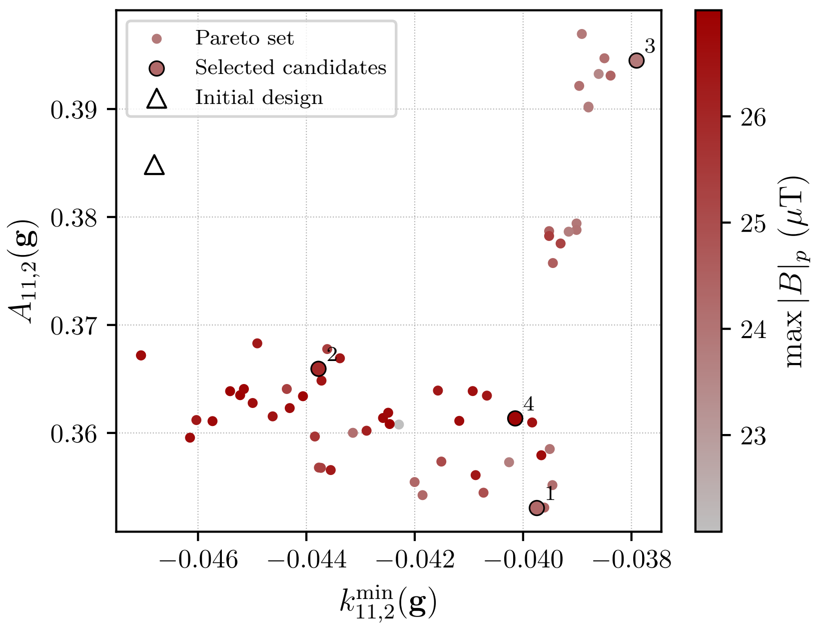


Figure 6.1: Pareto diagram for the primary-side coupling coefficient, showing the compromise between the objective $k_{11,2}^{\min}(\mathbf{g})$ and $A_{11,2}(\mathbf{g})$ for the initial design and to candidates 1–4.

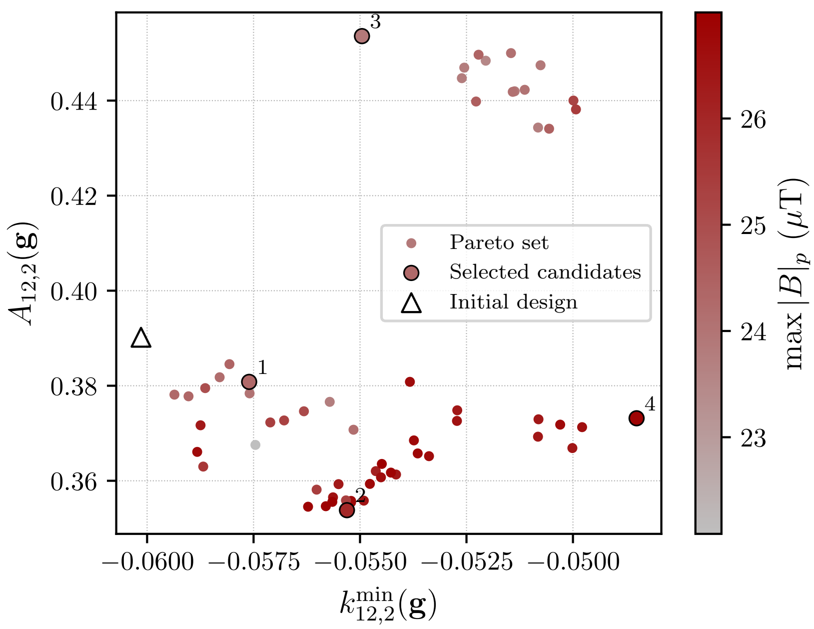


Figure 6.2: Pareto diagram for the secondary-side coupling coefficient, illustrating the compromise between the robustness objective $k_{12,2}^{\min}(\mathbf{g})$ and the amplitude $A_{12,2}(\mathbf{g})$ for initial design and candidates 1–4.

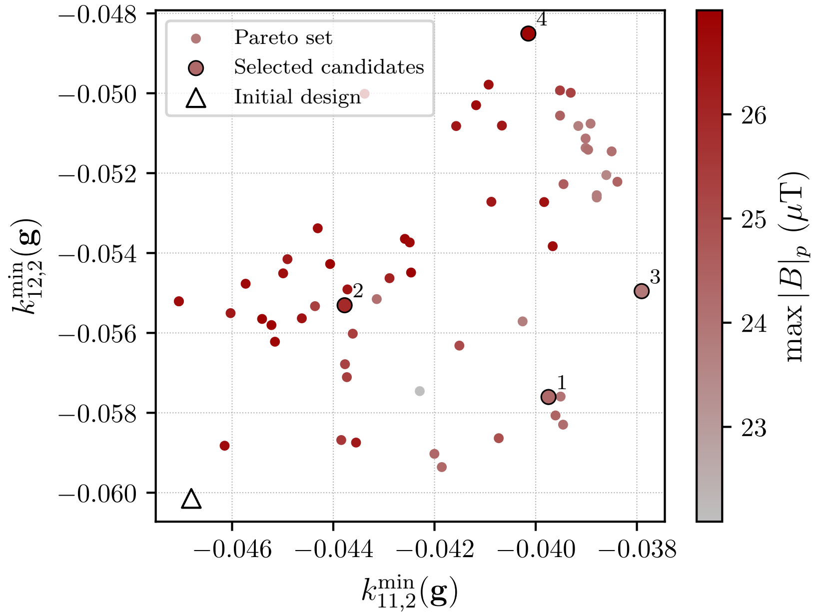


Figure 6.3: Pareto diagram showing the compromise between the worst-case primary and secondary coupling coefficients, $k_{11,2}^{\min}(\mathbf{g})$ and $k_{12,2}^{\min}(\mathbf{g})$, respectively, for the initial design and of candidates 1–4.

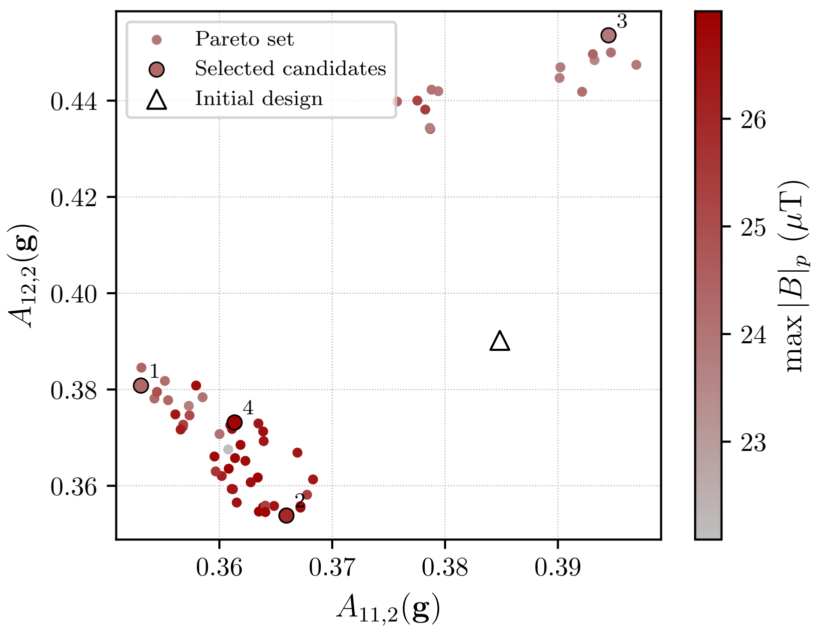


Figure 6.4: Pareto diagram of the amplitudes $A_{11,2}(\mathbf{g})$ and $A_{12,2}(\mathbf{g})$, which quantify the variation of the coupling coefficients with misalignment and vehicle position for the primary and secondary coils, respectively, for the initial design and candidates 1–4.

## 6.4 Response surfaces of initial and optimised design

The response surfaces of the coupling coefficient $k_{11,2}$ provide a compact visual representation of how the primary–secondary coupling evolves with vehicle position and misalignment, and are therefore useful to assess the impact of the geometric optimisation. Figures 6.5 and 6.6 compare the lateral response surfaces $k_{11,2}(x, y)$ for the initial geometry and for candidate design 3, respectively.

In the initial configuration (Figure 6.5), the coupling exhibits a relatively localised peak around the central region of the longitudinal axis and near zero lateral offset, followed by a rapid decay as $x$ increases or as the vehicle moves away from the alignment line. Negative or near-zero values appear as soon as the vehicle crosses the end of the primary coils, indicating that the system quickly loses effective coupling outside a narrow operating window.

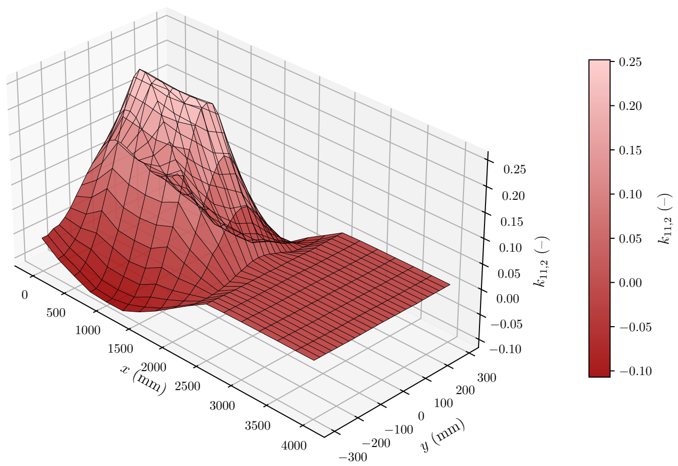


Figure 6.5: Response surface of the primary coupling coefficient $k_{11,2}$ as a function of the longitudinal position $x$ and lateral offset $y$ for the initial coupler geometry.

The optimised geometry, represented in the Figure 6.6, yields a noticeably broader level of high $k_{11,2}$ values along the longitudinal direction and for a wider range of lateral offsets. The peak coupling level is increased and the transition towards lower values is more gradual, particularly for moderate lateral misalignments. This behaviour is consistent with the NSGA–II objectives of improving the minimum coupling coefficient and reducing its sensitivity to lateral displacement, and confirms that candidate 3 provides a more robust lateral response than the initial design.

A similar trend is observed when the coupling coefficient is plotted against the longitudinal position and angular misalignment, $k_{11,2}(x, \alpha)$, in Figures 6.7 and 6.8. For the initial design, the response surface shows a pronounced dependence on $\alpha$ in the vicinity of the alignment condition: small angular deviations around $\alpha = 0°$ already lead to a significant reduction in $k_{11,2}$, and the coupling rapidly decreases to very low values as the vehicle leaves the region above the primary coils. Figure 6.8 indicates, that for the optimised geometry of candidate 3, the high-coupling ridge around $\alpha = 0°$ becomes both higher and wider.

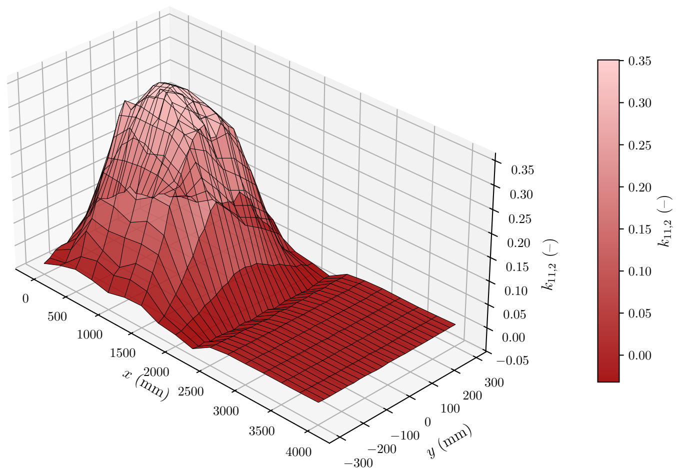


Figure 6.6: Response surface of the primary coupling coefficient $k_{11,2}$ as a function of the longitudinal position $x$ and lateral offset $y$ for candidate design 3 obtained with NSGA–II.

This indicates that the system maintains stronger coupling for a larger range of angular misalignments and longitudinal positions. The surface less smoother and the gradients with respect to $\alpha$ maintained, which is consistent with the improved minimum coupling and larger robustness indices reported earlier. Overall, the comparison of the response surfaces confirms that candidate 3 not only increases the peak values of $k_{11,2}$ but also flattens the response with respect to both lateral and angular misalignment, thereby providing a more stable and practically usable charging performance along the dynamic charging lane.

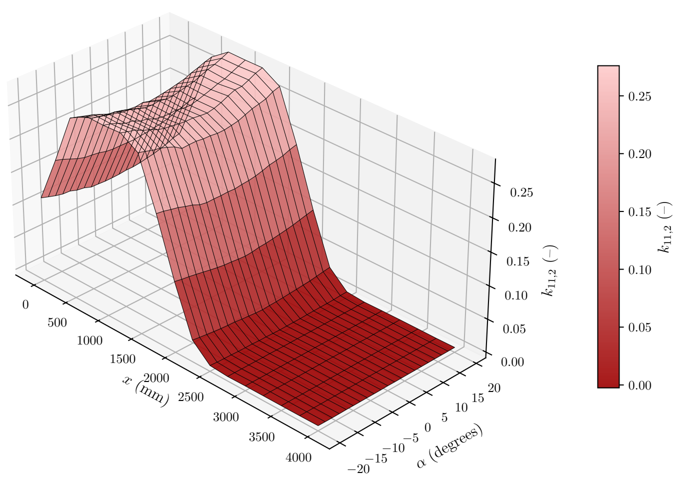


Figure 6.7: Response surface of the primary coupling coefficient $k_{11,2}$ as a function of the longitudinal position $x$ and angular misalignment $\alpha$ for the initial coupler geometry.

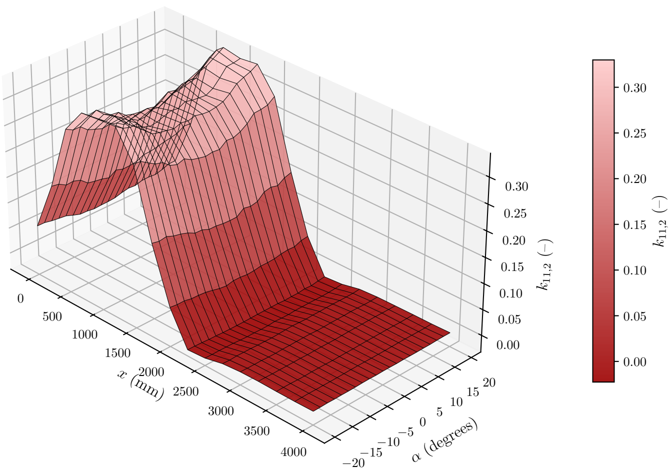


Figure 6.8: Response surface of the primary coupling coefficient $k_{11,2}$ as a function of the longitudinal position $x$ and angular misalignment $\alpha$ for candidate design 3 obtained with NSGA–II.

## 6.5 Magnetic flux density on the control planes

The profiles of the maximum magnitude of the complex magnetic flux density on the control planes provide a direct assessment of MF exposure for both the initial and the optimised geometries. The angular-misalignment plots in Figures 6.9– 6.11 show $\max|B|_{\text{top}}(\alpha)$, $\max|B|_{\text{left}}(\alpha)$ and $\max|B|_{\text{right}}(\alpha)$ at the YZ plane corresponding to the peak coupling, respectively. For the initial design, all three planes exhibit nearly flat but high level, with $\max|B|_{\text{top}}$ around $73$ $\mu$T and the lateral planes around $46$–$47$ $\mu$T over the whole range $0° \leq \alpha \leq 20°$, which substantially exceeds the adopted exposure limit of $27$ $\mu$T.

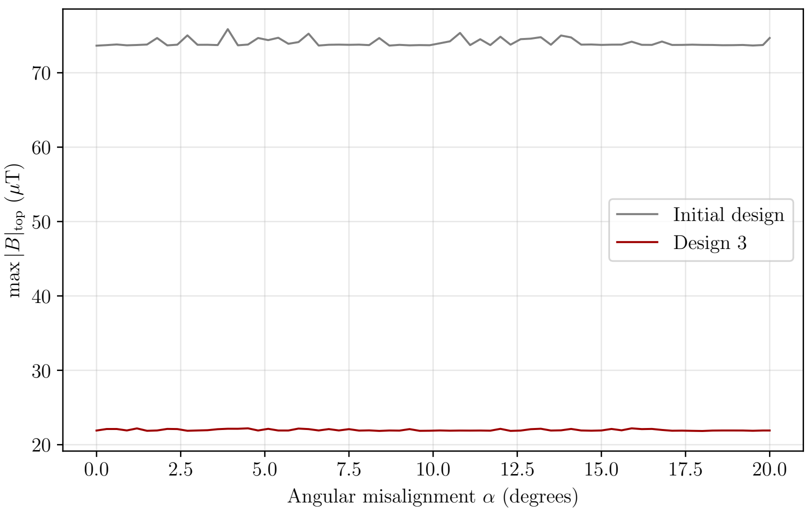


Figure 6.9: Maximum magnetic flux density on the top control plane as a function of angular misalignment $\alpha$ for the initial design and candidate design 3.

In contrast, candidate design 3 maintains field levels close to $22\ \mu$T on the top plane and approximately $18\ \mu$T on the left and right planes, with only very small variations as $\alpha$ increases. The optimised geometry therefore reduces the angular-misalignment field levels by a factor of about three on the top plane and by a factor of about two and a half on the lateral planes, while also providing almost perfectly flat profiles, which is consistent with the robustness objective of the optimisation problem.

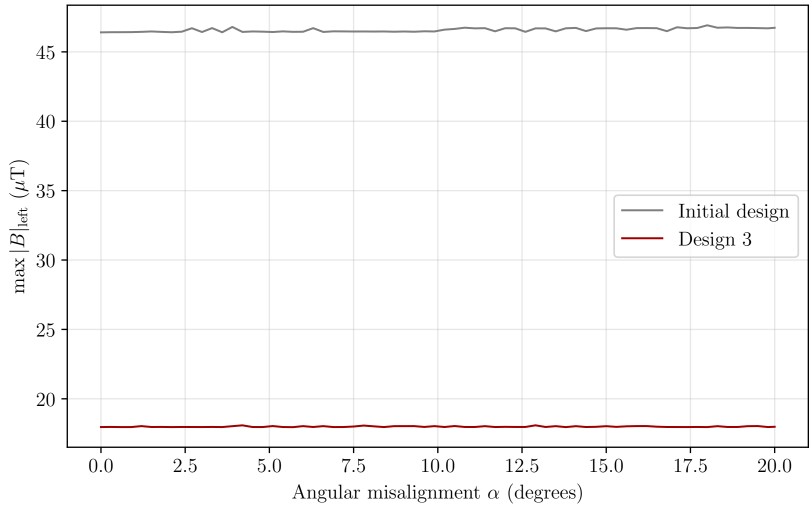


Figure 6.10: Maximum magnetic flux density on the left control plane as a function of angular misalignment $\alpha$ for the initial design and candidate design 3.

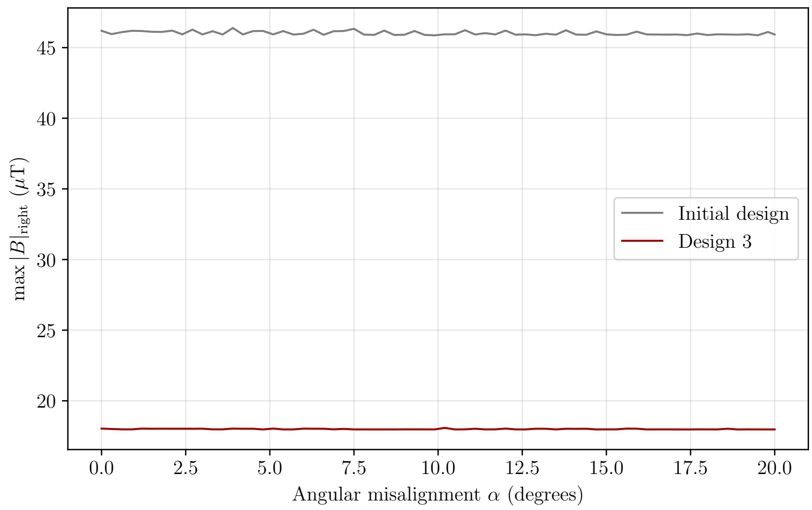


Figure 6.11: Maximum magnetic flux density on the right control plane as a function of angular misalignment $\alpha$ for the initial design and candidate design 3.

A similar behaviour is observed for lateral misalignment in Figures 6.12 and 6.13, which display $\max |B|_{\text{left}}(y)$ and $\max |B|_{\text{right}}(y)$ as functions of the offset $0 \leq y \leq 300$ mm. For the initial design, the lateral field on both planes remains in the range 45–47 $\mu$T, showing a modest dependence on $y$ but persistently exceeding the exposure limit across the whole interval. Candidate 3 again confines the field to approximately 18–19 $\mu$T, largely independent of $y$ and comfortably below the 27 $\mu$T threshold. Taken together, the angular and lateral profiles demonstrate that the optimised geometry simultaneously increases the coupling coefficients (Section 6.3) and achieves a substantial and uniform reduction of the magnetic flux density on all control planes, thereby fulfilling the MF–compliance constraint with a significant safety margin.

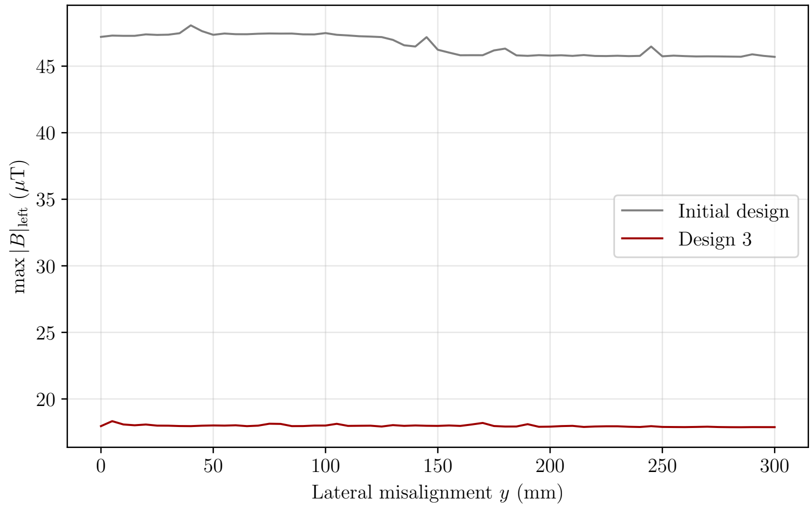


Figure 6.12: Maximum magnetic flux density on the left control plane as a function of lateral misalignment $y$ for the initial design and candidate design 3.

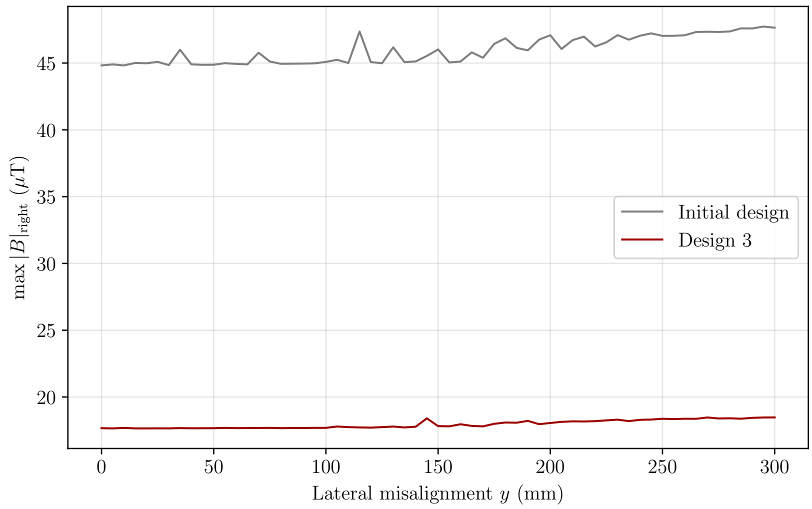


Figure 6.13: Maximum magnetic flux density on the right control plane as a function of lateral misalignment $y$ for the initial design and candidate design 3.

## 6.6 Comparison of the initial and the optimised design

The quantitative comparison in Table 6.2 shows that candidate design 3 achieves a systematic improvement of the coupling coefficients with respect to the initial geometry. The worst–case primary coupling increases from $k_{11,2}^{\min} = -0.0618$ to $k_{11,2}^{\min} = -0.0379$, while the corresponding maximum rises from $0.3172$ to $0.3566$, so that both the lower and upper bounds of $k_{11,2}$ are shifted towards more favourable values. On the secondary side, $k_{12,2}^{\min}$ improves from $-0.0873$ to $-0.0550$ and $k_{12,2}^{\max}$ from $0.3090$ to $0.3986$. These variations correspond to increments of approximately $0.02$–$0.09$ in the coupling coefficients across the operating domain, confirming that candidate 3 provides stronger coupling for both coils in almost all operating conditions. This enhancement is obtained at the expense of a moderate increase in the amplitudes $A_{11,2}$ and $A_{12,2}$, which reflects the higher peak values attained by the optimised design.

The angular and lateral profiles, together with the response surfaces (Figures 6.5 – 6.8), confirm that the coupling of candidate 3 is not only higher on average but also more robust to misalignment. Along both the angular coordinate $\alpha$ and the lateral offset $y$, the $k_{11,2}$ curves of candidate 3 are consistently above those of the initial design over a wide portion of the admissible range, and the transitions between the central alignment region and the misaligned configurations become smoother. In particular, the level of high coupling extends over a larger interval of longitudinal positions $x$ and misalignment values, so that the optimised geometry maintains useful coupling for a broader set of driving trajectories.

The magnetic – flux – density profiles in Figures 6.9 – 6.13 indicate that these gains in coupling are obtained without a detrimental increase in the field levels on the control planes. For all three planes and for both angular and lateral misalignments, the $\max |B|$ curves of candidate 3 remain of the same order of magnitude as those of the initial design, and the peaks are constrained by the exposure limit imposed in the optimisation problem. Taken together, the results demonstrate that candidate 3 represents a genuinely improved geometry: it delivers higher and more robust coupling coefficients over the operating domain while preserving MF exposure within the prescribed bounds.

# 7 Conclusions and future work

The present work has addressed the geometric design of a DIPT coupler for two-wheeled electric vehicles, with particular emphasis on maintaining robust electromagnetic coupling under misalignment while satisfying MF exposure constraints derived from current automotive standards. The work has combined finite-element modelling, surrogate modelling and global sensitivity analysis, and multi-objective optimisation into a single workflow, implemented around an Ansys Maxwell 3D model and advanced optimisation and GSA tools.

## 7.1 Overview of the study and adopted methodology

The first part of the study formulated the physical problem and placed it within the broader context of wireless power transfer technologies and regulatory requirements for dynamic charging. The decision to focus on inductive power transfer was motivated by its combination of high coupling efficiency, and compatibility with bidirectional power flow, which are critical for traction and regenerative braking in micromobility applications. In this context, the coupler was identified as the subsystem where geometry, materials and misalignment tolerances most strongly influence both coupling efficiency and MF leakage.

A detailed three-dimensional FE model of a shielded rectangular DIPT coupler was then constructed in Ansys Electronics Desktop. The primary coil is embedded in the roadway and defined in the global Cartesian reference frame, whereas the secondary assembly is attached to a relative coordinate system that moves with the vehicle, so that longitudinal displacement, lateral offset and angular misalignment can be imposed in a physically consistent manner. Coil windings are represented by 5 mm litz conductors, consistent with the SAE J2954 recommendations, and are supplied by SS–compensated resonant circuits operating at 85 kHz with a 38 A rms current on the primary side feeding a resistive load on the secondary side. Ferrite slabs and aluminium shields are parametrised by their dimensions, thicknesses and spacings, allowing their roles in flux guiding and leakage control to be investigated systematically. Temperature-dependent ferrite properties are described by an anhysteretic Jiles–Atherton model identified from manufacturer B–H curves, and the AC Magnetic solver is configured with adaptive mesh refinement and energy-based stopping criteria to ensure converged field solutions over the design space.

To quantify MF exposure, three control planes are defined above and around the vehicle, following the geometry of the regulatory "Region 3" and related reference levels from SAE J2954 and IEC 61980-3. The quantities of interest extracted from the finite-element simulations are the coupling coefficients between the two primary coils and the vehicle receiver coil, and the maximum magnitude of the complex magnetic flux density on each control plane. These outputs directly reflect the competing objectives of high power-transfer efficiency and low stray-field emission.

Two numerical datasets are then generated by means of a space-filling design of experiments in the joint space of geometric parameters and misalignment variables. A first dataset with 2200 samples varies only the geometric parameters at a fixed nominal position and served to the construction of sparse Polynomial Chaos Expansion (PCE) surrogates and the computation of Sobol'indices. A second dataset with 2500 simulations jointly samples the geometric variables and the control parameters within the bounds $0$ mm $\leq x \leq 4000$ mm, $-300$ mm $\leq y \leq 300$ mm and $-20^\circ \leq \alpha \leq 20^\circ$, thereby covering the relevant dynamic operating envelope.

On the surrogate-modelling side, sparse PCEs with hyperbolic truncation and least-angle regression are identified for all quantities of interest, and canonical LRA are constructed as an independent check of the inferred sensitivity patterns. The second dataset is used to train RF regressors that approximate the mapping from geometric and misalignment variables to coupling coefficients and control-plane flux densities. These forests provide fast evaluations within the design domain and are embedded into a Non-dominated Sorting Genetic Algorithm II (NSGA-II), which solves a multi-objective optimisation problem seeking geometries that enhance worst-case coupling, reduce the variation of coupling with misalignment, and keep the maximum magnetic flux density on all control planes below the adopted exposure limits. Selected Pareto-optimal candidates are finally re-simulated with the full Maxwell model to verify the surrogate predictions and to inspect the detailed three-dimensional response surfaces.

## 7.2 Summary of key findings

The finite-element model developed in this work has shown itself capable of capturing the main electromagnetic phenomena relevant to DIPT couplers under realistic misalignments. The parametrisation of coils, ferrite plates and shields in terms of a moderate set of geometric variables ensured that the design space encompassed both the baseline geometry and a broad family of plausible variants compatible with the packaging constraints of the target electric motorcycle. The use of temperature-dependent ferrite properties and realistic conductor models, together with an excitation consistent with SS compensation at 85 kHz, has enabled a physically consistent evaluation of both coupling and stray-field levels across the design domain.

A key conclusion of the FE analysis is that the baseline coupler, while providing acceptable coupling near the aligned configuration, produces magnetic flux densities on the top and lateral control planes that exceed the adopted reference levels for parts of the misalignment range. The simulated profiles show pronounced peaks in $|B|$ above the vehicle and near the lateral planes when the receiver passes over the end regions of the primary coils or experiences combined lateral and angular offsets. This behaviour reflects the concentration of leakage flux in regions where the ferrite and shielding are less effective, and underscores the need for careful joint tuning of coil, ferrite and shielding dimensions

The finite-element validation of the optimised geometry corresponding to NSGA-II candidate 3 indicates that these geometric adjustments can simultaneously improve coupling robustness and significantly reduce MF exposure. The response surfaces $k_{11,2}(x, y)$ and $k_{11,2}(x, \alpha)$ reveal a broader and higher level coupling, with smoother gradients with respect to lateral and angular misalignment than in the initial design. In parallel, the maximum magnetic flux density on the control planes is reduced and remains below the adopted limit across the investigated misalignment domain, with the largest improvements observed near the end-of-coil regions and for moderate tilts of the vehicle. These results confirm that the adopted modelling and optimisation framework can deliver geometries that satisfy MF constraints without sacrificing dynamic charging performance.

The surrogate-modelling phase has demonstrated that sparse PCEs and LRAs are able to reproduce the FE responses with good accuracy for the parameter ranges considered. Leave-one-out error estimates for the coupling coefficients remain of the order of $10^{-3}$, while those for the magnetic-flux-density maxima on the control planes are modestly higher but still compatible with the level of approximation required for sensitivity analysis. The close agreement between PCE-based and LRA-based Sobol′ indices further increases confidence in the inferred global sensitivity patterns.

The Sobol′ indices reveal a clear hierarchy among the geometric variables. For the coupling coefficients $k_{11,2}$ and $k_{12,2}$, the variance is dominated by the interior length of the primary coil, with the width of the secondary ferrite playing a secondary but non-negligible role. Shield dimensions, ferrite thicknesses and most clearances appear only through small higher-order interactions. For the maximum magnetic flux density on the control planes, the number of primary turns and the interior width and length of the primary coil are identified as the principal drivers, whereas secondary-side ferrite and shield widths exert a moderate influence and most remaining parameters are effectively negligible at first order.

Taken together, these findings imply that a relatively small subset of primary-side design variables jointly controls both coupling and MF levels. This insight justifies the reduction of the optimisation problem to a compact set of decision variables and highlights the central role of primary coil window dimensions and turn count in shaping the trade-off between performance and exposure. The consistency of these trends with recent surrogate-based studies of IPT/DIPT couplers in the literature further supports the validity of the surrogate-based GSA approach adopted here.

The NSGA-II optimisation, driven by Random Forest surrogates trained on the second dataset, has produced a family of Pareto-optimal geometries that make explicit the trade-offs between worst-case coupling, robustness to misalignment and MF constraints. The objectives considered include the minima and maxima of the coupling coefficients over the dynamic operating domain, the amplitudes of their variation with vehicle position, and the maximum magnetic flux density on the control planes, subject to geometric bounds and packaging restrictions.

The resulting Pareto fronts show that substantial improvements in worst-case coupling and robustness indices are attainable while simultaneously reducing MF levels. In particular, the selected candidate 3 achieves a noticeable increase in the minimum coupling coefficients $k_{11,2}$ and $k_{12,2}$ across the misalignment range and decreases the sensitivity of these coefficients to lateral and angular offsets, relative to the baseline design. At the same time, the predicted maximum magnetic flux density on the top and lateral control planes is lowered to values compatible with the adopted regulatory thresholds, a result confirmed by full FE re-evaluation.

A qualitative inspection of the optimised geometry indicates that these improvements are obtained by a coordinated adjustment of the primary coil window, ferrite widths and shield extents within the allowed bounds, in line with the sensitivity patterns previously identified. This confirms the usefulness of combining PCE-based GSA for variable screening and NGSA–II optimisation, and illustrates how a relatively modest number of finite-element simulations can be leveraged to inform a technically demanding geometric optimisation under misalignment and MF constraints.

## 7.3 Limitations of the present work

Despite the encouraging results, several limitations of the present study must be recognised. First, the finite-element model focuses on a single coupler topology. The findings regarding sensitivity and optimal geometries are therefore most directly applicable to similar configurations, and their generalisation to alternative coupler shapes, multi-coil arrangements or different vehicle geometries should be undertaken with care.

Second, the electromagnetic analysis is restricted to the coupling coefficients and magnetic flux density magnitudes on a limited number of control planes. While these quantities are directly linked to coupling efficiency and to the reference levels specified by current automotive MF standards, they do not capture aspects such as detailed internal electric fields within human tissues, local SAR, or the interaction with complex vehicle body structures. As such, the present study assesses regulatory compliance in an approximate manner, and a full dosimetry analysis would require coupled simulations with anatomical phantoms and vehicle models.

Third, although the surrogate models exhibit satisfactory global error metrics, they inevitably introduce approximation error, particularly in regions of the input space where data are sparse. The PCE approach assumes smooth dependence on the inputs and is sensitive to the choice of input distributions and truncation strategy. Instead, such quantities must be estimated via Monte Carlo sampling on the surrogate, adding an extra layer of numerical uncertainty. These limitations are particularly noticeable for the surrogate of the top plane magnetic flux density, whose predictive quality is somewhat lower than for the coupling coefficients.

Fourth, the optimisation problem is formulated at a quasi-static level, assuming fixed operating frequency, compensation topology and load conditions, and not considering thermal constraints and detailed loss mechanisms in conductors, ferrites and shields. Although coupling efficiency is a key contributor to system-level efficiency, end-to-end performance also depends on inverter, rectifier and regulation stages, as well as on thermal management and control strategies, which lie outside the scope of this work. Finally, manufacturing tolerances, material variability and installation uncertainties have not been modelled explicitly. The analysis assumes that the realised geometry coincides with the nominal design, which is an idealisation for practical implementations.

## 7.4 Recommendations for future work

Building on the results and limitations discussed previously, several directions for future research can be identified. A first natural extension is to broaden the electromagnetic analysis to include a more detailed characterisation of losses and thermal behaviour, by coupling the present AC magnetic model with thermal simulations and, if necessary, structural models for thermal-mechanical stresses. Such an integrated model would enable the simultaneous optimisation of coupling efficiency, MF exposure and temperature rise in coils, ferrites and shields, and would connect more directly with end-to-end efficiency assessments as outlined in the system-level discussion of DIPT architectures.

Alternative regression techniques, such as neural-networks, could be explored, particularly for responses that exhibit strong localised features, such as the top plane magnetic flux density. Moreover, future studies could treat misalignment variables as random inputs with prescribed probability distributions and compute Sobol' indices in this extended space, thereby quantifying how variability in driver behaviour and road geometry interacts with geometric uncertainties.

Also, the optimisation framework could be generalised to other coupler topologies and system-level configurations, such as DD or bipolar pads, multi-segment primary tracks, and alternative compensation networks, in line with recent developments reported for DIPT systems. This would help assess the robustness of the conclusions drawn here and support the development of design guidelines that are less dependent on a single use case.

Finally, experimental validation is an essential step towards practical deployment. Future work should therefore include the construction of a reduced-scale or full-scale prototype based on one or more optimised geometries, with measurements of coupling, efficiency and MF levels under controlled misalignments. Comparative analysis between measurements, finite-element predictions and surrogate-based estimates would not only calibrate the models but also reveal unknown phenomena such as manufacturing tolerances, material inhomogeneities and environmental effects. Insights from such experiments could then feed back into refined models and inform subsequent optimisation cycles, closing the loop between simulation, surrogate–based design and hardware realisation in dynamic wireless charging systems.

# References


[1] J. Noeren, N. Parspour, and L. Elbracht, “An Easily Scalable Dynamic Wireless Power Transfer System for Electric Vehicles,” *Energies*, vol. 16, no. 9, p. 3936, May 2023. [Online]. Available: https://www.mdpi.com/1996-1073/16/9/3936

[2] H. Yang, C. Wu, and T. Chen, “Efficiency Improvement for Wireless Power Transfer System via a Nonlinear Resistance Matching Network,” *Electronics*, vol. 12, no. 6, p. 1341, Mar. 2023. [Online]. Available: https://www.mdpi.com/2079-9292/12/6/1341

[3] SAE International, “SAE J 2954 - Wireless Power Transfer for Light-Duty Plug-in/Electric Vehicles and Alignment Methodology,” 2024, place: Warrendale, PA (EUA). [Online]. Available: https://www.sae.org/standards/content/j2954_202408/

[4] Society of Automotive Engineers, “SAE J2954/3 - Dynamic Wireless Power Transfer for both Light and Heavy Duty Vehicles.” [Online]. Available: https://www.sae.org/standards/content/j2954/3/

[5] A. A. S. Mohamed, A. A. Shaier, H. Metwally, and S. I. Selem, “An Overview of Dynamic Inductive Charging for Electric Vehicles,” *Energies*, vol. 15, no. 15, p. 5613, Aug. 2022. [Online]. Available: https://www.mdpi.com/1996-1073/15/15/5613

[6] A. A. Mohamed, A. A. Shaier, H. Metwally, and S. I. Selem, “A comprehensive overview of inductive pad in electric vehicles stationary charging,” *Applied Energy*, vol. 262, p. 114584, Mar. 2020. [Online]. Available: https://linkinghub.elsevier.com/retrieve/pii/S0306261920300969

[7] A. Mahesh, B. Chokkalingam, and L. Mihet-Popa, “Inductive Wireless Power Transfer Charging for Electric Vehicles–A Review,” *IEEE access : practical innovations, open solutions*, vol. 9, pp. 137 667–137 713, 2021. [Online]. Available: https://ieeexplore.ieee.org/document/9552904/

[8] Yao Pei, “Design and optimization of inductive power transfer systems by metamodeling techniques,” phd, Université Paris-Saclay, 2023. [Online]. Available: https://theses.hal.science/tel-04147736v1

[9] Z. Xue, W. Liu, C. Liu, and K. T. Chau, “Critical Review of Wireless Charging Technologies for Electric Vehicles,” *World Electric Vehicle Journal*, vol. 16, no. 2,

p. 65, Jan. 2025. [Online]. Available: https://www.mdpi.com/2032-6653/16/2/65

[10] A. A. Mohamed, A. A. Shaier, and H. Metwally, "Interoperability of the universal WPT3 transmitter with different receivers for electric vehicle inductive charger," *eTransportation*, vol. 6, p. 100084, Nov. 2020. [Online]. Available: https://linkinghub.elsevier.com/retrieve/pii/S2590116820300412

[11] A. Ahmad, M. S. Alam, and R. Chabaan, "A Comprehensive Review of Wireless Charging Technologies for Electric Vehicles," *IEEE Transactions on Transportation Electrification*, vol. 4, no. 1, pp. 38–63, Mar. 2018. [Online]. Available: https://ieeexplore.ieee.org/document/8101562/

[12] B. Luo, T. Long, L. Guo, R. Dai, R. Mai, and Z. He, "Analysis and Design of Inductive and Capacitive Hybrid Wireless Power Transfer System for Railway Application," *IEEE Transactions on Industry Applications*, vol. 56, no. 3, pp. 3034–3042, May 2020. [Online]. Available: https://ieeexplore.ieee.org/document/9026797/

[13] A. Triviño-Cabrera, J. M. González-González, and J. A. Aguado, *Wireless Power Transfer for Electric Vehicles: Foundations and Design Approach*, ser. Power Systems. Cham: Springer International Publishing, 2020. [Online]. Available: http://link.springer.com/10.1007/978-3-030-26706-3

[14] A. Triviño, J. M. González-González, and J. A. Aguado, "Wireless Power Transfer Technologies Applied to Electric Vehicles: A Review," *Energies*, vol. 14, no. 6, p. 1547, Mar. 2021. [Online]. Available: https://www.mdpi.com/1996-1073/14/6/1547

[15] J. Acero, I. Lope, C. Carretero, H. Sarnago, and J. M. Burdío, "Comparative Evaluation of Different Cables for Magnetic Couplers in Inductive Power Transfer Systems," *IEEE Transactions on Industry Applications*, vol. 60, no. 2, pp. 3459–3471, Mar. 2024. [Online]. Available: https://ieeexplore.ieee.org/document/10365541/

[16] W. Zhao, Y. Peng, S. Zhan, and H. Wang, "Design and Optimization of Litz-Wire Planar Spiral Coil for Inductive Power Transfer Application," Apr. 2023. [Online]. Available: https://www.techrxiv.org/articles/preprint/Design_and_Optimization_of_Litz-Wire_Planar_Spiral_Coil_for_Inductive_Power_Transfer_Application/22491235

[17] Y. Bu, W. Wang, T. Kasai, and T. Mizuno, "Improvements in the Transmission Efficiency in an Electric Vehicles Wireless Power Transfer System Using Litz Magnetoplated Wire," in *2016 IEEE Vehicle Power and Propulsion Conference (VPPC)*. Hangzhou, China: IEEE, Oct. 2016, pp. 1–4. [Online]. Available: http://ieeexplore.ieee.org/document/7791705/

[18] Z. Pantic and S. Lukic, "Computationally-Efficient, Generalized Expressions for the Proximity-Effect in Multi-Layer, Multi-Turn Tubular Coils for Wireless Power Transfer Systems," *IEEE Transactions on Magnetics*, vol. 49, no. 11, pp. 5404–5416, Nov. 2013. [Online]. Available: https://ieeexplore.ieee.org/document/6517920/

[19] N. Sekiya and Y. Monjugawa, "A Novel REBCO Wire Structure That Improves Coil Quality Factor in MHz Range and its Effect on Wireless Power Transfer Systems," *IEEE Transactions on Applied Superconductivity*, vol. 27, no. 4, pp. 1–5, Jun. 2017. [Online]. Available: http://ieeexplore.ieee.org/document/7835113/

[20] I.-S. Jeong, B.-I. Jung, D.-S. You, and H.-S. Choi, "Analysis of -Parameters in Magnetic Resonance WPT Using Superconducting Coils," *IEEE Transactions on Applied Superconductivity*, vol. 26, no. 3, pp. 1–4, Apr. 2016. [Online]. Available: http://ieeexplore.ieee.org/document/7440842/

[21] F. F. Sichani, S. Rahnama, M. Raghebi, and C. Sommitsch, "An investigation on micro-hardness, micro-structure and ductility of clad layer in copper clad aluminum wire under multi stage–NCWD," *Materials Research Express*, vol. 7, no. 5, p. 056501, May 2020. [Online]. Available: https://iopscience.iop.org/article/10.1088/2053-1591/ab89e0

[22] C. R. Sullivan, "Aluminum Windings and Other Strategies for High-Frequency Magnetics Design in an Era of High Copper and Energy Costs," in *APEC 07 - Twenty-Second Annual IEEE Applied Power Electronics Conference and Exposition*. Anaheim, CA, USA: IEEE, Feb. 2007, pp. 78–84. [Online]. Available: http://ieeexplore.ieee.org/document/4195702/

[23] F. Lu, H. Zhang, H. Hofmann, and C. C. Mi, "A Dynamic Charging System With Reduced Output Power Pulsation for Electric Vehicles," *IEEE Transactions on Industrial Electronics*, vol. 63, no. 10, pp. 6580–6590, Oct. 2016. [Online]. Available: http://ieeexplore.ieee.org/document/7465826/

[24] Y. D. Ko and Y. J. Jang, "The Optimal System Design of the Online Electric Vehicle Utilizing Wireless Power Transmission Technology," *IEEE Transactions on Intelligent Transportation Systems*, vol. 14, no. 3, pp. 1255–1265, Sep. 2013. [Online]. Available: https://ieeexplore.ieee.org/document/6512050

[25] C. Panchal, S. Stegen, and J. Lu, "Review of static and dynamic wireless electric vehicle charging system," *Engineering Science and Technology, an International Journal*, vol. 21, no. 5, pp. 922–937, Oct. 2018. [Online]. Available: https://linkinghub.elsevier.com/retrieve/pii/S221509861830154X

[26] S. Y. Choi, B. W. Gu, S. Y. Jeong, and C. T. Rim, "Trends of Wireless Power Transfer Systems for Roadway Powered Electric Vehicles," in *2014 IEEE 79th Vehicular Technology Conference (VTC Spring)*. Seoul, South Korea: IEEE, May 2014, pp. 1–5. [Online]. Available: http://ieeexplore.ieee.org/document/7023175/

[27] C. C. Mi, G. Buja, S. Y. Choi, and C. T. Rim, “Modern Advances in Wireless Power Transfer Systems for Roadway Powered Electric Vehicles,” *IEEE Transactions on Industrial Electronics*, vol. 63, no. 10, pp. 6533–6545, Oct. 2016. [Online]. Available: http://ieeexplore.ieee.org/document/7491313/

[28] F. Y. Lin, C. Carretero, G. A. Covic, and J. T. Boys, “A Reduced Order Model to Determine the Coupling Factor Between Magnetic Pads Used in Wireless Power Transfer,” *IEEE Transactions on Transportation Electrification*, vol. 3, no. 2, pp. 321–331, Jun. 2017. [Online]. Available: http://ieeexplore.ieee.org/document/7744668/

[29] M. Budhia, G. A. Covic, and J. T. Boys, “Design and Optimization of Circular Magnetic Structures for Lumped Inductive Power Transfer Systems,” *IEEE Transactions on Power Electronics*, vol. 26, no. 11, pp. 3096–3108, Nov. 2011. [Online]. Available: http://ieeexplore.ieee.org/document/5752254/

[30] R. Bosshard, U. Iruretagoyena, and J. W. Kolar, “Comprehensive Evaluation of Rectangular and Double-D Coil Geometry for 50 kW/85 kHz IPT System,” *IEEE Journal of Emerging and Selected Topics in Power Electronics*, vol. 4, no. 4, pp. 1406–1415, Dec. 2016. [Online]. Available: http://ieeexplore.ieee.org/document/7542513/

[31] G. A. Covic and J. T. Boys, “Inductive Power Transfer,” *Proceedings of the IEEE*, vol. 101, no. 6, pp. 1276–1289, Jun. 2013. [Online]. Available: http://ieeexplore.ieee.org/document/6492113/

[32] Z. Zhang, H. Pang, A. Georgiadis, and C. Cecati, “Wireless Power Transfer—An Overview,” *IEEE Transactions on Industrial Electronics*, vol. 66, no. 2, pp. 1044–1058, Feb. 2019. [Online]. Available: https://ieeexplore.ieee.org/document/8357386/

[33] M. Pinuela, D. C. Yates, S. Lucyszyn, and P. D. Mitcheson, “Maximizing DC-to-Load Efficiency for Inductive Power Transfer,” *IEEE Transactions on Power Electronics*, vol. 28, no. 5, pp. 2437–2447, May 2013. [Online]. Available: http://ieeexplore.ieee.org/document/6289372/

[34] M. H. Hassan and Y. A. Zaghloul, “A Simulation-Driven Exploration of Coil Design and WPT System Integration Strategies for High Quality Factor and Reduced Power Reflections,” in *2024 International Conference on Modeling, Simulation & Intelligent Computing (MoSICom)*. Dubai, United Arab Emirates: IEEE, Dec. 2024, pp. 479–483. [Online]. Available: https://ieeexplore.ieee.org/document/10881061/

[35] Q. Chen, X. Zhang, W. Chen, and C. Wang, “Winding loss analysis of planar spiral coil and its structure optimization technique in wireless power transfer

system," *Scientific Reports*, vol. 12, no. 1, p. 19418, Nov. 2022. [Online]. Available: https://www.nature.com/articles/s41598-022-24006-x

[36] E. Asa, M. Mohammad, O. C. Onar, J. Pries, V. Galigekere, and G.-J. Su, "Review of Safety and Exposure Limits of Electromagnetic Fields (EMF) in Wireless Electric Vehicle Charging (WEVC) Applications," in *2020 IEEE Transportation Electrification Conference & Expo (ITEC)*. Chicago, IL, USA: IEEE, Jun. 2020, pp. 17–24. [Online]. Available: https://ieeexplore.ieee.org/document/9161597/

[37] International Commission on Non-Ionizing Radiation Protection,, "Guidelines for Limiting Exposure to Time-varying Electric and Magnetic Fields (1 Hz to 100 kHz)," *Health Physics*, vol. 99, no. 6, pp. 818–836, Dec. 2010. [Online]. Available: https://journals.lww.com/00004032-201012000-00026

[38] ——, "Guidelines for Limiting Exposure to Electromagnetic Fields (100 kHz to 300 GHz)," *Health Physics*, vol. 118, no. 5, pp. 483–524, May 2020. [Online]. Available: https://journals.lww.com/10.1097/HP.0000000000001210

[39] L. Bodewein, K. Schmiedchen, D. Dechent, D. Stunder, D. Graefrath, L. Winter, T. Kraus, and S. Driessen, "Systematic review on the biological effects of electric, magnetic and electromagnetic fields in the intermediate frequency range (300 Hz to 1 MHz)," *Environmental Research*, vol. 171, pp. 247–259, Apr. 2019. [Online]. Available: https://linkinghub.elsevier.com/retrieve/pii/S0013935119300143

[40] IEEE Standards Association, "IEEE standard for safety levels with respect to human exposure to electric, magnetic, and electromagnetic fields, 0 hz to 300 ghz," 2019.

[41] European Parliament and Council, "Directive 2013/35/EU of the European Parliament and of the Council of 26 June 2013 on the minimum health and safety requirements regarding the exposure of workers to the risks arising from physical agents (electromagnetic fields) (20th individual Directive within the meaning of Article 16(1) of Directive 89/391/EEC) and repealing Directive 2004/40/EC," 2013. [Online]. Available: https://eur-lex.europa.eu/eli/dir/2013/35/oj

[42] "Law No. 64/2017 of 7 August," Lisbon, Portugal, 2017. [Online]. Available: https://dre.pt/dre/detalhe/lei/64-2017-107963496

[43] International Organization for Standardization, "ISO 14117:2019 - Active implantable medical devices — Electromagnetic compatibility — EMC test protocols for implantable cardiac pacemakers, implantable cardioverter defibrillators and cardiac resynchronization devices," Sep. 2019. [Online]. Available: https://www.iso.org/standard/73915.html

[44] International Electrotechnical Commission, "IEC 61980-1 - Electric vehicle wireless power transfer (WPT) systems - Part 1: General requirements," Nov. 2020. [Online]. Available: https://webstore.iec.ch/en/publication/31657

[45] International Organization for Standardization, "ISO 5474-4:2025 Electrically propelled road vehicles — Functional and safety requirements for power transfer between vehicle and external electric circuitPart 4: Magnetic field wireless power transfer," Mar. 2025. [Online]. Available: https://www.iso.org/standard/81300.html

[46] IEEE Standards Association, "IEEE/IEC 63184-2025 - Assessment methods of the human exposure to electric and magnetic fields from wireless power transfer systems - models, instrumentation, measurement and computational methods and procedures (frequency range of 3 kHz to 30 MHz)," Feb. 2025.

[47] International Electrotechnical Commission, "IEC 61980-3 - Electric vehicle wireless power transfer (WPT) systems - Part 3: Specific requirements for magnetic field wireless power transfer systems," Nov. 2022. [Online]. Available: https://webstore.iec.ch/en/publication/66059

[48] D. Patil, M. K. McDonough, J. M. Miller, B. Fahimi, and P. T. Balsara, "Wireless Power Transfer for Vehicular Applications: Overview and Challenges," *IEEE Transactions on Transportation Electrification*, vol. 4, no. 1, pp. 3–37, Mar. 2018. [Online]. Available: https://ieeexplore.ieee.org/document/8168345/

[49] M. Mohammad, E. T. Wodajo, S. Choi, and M. E. Elbuluk, "Modeling and Design of Passive Shield to Limit EMF Emission and to Minimize Shield Loss in Unipolar Wireless Charging System for EV," *IEEE Transactions on Power Electronics*, vol. 34, no. 12, pp. 12 235–12 245, Dec. 2019. [Online]. Available: https://ieeexplore.ieee.org/document/8663438/

[50] T. Campi, S. Cruciani, F. Maradei, and M. Feliziani, "Active Coil System for Magnetic Field Reduction in an Automotive Wireless Power Transfer System," in *2019 IEEE International Symposium on Electromagnetic Compatibility, Signal & Power Integrity (EMC+SIPI)*. New Orleans, LA, USA: IEEE, Jul. 2019, pp. 189–192. [Online]. Available: https://ieeexplore.ieee.org/document/8825202/

[51] A. A. S. Mohamed and A. A. Shaier, "Shielding Techniques of IPT System for Electric Vehicles' Stationary Charging," in *Electric Vehicle Integration in a Smart Microgrid Environment*, 1st ed. Boca Raton: CRC Press, Jul. 2021, pp. 279–293. [Online]. Available: https://www.taylorfrancis.com/books/9780367423926/chapters/10.1201/9780367423926-12

[52] M. Mohammad, J. Pries, O. Onar, V. P. Galigekere, G.-J. Su, S. Anwar, J. Wilkins, U. D. Kavimandan, and D. Patil, "Design of an EMF Suppressing Magnetic Shield for a 100-kW DD-Coil Wireless Charging System for Electric

Vehicles," in *2019 IEEE Applied Power Electronics Conference and Exposition (APEC)*. Anaheim, CA, USA: IEEE, Mar. 2019, pp. 1521–1527. [Online]. Available: https://ieeexplore.ieee.org/document/8722084/

[53] J. Park, C. Park, Y. Shin, D. Kim, B. Park, J. Cho, J. Choi, and S. Ahn, "Planar multiresonance reactive shield for reducing electromagnetic interference in portable wireless power charging application," *Applied Physics Letters*, vol. 114, no. 20, p. 203902, May 2019. [Online]. Available: https://pubs.aip.org/apl/article/114/20/203902/36764/Planar-multiresonance-reactive-shield-for-reducing

[54] E. Zio, "Monte Carlo Simulation: The Method," in *The Monte Carlo Simulation Method for System Reliability and Risk Analysis*. London: Springer London, 2013, pp. 19–58, series Title: Springer Series in Reliability Engineering. [Online]. Available: http://link.springer.com/10.1007/978-1-4471-4588-2_3

[55] A. I. J. Forrester, A. Sóbester, and A. J. Keane, *Engineering Design via Surrogate Modelling: A Practical Guide*, 1st ed. Wiley, Jul. 2008. [Online]. Available: https://onlinelibrary.wiley.com/doi/book/10.1002/9780470770801

[56] C. Lataniotis, D. Wicaksono, S. Marelli, and B. Sudret, "UQLab user manual – Kriging (Gaussian process modeling)," Chair of Risk, Safety and Uncertainty Quantification, ETH Zurich, Switzerland, Tech. Rep., 2024.

[57] S. Marelli, N. Lüthen, and B. Sudret, "UQLab user manual – Polynomial chaos expansions," Chair of Risk, Safety and Uncertainty Quantification, ETH Zurich, Switzerland, Tech. Rep., 2024.

[58] D. G. Krige, "A statistical approach to some mine valuation and allied problems on the Witwatersrand," phd, University of the Witwatersrand, 1951. [Online]. Available: http://hdl.handle.net/10539/17975

[59] G. Matheron, "Principles of geostatistics," *Economic Geology*, vol. 58, no. 8, pp. 1246–1266, Dec. 1963. [Online]. Available: http://pubs.geoscienceworld.org/economicgeology/article/58/8/1246/17275/Principles-of-geostatistics

[60] J. Sacks, W. J. Welch, T. J. Mitchell, and H. P. Wynn, "Design and Analysis of Computer Experiments," *Statistical Science*, vol. 4, no. 4, Nov. 1989, sacks_design_1989. [Online]. Available: https://projecteuclid.org/journals/statistical-science/volume-4/issue-4/Design-and-Analysis-of-Computer-Experiments/10.1214/ss/1177012413.full

[61] T. J. Santner, B. J. Williams, and W. I. Notz, *The Design and Analysis of Computer Experiments*, ser. Springer Series in Statistics. New York, NY: Springer New York, 2018. [Online]. Available: http://link.springer.com/10.1007/978-1-4939-8847-1

[62] V. Dubourg, "Adaptive surrogate models for reliability analysis and reliability-based design optimization," phd, Université Blaise Pascal, Dec. 2011. [Online].

Available: https://theses.hal.science/tel-00697026/

[63] K. Knaisch and P. Gratzfeld, "Gaussian process surrogate model for the design of circular, planar coils used in inductive power transfer for electric vehicles," *IET Power Electronics*, vol. 9, no. 15, pp. 2786–2794, Dec. 2016. [Online]. Available: https://ietresearch.onlinelibrary.wiley.com/doi/10.1049/iet-pel.2016.0392

[64] C. E. Rasmussen and C. K. I. Williams, *Gaussian Processes for Machine Learning*. The MIT Press, Nov. 2005. [Online]. Available: https://direct.mit.edu/books/book/2320/Gaussian-Processes-for-Machine-Learning

[65] J. Oakley, "Bayesian inference for the uncertainty distribution of computer model outputs," *Biometrika*, vol. 89, no. 4, pp. 769–784, Dec. 2002. [Online]. Available: https://academic.oup.com/biomet/article-lookup/doi/10.1093/biomet/89.4.769

[66] J. Rezac, N. Hess, and J. Coder, "Estimating Regions of Wireless Coexistence with Gaussian Process Surrogate Models," in *Proceedings of the 2021 IEEE International Symposium on Electromagnetic Compatibility, Signal and Power Integrity*, Glasgow, 2021. [Online]. Available: https://tsapps.nist.gov/publication/get_pdf.cfm?pub_id=931435

[67] B. Sudret, "Global sensitivity analysis using polynomial chaos expansions," *Reliability Engineering & System Safety*, vol. 93, no. 7, pp. 964–979, Jul. 2008. [Online]. Available: https://linkinghub.elsevier.com/retrieve/pii/S0951832007001329

[68] K. Konakli, C. Mylonas, S. Marelli, and B. Sudret, "UQLab user manual – Canonical low-rank approximations," Chair of Risk, Safety and Uncertainty Quantification, ETH Zurich, Switzerland, Tech. Rep., 2024.

[69] K. Konakli and B. Sudret, "Polynomial meta-models with canonical low-rank approximations: Numerical insights and comparison to sparse polynomial chaos expansions," *Journal of Computational Physics*, vol. 321, pp. 1144–1169, Sep. 2016. [Online]. Available: https://linkinghub.elsevier.com/retrieve/pii/S0021999116302303

[70] M. Chevreuil, R. Lebrun, A. Nouy, and P. Rai, "A Least-Squares Method for Sparse Low Rank Approximation of Multivariate Functions," *SIAM/ASA Journal on Uncertainty Quantification*, vol. 3, no. 1, pp. 897–921, Jan. 2015. [Online]. Available: https://epubs.siam.org/doi/10.1137/13091899X

[71] S. Marelli, C. Lamas, K. Konakli, C. Mylonas, P. Wiederkehr, and B. Sudret, "UQLab user manual – Sensitivity analysis," Chair of Risk, Safety and Uncertainty Quantification, ETH Zurich, Switzerland, Tech. Rep., 2024.

[72] S. Yildiz, H. Pehlivan Solak, and M. Nikbay, "Multi-Fidelity Low-Rank Approximations for Uncertainty Quantification of a Supersonic Aircraft

Design," *Algorithms*, vol. 15, no. 7, p. 250, Jul. 2022. [Online]. Available: https://www.mdpi.com/1999-4893/15/7/250

[73] V. N. Vapnik, *The Nature of Statistical Learning Theory*. New York, NY: Springer New York, 2000. [Online]. Available: http://link.springer.com/10.1007/978-1-4757-3264-1

[74] M. Moustapha, C. Lataniotis, S. Marelli, and B. Sudret, "UQLab user manual – Support vector machines for regression," Chair of Risk, Safety and Uncertainty Quantification, ETH Zurich, Switzerland, Switzerland, Tech. Rep., 2022.

[75] H. Tyralis and G. Papacharalampous, "A review of predictive uncertainty estimation with machine learning," *Artificial Intelligence Review*, vol. 57, no. 4, p. 94, Mar. 2024. [Online]. Available: https://link.springer.com/10.1007/s10462-023-10698-8

[76] M. Aufiero and L. Janson, "Surrogate-Based Global Sensitivity Analysis with Statistical Guarantees via Floodgate," *SIAM/ASA Journal on Uncertainty Quantification*, vol. 13, no. 2, pp. 563–590, Jun. 2025. [Online]. Available: https://epubs.siam.org/doi/10.1137/24M1718330

[77] D. Xiu, *Numerical Methods for Stochastic Computations: A Spectral Method Approach*. Princeton University Press, Jul. 2010. [Online]. Available: http://www.jstor.org/stable/10.2307/j.ctv7h0skv

[78] G. Blatman, "Adaptive sparse polynomial chaos expansions for uncertainty propagation and sensitivity analysis," Ph.D. dissertation, Université Blaise Pascal, 2009. [Online]. Available: http://www.theses.fr/2009CLF21955

[79] O. Chapelle, V. Vapnik, and Y. Bengio, "Model Selection for Small Sample Regression," *Machine Learning*, vol. 48, no. 1-3, pp. 9–23, Jul. 2002. [Online]. Available: https://link.springer.com/10.1023/A:1013943418833

[80] T. Hastie, J. Taylor, R. Tibshirani, and G. Walther, "Forward stagewise regression and the monotone lasso," *Electronic Journal of Statistics*, vol. 1, no. none, Jan. 2007. [Online]. Available: https://projecteuclid.org/journals/electronic-journal-of-statistics/volume-1/issue-none/Forward-stagewise-regression-and-the-monotone-lasso/10.1214/07-EJS004.full

[81] G. Blatman and B. Sudret, "Adaptive sparse polynomial chaos expansion based on least angle regression," *Journal of Computational Physics*, vol. 230, no. 6, pp. 2345–2367, Mar. 2011. [Online]. Available: https://linkinghub.elsevier.com/retrieve/pii/S0021999110006856

[82] L. Breiman, "Random Forests," *Machine Learning*, vol. 45, no. 1, pp. 5–32, Oct. 2001. [Online]. Available: https://link.springer.com/10.1023/A:1010933404324

[83] G. Biau and E. Scornet, "A random forest guided tour," *TEST*, vol. 25, no. 2, pp. 197–227, Jun. 2016. [Online]. Available: http://link.springer.com/10.1007/s11749-016-0481-7

[84] A. Saltelli, Ed., *Global sensitivity analysis: the primer*. Chichester, England Hoboken, NJ: John Wiley, 2008.

[85] I. SoboÍ, "Sensitivity Estimates for Nonlinear Mathematical Models," *Math. Model. Comput. Exp.*, vol. 1, p. 407, 1993. [Online]. Available: https://cir.nii.ac.jp/crid/1370009142503384324

[86] P. Lagouanelle, C. Boulitrop, L. Pichon, F. Freschi, and M. Lambert, "Gradient-based metamodel optimization for the design of 3F3 Ferrites Core in a WPT system," in *2023 24th International Conference on the Computation of Electromagnetic Fields* (*COMPUMAG*), Kyoto, Japan, May 2023. [Online]. Available: https://hal.science/hal-04153335

[87] "Ansys Maxwell Brochure," 2011.

[88] R. M. Nimri, A. Kamineni, and R. Zane, "A Modular Pad Design compatible with SAE J2954 for Dynamic Inductive Power Transfer," in *2020 IEEE PELS Workshop on Emerging Technologies: Wireless Power Transfer* (*WoW*). Seoul, Korea (South): IEEE, Nov. 2020, pp. 45–49. [Online]. Available: https://ieeexplore.ieee.org/document/9291322/

[89] J. A. Afonso, H. G. Duarte, L. A. L. Cardoso, V. Monteiro, and J. L. Afonso, "Wireless Communication and Management System for E-Bike Dynamic Inductive Power Transfer Lanes," *Electronics*, vol. 9, no. 9, p. 1485, Sep. 2020. [Online]. Available: https://www.mdpi.com/2079-9292/9/9/1485

[90] Elektrisola, "High Frequency Litz Wire - Product Program and Technical Data," 2025. [Online]. Available: https://www.elektrisola.com/Download/LitzWire_eng.pdf

[91] International Electrotechnical Commission, "IEC 60317-11 Specifications for particular types of winding wires - Part 11: Bunched solderable polyurethane enamelled round copper wires, class 130, with silk covering," Sep. 2005.

[92] C. R. Sullivan and R. Y. Zhang, "Simplified design method for litz wire," in *2014 IEEE Applied Power Electronics Conference and Exposition - APEC 2014*. Fort Worth, TX, USA: IEEE, Mar. 2014, pp. 2667–2674. [Online]. Available: http://ieeexplore.ieee.org/document/6803681/

[93] Elektrisola, "Litz Wire Details | ELEKTRISOLA," 2025. [Online]. Available: https://www.elektrisola.com/en/Litz-Wire/Info-Details

[94] TDK, "TDK Power Ferrite Material PC47, PC90 and PC95," Oct. 2011. [Online]. Available: https://mhw-intl.com/wp-content/uploads/2011/10/

TDK-Power-Ferrite-Material-Characteristics.pdf

[95] ——, "Mn-Zn Ferrite Material characteristics," Oct. 2022. [Online]. Available: https://product.tdk.com/en/system/files/dam/doc/product/ferrite/ferrite/ferrite-core/catalog/ferrite_mn-zn_material_characteristics_en.pdf

[96] A. Rohatgi, "WebPlotDigitizer," 2025. [Online]. Available: https://automeris.io/

[97] Ansys Inc., "Maxwell(R) Help Release 2025 R2," Jul. 2025.

[98] P. Kis, "Parameter identification of Jiles–Atherton model with nonlinear least-square method," *Physica B: Condensed Matter*, vol. 343, no. 1-4, pp. 59–64, Jan. 2004. [Online]. Available: https://linkinghub.elsevier.com/retrieve/pii/S0921452603005520

[99] P. Stucky and W. Lord, "Skin Depth Considerations in Eddy Current NDT," in *Review of Progress in Quantitative Nondestructive Evaluation*, D. O. Thompson and D. E. Chimenti, Eds. Boston, MA: Springer US, 1992, pp. 299–306. [Online]. Available: http://link.springer.com/10.1007/978-1-4615-3344-3_37

[100] P. D. Desai, H. M. James, and C. Y. Ho, "Electrical Resistivity of Aluminum and Manganese," *Journal of Physical and Chemical Reference Data*, vol. 13, no. 4, pp. 1131–1172, Oct. 1984. [Online]. Available: https://pubs.aip.org/jpr/article/13/4/1131/241367/Electrical-Resistivity-of-Aluminum-and-Manganese

[101] T. Campi, S. Cruciani, F. Maradei, and M. Feliziani, "Two-Coil Receiver for Electrical Vehicles in Dynamic Wireless Power Transfer," *Energies*, vol. 14, no. 22, p. 7790, Nov. 2021. [Online]. Available: https://www.mdpi.com/1996-1073/14/22/7790

[102] S. Marelli and B. Sudret, "UQLab: A Framework for Uncertainty Quantification in Matlab," in *Vulnerability, Uncertainty, and Risk*. Liverpool, UK: American Society of Civil Engineers, Jun. 2014, pp. 2554–2563. [Online]. Available: http://ascelibrary.org/doi/10.1061/9780784413609.257

[103] Y. Leng, D. Luo, Z. Li, and F. Yu, "Coupling coefficient calculation and optimization of positive rectangular series coils in wireless power transfer systems," *Heliyon*, vol. 9, no. 10, p. e21121, Oct. 2023. [Online]. Available: https://linkinghub.elsevier.com/retrieve/pii/S2405844023083299

[104] S.-C. Yang, H. He, X.-Y. Yan, Y.-H. Chen, Y. Hua, Y.-G. Cao, J. Li, H.-H. Li, and S. Yin, "Segmental Track Analysis in Dynamic Wireless Power Transfer," *Energies*, vol. 12, no. 20, p. 3875, Oct. 2019. [Online]. Available: https://www.mdpi.com/1996-1073/12/20/3875

[105] S. Bareli, L. Geri, Y. Nikulshin, O. E. Nahum, Y. Hadas, Y. Yeshurun, E. Yaniv, and S. Wolfus, "Effect of Coil Dimensions on Dynamic Wireless

Power Transfer for Electric Vehicles," Jun. 2021. [Online]. Available: https://www.techrxiv.org/doi/full/10.36227/techrxiv.14852559.v1

[106] M. Bensetti, K. Kadem, Y. Pei, Y. Le Bihan, E. Labouré, and L. Pichon, "Parametric Optimization of Ferrite Structure Used for Dynamic Wireless Power Transfer for 3 kW Electric Vehicle," *Energies*, vol. 16, no. 14, p. 5439, Jul. 2023. [Online]. Available: https://www.mdpi.com/1996-1073/16/14/5439

[107] J. Zimmermann, R. Altenkirch, and U. Van Rienen, "Numerical study on the effect of capacitively coupled electrical stimulation on biological cells considering model uncertainties," *Scientific Reports*, vol. 12, no. 1, p. 4744, Mar. 2022. [Online]. Available: https://www.nature.com/articles/s41598-022-08279-w

[108] N. Prosen, M. Milanovič, and J. Domajnko, "Magnetic Flux Density Measurement Platform for an Inductive Wireless Power Transmitter Coil Design," *Sensors*, vol. 22, no. 2, p. 479, Jan. 2022. [Online]. Available: https://www.mdpi.com/1424-8220/22/2/479

[109] V. D. Buck, C. A. M. López, P. Nimmegeers, I. Hashem, and J. V. Impe, "Multi-objective optimisation of chemical processes via improved genetic algorithms: A novel trade-off and termination criterion," in *Computer Aided Chemical Engineering*. Elsevier, 2019, vol. 46, pp. 613–618. [Online]. Available: https://linkinghub.elsevier.com/retrieve/pii/B978012818634350103X

[110] A. A. Keller, *Multi-Objective Optimization in Theory and Practice II: metaheuristic algorithms*. S.l.: Bentham Science PUblisher, 2019.

Instituto Superior
de Engenharia
Politécnico de Coimbra